

AD-A147 678

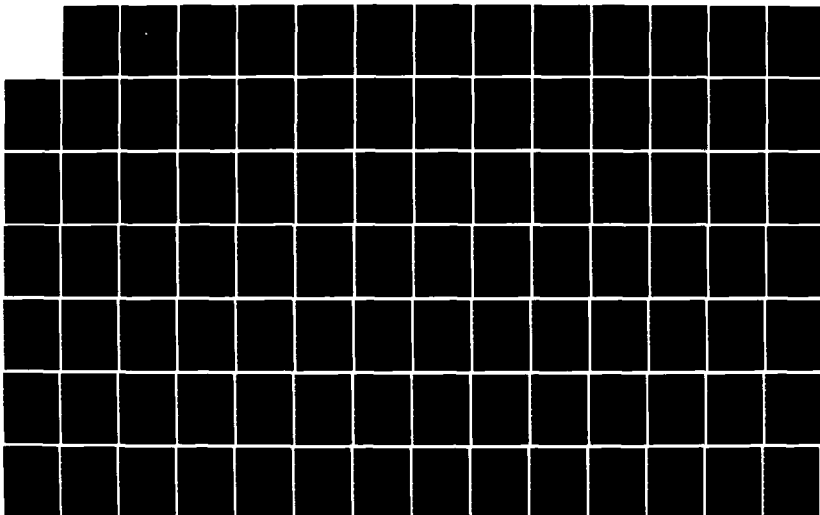
ESTIMATIONS OF DIABATIC HEATING FOR AN  
EXPLOSIVELY-DEVELOPING MARITIME CYCLONE(U) NAVAL  
POSTGRADUATE SCHOOL MONTEREY CA T E BOSSE JUN 84

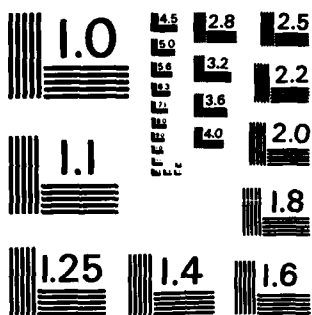
1/2

UNCLASSIFIED

F/G 4/2

NL





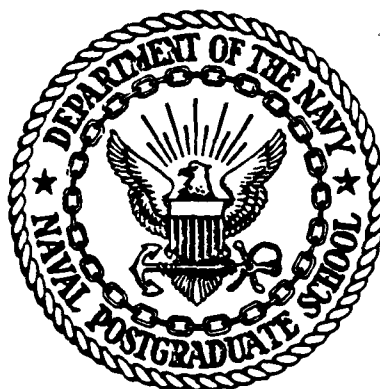
MICROCOPY RESOLUTION TEST CHART  
NATIONAL BUREAU OF STANDARDS-1963-A

2

# NAVAL POSTGRADUATE SCHOOL

Monterey, California

AD-A147 678



DTIC  
ELECTE  
NOV 23 1984  
S D E

## THESIS

ESTIMATIONS OF DIABATIC HEATING FOR AN  
EXPLOSIVELY-DEVELOPING MARITIME CYCLONE

by

Thomas E. Bosse

June 1984

Thesis Advisor:

C. Wash

Approved for public release; distribution unlimited.

DTIC FILE COPY

84 11 15 036

UNCLASSIFIED

SECURITY CLASSIFICATION OF THIS PAGE (When Data Entered)

REPORT DOCUMENTATION PAGE		READ INSTRUCTIONS BEFORE COMPLETING FORM	
1. REPORT NUMBER	2. GOVT ACCESSION NO.	3. RECIPIENT'S CATALOG NUMBER	
AD-A147678			
4. TITLE (and Subtitle) Estimations of Diabatic Heating for an Explosively-Developing Maritime Cyclone		5. TYPE OF REPORT & PERIOD COVERED Master's Thesis; June 1984	
		6. PERFORMING ORG. REPORT NUMBER	
7. AUTHOR(s) Thomas E. Bosse		8. CONTRACT OR GRANT NUMBER(s)	
9. PERFORMING ORGANIZATION NAME AND ADDRESS Naval Postgraduate School Monterey, California 93943		10. PROGRAM ELEMENT, PROJECT, TASK AREA & WORK UNIT NUMBERS	
11. CONTROLLING OFFICE NAME AND ADDRESS Naval Postgraduate School Monterey, California 93943		12. REPORT DATE June 1984	
		13. NUMBER OF PAGES 158	
14. MONITORING AGENCY NAME & ADDRESS (if different from Controlling Office)		15. SECURITY CLASS. (of this report) Unclassified	
		15a. DECLASSIFICATION/DOWNGRADING SCHEDULE	
16. DISTRIBUTION STATEMENT (of this Report)  Approved for public release; distribution unlimited.			
17. DISTRIBUTION STATEMENT (of the abstract entered in Block 20, if different from Report)			
18. SUPPLEMENTARY NOTES			
19. KEY WORDS (Continue on reverse side if necessary and identify by block number)  Diabatic heating in cyclogenesis NOGAPS diabatic parameterization Thermodynamic energy budget			
20. ABSTRACT (Continue on reverse side if necessary and identify by block number)  The Navy Operational Global Atmospheric Prediction System (NOGAPS) boundary layer and cloud parameterizations are evaluated for a case of explosive cyclogenesis in the western North Pacific Ocean. Storm-region diabatic heating estimates are obtained from the application of quasi-Lagrangian diagnostics to a thermodynamic energy budget calculation, and from the NOGAPS diagnoses.			

DD FORM 1 JAN 73 1473

EDITION OF 1 NOV 68 IS OBSOLETE  
S/N 0102-LF-014-6601

1

UNCLASSIFIED

SECURITY CLASSIFICATION OF THIS PAGE (When Data Entered)

UNCLASSIFIED

SECURITY CLASSIFICATION OF THIS PAGE (When Data Entered)

#20 - ABSTRACT - (CONTINUED)

The model-diagnosed sensible heating appears to be correctly positioned, while the diagnoses of convective, large-scale and open-cell cumulus condensation heating produce cloud features which generally reflect the distribution of the clouds in the satellite imagery.

NOGAPS provides a better estimate of the diabatic heating over the open ocean than does the thermodynamic energy budget calculation. The contribution of diabatic heating in this case study is determined to be as significant as that of thermal advection. This diabatic energy input is an order of magnitude greater than that determined from studies of continental cyclogenesis.

Accession For	
NTIS GRA&I	<input checked="checked" type="checkbox"/>
DTIC TAB	<input type="checkbox"/>
Unannounced	<input type="checkbox"/>
Justification	
By	
Distribution/	
Availability Codes	
Avail and/or	
Dist	Special
A-1	



UNCLASSIFIED

SECURITY CLASSIFICATION OF THIS PAGE(When Data Entered)

Approved for public release; distribution unlimited.

Estimations of Diabatic Heating for an  
Explosively-Developing Maritime Cyclone

by

Thomas E. Bosse  
Lieutenant, United States Navy  
B.S., United States Naval Academy, 1976

Submitted in partial fulfillment of the  
requirements for the degree of

MASTER OF SCIENCE IN METEOROLOGY AND OCEANOGRAPHY

from the

NAVAL POSTGRADUATE SCHOOL

June 1984

Author:

Thomas E. Bosse

Approved by:

Carlyle W. Dark

Thesis Advisor

Russell L. Elberg

Second Reader

Richard J. Adams

Chairman, Department of Meteorology

John Dyer

Dean of Science and Engineering

ABSTRACT

→ This thesis evaluates the

The Navy Operational Global Atmospheric Prediction System (NOGAPS) boundary layer and cloud parameterizations are evaluated for a case of explosive cyclogenesis in the western North Pacific Ocean. Storm-region diabatic heating estimates are obtained from the application of quasi-Lagrangian diagnostics to a thermodynamic energy budget calculation, and from the NOGAPS diagnoses.

The model-diagnosed sensible heating appears to be correctly positioned, while the diagnoses of convective, large-scale and open-cell cumulus condensation heating produce cloud features which generally reflect the distribution of the clouds in the satellite imagery.

NOGAPS provides a better estimate of the diabatic heating over the open ocean than does the thermodynamic energy budget calculation. The contribution of diabatic heating in this case study is determined to be as significant as that of thermal advection. This diabatic energy input is an order of magnitude greater than that determined from studies of continental cyclogenesis.

## TABLE OF CONTENTS

I.	INTRODUCTION -----	12
II.	LITERATURE SURVEY -----	18
	A. GENERAL -----	18
	B. SENSIBLE AND LATENT HEAT FLUX -----	18
	C. LATENT HEAT RELEASE -----	22
III.	NOGAPS DIABATIC PACKAGE EVALUATION -----	32
	A. GENERAL -----	32
	B. PROCEDURE -----	33
	C. MODEL BOUNDARY LAYER TREATMENT -----	35
	D. EVALUATION OF SENSIBLE HEAT FLUX AND CLOUD FIELDS -----	40
IV.	ADVECTIVE AND DIABATIC TEMPERATURE CHANGES DURING CYCLOGENESIS -----	70
	A. GENERAL -----	70
	B. THERMODYNAMIC ENERGY BUDGET CALCULATION -----	71
	C. DIABATIC EFFECTS ESTIMATED BY NOGAPS -----	82
	D. NOGAPS AND BUDGET COLUMN WARMING COMPARISON -	91
V.	CONCLUSIONS AND RECOMMENDATIONS -----	93
	A. RESULTS -----	93
	B. RECOMMENDATIONS FOR FUTURE RESEARCH -----	97
	C. FINAL CONCLUSION -----	98
	APPENDIX A: SYNOPTIC SUMMARY -----	99
	APPENDIX B: FGGE DATA -----	103
	APPENDIX C: THE NAVY OPERATIONAL GLOBAL ATMOSPHERIC PREDICTION SYSTEM -----	105



APPENDIX D: TABLES -----	110
APPENDIX E: FIGURES -----	113
LIST OF REFERENCES -----	153
INITIAL DISTRIBUTION LIST -----	157

LIST OF TABLES

I.	Sensible Heat Flux Comparison -----	110
II.	Sigma and Pressure Layer Ranges and Weighting ---	111
III.	Availability of FGGE Data -----	112

# LIST OF FIGURES

1. Storm Track and FNOC Sea-surface Temperature Analysis -----	113
2. NOGAPS BL Diagnosis 12 GMT 13 January 1979 (A) Sensible Heat (B) LCI -----	114
3. NOGAPS BL Diagnoses 12 GMT 13 January 1979 -----	115
4. BL Wind and Flux Fields for 00 GMT 13 January 1979 -----	116
5. Similar to Figure 4 Except for 12 GMT 13 January 1979 -----	117
6. Similar to Figure 4 Except for 00 GMT 14 January 1979 -----	118
7. Similar to Figure 4 Except for 12 GMT 14 January 1979 -----	119
8. Similar to Figure 4 Except for 00 GMT 15 January 1979 -----	120
9. DMSP Visual Satellite Imagery for 2341 GMT 12 January 1979 -----	121
10. DMSP Infrared Satellite Imagery for 2341 GMT 12 January 1979 -----	122
11. NOGAPS Cloud Diagnoses -----	123
12. Similar to Figure 9 Except for 1405 GMT 13 January 1979 -----	124
13. Similar to Figure 10 Except for 1405 GMT 13 January 1979 -----	125
14. Similar to Figure 11 Except for 12 GMT 13 January 1979 -----	126
15. Similar to Figure 9 Except for 0023 GMT 14 January 1979 -----	127
16. Similar to Figure 10 Except for 0023 GMT 14 January 1979 -----	128

17.	Similar to Figure 11 Except for 00 GMT 14 January 1979 -----	129
18.	Similar to Figure 9 Except for 1205 GMT 14 January 1979 -----	130
19.	Similar to Figure 10 Except for 1205 GMT 14 January 1979 -----	131
20.	Similar to Figure 11 Except for 12 GMT 14 January 1979 -----	132
21.	Similar to Figure 11 Except for 00 GMT 15 January 1979 -----	133
22.	Condensation Heating Fields for 00 GMT 13 January 1979 -----	134
23.	Similar to Figure 22 Except for 12 GMT 13 January 1979 -----	135
24.	Similar to Figure 22 Except for 00 GMT 14 January 1979 -----	136
25.	Similar to Figure 22 Except for 12 GMT 14 January 1979 -----	137
26.	Similar to Figure 22 Except for 00 GMT 15 January 1979 -----	138
27.	Distribution of Budget Parameters -----	139
28.	Layer Potential Temperature from ECMWF Initialization and Height Analysis -----	140
29.	Temperature Time Tendency Time Sections -----	141
30.	Advective Temperature Tendency Time Sections -----	142
31.	Diabatic Residual Temperature Tendency Time Section -----	143
32.	Budget Residual and Advective Column Averaged Temperature Tendency -----	144
33.	NOGAPS Total Diabatic Tendency Time Sections -----	145
34.	NOGAPS Convective Condensation Temperature Tendency Time Sections -----	146
35.	NOGAPS Eddy Transport of Sensible Heating Time Sections -----	147

36.	NOGAPS Large-scale Condensation Temperature Tendency Time Sections -----	148
37.	NOGAPS Long-wave Radiation Temperature Tendency Time Sections -----	149
38.	NOGAPS Column-averaged Total Diabatic, Latent Heating, Eddy Sensible Heating and Long-wave Radiation Temperature Tendencies -----	150
39.	NOGAPS Latent Heating Energy Input -----	151
40.	Column-averaged Budget Residual and NOGAPS Total Diabatic Temperature Tendencies -----	152

#### ACKNOWLEDGEMENT

I wish to extend my sincere thanks to Mr. Jim Peak for his programming assistance, and to Mr. Steve Payne for his help with the interpretation of the NOGAPS code and model boundary layer behavior. A special thanks goes to Dr. C.S. Liou for his valuable input and programming assistance, which facilitated the final successful run of the NOGAPS code. Additionally, my sincere appreciation and thanks to my advisors, Professors C.H. Wash and R.L. Elsberry. Without their guidance and timely critical review of the thesis as it evolved, this study could not have been completed.

## I. INTRODUCTION

Explosive extratropical maritime cyclogenesis poses extreme hazards to naval and commercial shipping as well as to stationary oceanic platforms. Rapid cyclogenesis is characterized by intense deepening of a storm system over a short period of time, which results in the generation of high wind and damaging waves. Present numerical models often fail to forecast the intense nature of these systems, which leads to storm-related property damage, injury and death.

The explosively deepening cyclone is described by Sanders and Gyakum (1980) as primarily a wintertime marine event. An explosive event is defined when the normalized  $(\sin \phi / \sin 60)$  central pressure fall is equivalent to one mb/h for 24 h at  $60^\circ\text{N}$ . Their study indicates that these cyclones occur in the vicinity of a strong sea-surface temperature gradient along the leading edge of an outbreak of cold, continental air. The regions of maximum frequency were found to be in the western North Pacific and Atlantic Oceans.

The failure of numerical models to satisfactorily forecast the rapid intensification of explosive systems is well documented in several studies, including those of Sanders and Gyakum (1980), Bosart (1981), and Gyakum (1983). These studies elucidate the problems of numerically forecasting

explosive cyclogenesis. Sanders and Gyakum verified the National Meteorological Center (NMC) six-and seven-layer primitive equation (PE) model predictions of explosive events observed during the 1977-1979 seasons. Their results demonstrated that the coarse mesh, six-layer PE model forecast only about 25% of the observed 12-h central pressure tendency during the explosive stage of cyclogenesis. Use of the higher resolution seven-layer PE model led to only a slight improvement in the forecast ( $< 10\%$ ). Bosart (1981) documented similar deficiencies with the Limited-area Fine Mesh II (LFMII) model in his study of the 1979 President's Day storm. Again, the magnitude of the central pressure fall was drastically underforecast, and this intense storm struck the eastern seaboard of the U.S. with little warning.

In an extreme case, Gyakum (1983) found that the LFMII model underforecast the 12-h explosive deepening of the 1978 Queen Elizabeth II storm by 55 mb. This failure led to gross errors in the wind and wave forecasts and resulted in damage to commercial shipping, most notably in the Queen Elizabeth II, for which the storm was named. Calland (1983) also discovered significant forecast errors in both storm intensity and track in his evaluation of the NMC and Fleet Numerical Oceanography Center (FNOC) coarse-mesh primitive equation model predictions for a western North Pacific Ocean system.

In numerical simulations of the Queen Elizabeth II storm, Anthes et al. (1983) found the incipient model cyclone to



be shallow and sensitive to the initial conditions. They suggested that increased vertical resolution in the lower troposphere and an initial analysis with more representative moisture, static stability and low-level wind structures will lead to improved operational forecasting of maritime cyclogenesis.

This thesis is part of a larger investigation into the nature of maritime extratropical cyclones, which has an overall objective of improving numerical weather prediction over the oceans. The primary objective of this study is to evaluate the contribution of diabatic heating to storm development, especially during the explosive deepening stage. A secondary objective is to analyze the performance of the cloud and boundary layer parameterization package of the UCLA General Circulation Model as incorporated in the Naval Operational Global Atmospheric Prediction System (NOGAPS).

Following the work of Calland (1983), an explosive North Pacific Ocean cyclone is analyzed to determine the quantitative contribution of diabatic heating to cyclone development. This storm possesses the characteristics of 'Type A' cyclogenesis which is described by Petterssen et al. (1962) and Petterssen and Smebye (1971) as frontal wave development initiated by baroclinic instability. This type of cyclogenesis usually occurs with nearly straight upper-level flow over a zone of maximum baroclinity. As the storm develops, an upper-level cold trough forms and maintains a

nearly constant spatial relationship with the low-level cyclone. Petterssen indicates that thermal advection is a dominant term in 'Type A' cyclogenesis, while vorticity advection plays only a minor role. A detailed discussion of the synoptic development of the storm analyzed in this thesis is given by Calland (1983). The significant events of that development are summarized in Appendix A to present a profile of cyclogenesis as it occurred between 13-15 January 1979.

The quantitative analysis of the effect of diabatic heating on storm development is accomplished using the NOGAPS heating package (COMP3) in conjunction with the quasi-Lagrangian diagnostics routine as developed by Johnson and Downey (1975 a and b) and applied by Calland (1983) in his mass and circulation budget study. Fields of convective condensation heat release, large-scale condensation heat release, sensible heat flux, long wave radiation heating, short wave radiation heating and total diabatic heating are derived from diagnostic application of the NOGAPS heating package to the European Center for Medium-Range Weather Forecasting (ECMWF) level IIb analyses of the First Garp Global Experiment (FGGE) data base. This diagnostic use of NOGAPS is similar to the semi-prognostic model application described by Lord (1982), which is discussed in the next chapter. The FGGE data base and ECMWF analyses are discussed in Appendix B.

The ECMWF analyses are interpolated to the six sigma levels of the model at 12 h intervals for a grid which covers the region of storm development with a horizontal resolution of  $1.875^\circ$  in latitude and longitude. These interpolated analyses are used with the NOGAPS diabatic package to diagnostically estimate the heating fields. Storm volume averages of each heating field are prepared for the immediate area of storm influence. Diabatic energy inputs to the column from the total heating and latent heating fields are estimated for the storm volume.

In a parallel analysis, the FGGE data base is used to estimate the total and advective temperature tendencies in the local storm environment through the application of quasi-Lagrangian diagnostics. In this application, the storm volume is centered on, and translates with, the cyclone. This diagnostic technique effectively removes developmental aspects of the cyclone which are associated with the storm motion. Another estimate of the diabatic temperature change is derived as a residual between the total and advective temperature change fields. These results are compared with those obtained from NOGAPS as a check on the model's effectiveness.

A survey of the literature on the role of surface fluxes and latent heat release in cyclogenesis is included in Chapter II. The boundary layer and cloud parameterizations are evaluated in Chapter III through diagnostic use of the NOGAPS code. Storm-related diabatic heating, as determined

by the application of quasi-Lagrangian diagnostics to the FGGE data, is compared to the model-generated diabatic heating in Chapter IV. Conclusions and recommendations for future study are incorporated in Chapter V.

## II. LITERATURE SURVEY

### A. GENERAL

The surface fluxes from the ocean and the release of latent heat through cumulus convection play important roles in ocean cyclone development. When these processes occur in the proper location with respect to a developing system, they can enhance cyclone growth. A review of past studies suggests that these diabatic processes are important ingredients in explosively developing extratropical maritime cyclones.

### B. SENSIBLE AND LATENT HEAT FLUX

Petterssen et al. (1962) constructed composite models of North Atlantic cyclones at various stages of development. They documented strong fluxes of sensible and latent heat in the cold, southward flowing polar air to the north and west of a well-developed frontal zone over the ocean. Although both fluxes were strong in this region, sensible heating was dominant. They found that the daily loss of heat from the ocean to the atmosphere in extreme cases could exceed 20 times the average absorption of incoming solar radiation at high latitudes during winter. The typical sensible heat flux maximum was approximately  $700 \text{ W/m}^2$ . The typical latent heat flux maximum was found to be of this same order of magnitude. Petterssen indicated that the addition of the

sensible heat and moisture flux to cold, polar air will destabilize the boundary layer and cause some convective activity to the north of the frontal zone. Although the sensible heating may be extreme in this region, deep convection does not occur unless the air curves cyclonically.

These composite models depict the warmer air to the south of the frontal zone as tropical in nature. South of the frontal zone the sensible heat flux is minimal, since the atmosphere is essentially in thermal equilibrium with the ocean surface. Most of the moisture that is provided to the frontal system, and later removed as precipitation, has tropical origins.

Anthes et al. (1983) determined through model simulations of the Queen Elizabeth II storm that the surface fluxes have a moderate effect on storm development. In agreement with Petterssen, they found large changes in the PBL and low-level frontal structure to the southwest of the cyclone in the area of strong cold advection. The simulations indicated that the addition of the surface fluxes reduced the gradient of the front as the cold air was modified by the warmer ocean. At the same time these fluxes destabilized and moistened the boundary layer, especially to the southwest of the storm center.

Based on a sample of 256 events of explosive cyclogenesis, Sanders and Gyakum (1980) placed the location of 92% of these storms within, or to the north of the maximum baroclinity

and wind at 500 mb. This statistic indicates that most of the explosive events were placed in the polar air mass where the large-scale horizontal temperature contrasts and the transfer of sensible and latent heat from the warmer ocean to the colder air are important. Most of these explosive deepeners occurred during winter with only a few summer cases noted. This seasonal dependence supports the conclusion that large-scale, horizontal temperature contrasts are important to explosive development. Mullen (1983) also found a strong preference for explosive deepening to the north of the maximum baroclinity at 500 mb in his investigation of explosive cyclones in polar airstreams.

Sanders and Gyakum found that extratropical explosive cyclones are not as sensitive to the sea-surface temperature as tropical cyclones. Explosive cyclones occur over a large range of sea-surface temperatures ( $0^{\circ}$ - $23^{\circ}\text{C}$ ). The sensible and latent heat exchange at the surface is most intense when fast-moving, cold air crosses a strong sea-surface temperature gradient toward warmer water. This scenario results in a modification of the air mass and produces lower static stabilities in the lower troposphere, which is an important factor in explosive development.

Staley and Gall (1977) demonstrated that growth rates of short baroclinic waves were enhanced by lower static stability and strong low-level vertical wind shear. Sanders and Gyakum (1980) hypothesized that the positions of strong sea-surface temperature gradients would indicate areas of

low-level baroclinity with a higher susceptibility to explosive development. Indeed, their analysis of explosive developments in both the North Pacific and Atlantic Oceans demonstrated that these cyclones tended to develop in regions of strong sea-surface temperature gradients.

Bosart (1981) also emphasized the important role played by surface fluxes of sensible and latent heat in the vicinity of a strong sea-surface temperature gradient. In his analysis of the President's Day storm, Bosart noted that large sensible and latent heat fluxes in the region of the Gulf Stream strengthened a low-level baroclinic zone and caused conditionally unstable lapse rates. In a later study of this same system, Bosart and Lin (1984) calculated the sensible heat flux and found that the maximum ranged between approximately 400 and 800  $\text{W/m}^2$  during the period of cyclone development. Latent heat fluxes were found to be as much as three times greater. The average of sensible heating estimated by Chou and Atlas (1982) during the initial cold air outbreak associated with the President's Day storm was 249  $\text{W/m}^2$ . These large boundary layer fluxes altered the environment and enhanced the potential for deep convection, which provided the cyclone circulation with the heat and moisture required for explosive deepening.

In a North Atlantic cyclogenesis case study by Gall and Johnson (1971), the surface sensible heat fluxes generated significant amounts of available potential energy during the period of cyclone development. They indicated that forcing



of large-scale cyclogenesis was influenced by the horizontal extent of the transfer of energy at the surface over the ocean, which was determined by the large-scale environment. They found that the total diabatic available potential energy generation within the storm scale was sufficient to offset the frictional dissipation of kinetic energy during the early and mature stages of the cyclone. This comparison illustrates the important role played by sensible heating, as well as the other diabatic heating sources, in cyclogenesis.

The direct dynamic contribution of sensible and latent heat flux to explosive cyclogenesis appears to be small. Gyakum (1983) cites the importance of low-level baroclinic forcing in initiating cyclone development and providing the lifting necessary to establish a CISK-like mechanism which could drive explosive growth rates. The direct contribution of the surface fluxes in a dynamic situation of this type appears to be minimal, but Gyakum feels that these fluxes are important in that they destabilize the boundary layer and provide the air converging into the low center with the moisture necessary to sustain deep convection.

#### C. LATENT HEAT RELEASE

The role of latent heat release in cyclone development was first studied early in the nineteenth century. Margules (1903) calculated that in a potentially stable situation the release of latent heat served mainly to decrease the rate of cooling of a rising air parcel but did not act to increase

the parcel's kinetic energy. This study did not take into account the effect of the surrounding environment on the system or the rate at which the energy conversion took place. The conclusions of Margules' study did, however, influence research in cyclogenesis for many years (Danard, 1964).

It was not until the 1950's that the convective process was again viewed as an important mechanism in cyclone development. Aubert (1957) concluded that released latent heat greatly increases vertical motion and tends to lower pressure surfaces in the lower troposphere and raise them in the upper troposphere. Petterssen et al. (1962) described the role of released latent heat in cyclone development as having two separate effects depending on the location of the released heat relative to a frontal zone. If the latent heat release takes place in the cold, polar air to the north of a well-developed frontal zone, it has an effect much like that of the sensible heat flux. Condensation here serves to reduce the baroclinity as well as the potential energy of the cyclone as compared to a purely adiabatic system. If, however, the release of latent heat occurs over the frontal surface, condensation serves to increase the potential energy of the cyclone.

Danard (1964) calculated the effect of released latent heat on vertical velocity when the static stability is allowed to vary horizontally. This allowance was an improvement over Margules' closed boundary condition. The results demonstrated that the effect of released latent heat on a

rising air parcel is to increase its vertical velocity. Upward motion is amplified in regions of heavy precipitation, with slight downward motion occurring in the surrounding areas. The increase in vertical velocity in the mid-troposphere from latent heat release leads to increased convergence at low levels and increased divergence aloft.

Danard also related this release of latent heat to the production of kinetic energy and vorticity at upper and lower tropospheric levels which is of the same order of magnitude as the energy and vorticity production from dry adiabatic processes. Danard described the role of released latent heat as a mechanism for cyclone intensification, since he felt that a pre-existing disturbance had to be present for the necessary deep convection to occur. This description is supported by Mak (1982), who found that baroclinic forcing organizes latent heat release on a scale similar to that of the existing disturbance.

Danard (1966) modeled the vertical distribution of latent heat release as a parabolic function with a maximum in the middle troposphere. He compared the results of an energy analysis case study to calculated changes in potential energy due to latent heat release. He found that the increase in available potential energy from condensation heating was much more significant than the loss caused by the increased vertical motion in the low and middle troposphere. This result led to the conclusion that release of latent heat would reduce the loss of available potential energy of the system

normally associated with vertical circulations. He calculated a storm area latent heat release energy maximum of  $11 \text{ W/m}^2$ .

Bullock and Johnson (1971) used a translating budget volume to estimate the generation of available potential energy for early, mature and occluding stages of an extratropical cyclone over the continental United States. They found that the horizontal and vertical distribution of the latent heat release is important in determining its contribution to storm generation. They determined that maximum heating in the lower levels, especially when it occurs over the warm sector, produces the maximum generation of available potential energy. The estimate for storm volume latent heating potential energy production was  $1.31 \times 10^{21} \text{ ergs/s}$  ( $8 \text{ W/m}^2$ ), which is consistent with Danard's findings.

Tracton (1973) evaluated the role of cumulus convection in cyclone development using numerical model forecasts. He tested the following hypothesis:

In some instances of extratropical cyclogenesis, cumulus convection plays a crucial role in the initiation of development through the release of latent heat in the vicinity of the cyclone center. In such cases, dynamical models that do not adequately simulate convective precipitation, especially as it might occur in an environment that is unsaturated, will fail to properly forecast the onset of development.

His evaluation of the NMC six-layer primitive equation model, NMC limited-area, fine-mesh model and FNOC five-layer primitive equation model forecast performance in 19 separate cases of continental United States cyclogenesis supported the hypothesis. In all cases where convection occurred near

the low center in an unsaturated environment, the numerical models failed to properly forecast cyclone development.

In contrast to Danard, Tracton viewed convection as an initiation process in cyclogenesis when it occurred near the surface low center. He suggested that released latent heat caused these cyclones to develop earlier than they would have with only large-scale baroclinic processes affecting them. This inference was demonstrated by associating the model forecast lag time with cyclones where the vorticity advection was weak. He found that the largest deepening at the storm center occurs when the ratio of upper tropospheric to lower tropospheric latent heating is smallest.

In a study of east coast cyclogenesis, Danard and Ellenton (1980) supported the conclusion of Bullock and Johnson (1971). Danard and Ellenton found that it is the configuration of the latent heat release that determines this diabatic influence on cyclone intensification. They discovered that the Laplacian of the surface heating did not lead to intensification over the low center, even though surface fluxes were strong in the cold air behind the storm. In agreement with Gyakum (1983), Danard and Ellenton felt that the surface fluxes contributed to the development of favorable vertical distributions of temperature and moisture which enhance later cyclone intensification.

Sanders and Gyakum (1980) also studied the performance of the NMC primitive equation models in explosive situations. They found that the primitive equation models drastically

underforecast the intensity of developing cyclones. An increase in horizontal resolution of the model did not correct the magnitude of the observed deficiency. Sanders and Gyakum concluded that several factors are poorly represented in current models. Based on the extent of cumulus convection observed in satellite imagery of explosive cyclones, they indicated that a better representation of the effect of cumulus convection and latent heat release, as well as an improved PBL formulation, is required for the model calculations.

Gyakum (1983) found that the Queen Elizabeth II cyclogenesis was initiated by shallow baroclinic forcing in a region of widespread potential instability, which led to the outbreak of cumulus convection in the vicinity of the surface low center. He observed that adiabatic, quasi-geostrophic dynamics could not account for the observed intensity of cyclone development during its explosive stage.

The following relationship was used by Gyakum to determine the contribution of diabatic heating to storm development:

$$\frac{\partial h}{\partial t} = \underset{(1)}{C} \cdot \underset{(2)}{\nabla h} - \underset{(3)}{V} \cdot \underset{(4)}{\nabla h} + \underset{(5)}{\left(\frac{\partial h}{\partial t}\right)_{\text{adiab}}} + \left(\frac{\partial h}{\partial t}\right)_{\text{diab}} \quad (1)$$

where (1) is the mean layer thickness change following the storm center; (2) is the thickness change produced by the cyclone's movement; (3) is the change due to horizontal temperature advection; (4) is the change from adiabatic warming and cooling due to storm-scale vertical motion; and

(5) is the diabatic contribution to thickness change. The contribution of diabatic heating to the thickness change over the low center was determined through a residual calculation using the parameters of observed thickness change, temperature and assumed vertical velocity profiles. The residual warming of the column over the surface low center was found to be very significant (about 16°C) during the 12-h explosive period of this cyclone.

Gyakum concluded that much of the converging air at the surface ascended within convective towers near the low. This ascending air provided the bulk heating that likely forced the vertical motion not accounted for by adiabatic, quasi-geostrophic dynamics. The vertical heating ( $\dot{q}$ ) profile was modeled with a mid-level maximum and zero values at the surface and top of the atmosphere. Linear profiles were assumed between these points. By varying the level of maximum heating, Gyakum found that heating profiles having a maximum at low levels could force surface convergence and vertical ascent on a scale consistent with the observed extreme geopotential height falls. He calculated that cumulus-induced subsidence warming in the vicinity of the low during the explosive stage produced column warming of 16°C over a 12-h period. Warming of this magnitude was sufficient to account for the observed 12-h thickness changes in the column.

Model simulations of the Queen Elizabeth II storm by Anthes et al. (1983) support most of Gyakum's findings.

Comparisons of simulations with and without latent heating produced upper tropospheric temperature differences of  $8.9^{\circ}\text{C}$ , with the warmer values associated with the latent heat release from deep convection. The simulation with latent heating included was colder in the lower troposphere where the heaviest precipitation occurred, but warmer in the surrounding areas due to the compensating subsidence. The genesis in the model was not significantly affected by latent heat release during the early stages. Anthes, et al. (1983) indicated that the relatively weak contribution of latent heating during this early period supported the hypothesis that baroclinic instability was the mechanism for early development. Once stronger vertical motions were established, latent heating played a more important role in later intensification.

In a study of an extratropical maritime cyclone during the initial phase of the 1975 Air Mass Transformation Experiment, Chen et al. (1983) also determined that maritime cyclogenesis is enhanced by latent heat release. Model simulations of this storm indicated that the latent heating was linked to the surface fluxes. When the surface fluxes were removed from the experiment, the amount of latent heating, as well as cyclogenesis, was reduced. The latent heating also had an impact on the phase speed of the cyclone. Reductions in latent heating led to a slower translation of the storm system.



In summary, numerous studies have found surface fluxes of sensible and latent heat, as well as the effects of latent heat release induced by convective processes, to be significant in certain situations of cyclogenesis. The surface fluxes provide heat and moisture to the cold continental air which destabilizes the boundary layer and provides a favorable environment for sustained convection. Latent heat release, particularly in the vicinity of a surface low center, will increase both the vertical velocity and surface convergence in the region. The lower the level where the maximum of this heat release occurs, the greater the surface convergence. This type of bulk heating will lead to an increase of the energy and vorticity of a cyclone, especially if the deep convection takes place near a surface low center. The latent heat release appears to be a mechanism for storm intensification rather than initiation, and increases in importance once the vertical circulation has been established by low-level baroclinic forcing.

Several studies suggest that a CISK-like mechanism may be responsible for the rapid growth and extreme deepening observed in explosively deepened cyclones. Subsidence warming over the surface low would be induced by surrounding convective towers and may provide enough heating to the column to produce the 12-h geopotential height falls observed in some of the intense warm-core systems.

Numerical models that do not properly consider the diabatic effects in cyclone development perform poorly where

convection occurs in an unsaturated environment. All of the operational models that have been tested fail to forecast adequately the rate of development of explosive maritime cyclones.

### III. NOGAPS DIABATIC PACKAGE EVALUATION

#### A. GENERAL

The Naval Operational Global Atmospheric Prediction System (NOGAPS) model, which is based on the UCLA General Circulation Model (GCM), is comprised of a series of routines which are structured to produce analyses and predictions on a global basis. A discussion of NOGAPS (version 2.0) is contained in Appendix C. Subroutine COMP3 incorporates the main diabatic processes for the model.

Diabatic processes of this Pacific storm system are analyzed using COMP3 in a diagnostic mode. This approach is similar to the semi-prognostic technique utilized by Lord (1982) in his test of the Arakawa-Schubert cumulus parameterization for the tropical Atlantic region. Lord made use of observed parameters to estimate the large-scale forcing of a cumulus ensemble at given observation times. These observations and the parameterization are combined to predict precipitation and cumulus warming and drying for each observation time. The semi-prognostic method is not an integration in time and it is therefore free of any modeling errors other than those in the parameterization. This approach allows for a comparison of model-generated tendencies with observed tendencies for each observation time, since the observed tendencies are not included in the model calculations. The

diagnostic use of COMP3 is described in more detail in the next section.

Diagnostic (semi-prognostic) fields of sensible heat flux, convective condensation heating, large-scale condensation heating, total surface precipitation, boundary layer (BL) thickness and layer cloud instability (LCI) are produced by COMP3 using the ECMWF FGGE data as the large-scale forcing. The diabatic processes, as depicted by COMP3 using the semi-prognostic technique, are evaluated during storm development by comparison with observed data and satellite imagery.

#### B. PROCEDURE

The 12-h FGGE data are utilized to study storm diabatic processes for a case of Western Pacific explosive cyclogenesis during the period 00 GMT 13 January to 00 GMT 15 January 1979. A complete discussion of the synoptic development of this cyclone is given by Calland (1983). A summary of this development is included as Appendix A.

COMP3 is evaluated independently of the full NOGAPS model. Boundary layer (BL) information which is normally provided to COMP3 by NOGAPS is developed internally through an iterative process at each 12-h evaluation time. Diagnostic (semi-prognostic) utilization of COMP3 is accomplished by resetting the basic parameters of surface pressure, temperature, moisture and wind components to the ECMWF analysis values after each iteration. This technique allows COMP3 to compute the physical processes without advancing in time. Ten iterations

of the code are performed at each analysis time to allow the opportunity to develop a suitable boundary layer.

An initial guess of 100 mb is made for BL thickness. The initial jumps of the wind components, temperature and moisture at the BL inversion are set equal to zero at 00 GMT 12 January 1979. The iterated boundary layer parameters are passed to the next analysis time as the initial guess and the code is again iterated to develop the boundary layer for each new time period. This process is repeated for each time through 00 GMT 15 January 1979. It should be noted that a shift in the FGGE data grid occurs at 12 GMT 14 January 1979 (Calland, 1983). For continuity, BL parameters in the overlapping regions of the two data grids are passed directly to the new grid as the first guess field for 12 GMT 14 January. Initial BL parameters for the non-overlapping area of the new grid are given by the northern row and western column of the overlapping portion of the grid. Due to oscillatory behavior in some of the BL parameters, averaging is performed over the last six iterations of each evaluation. More details on this boundary layer treatment are presented in the next section.

Sea-surface temperatures (SST's) from FNOC are used from 12 and 16 January 1979. The 12 January 1979 analysis corresponds to the first FGGE data grid and is used for the first three evaluation times. The 16 January 1979 SST field corresponds to the second FGGE data grid and is incorporated into

the analysis of the last two evaluation times. These analyses and the storm track are included as Fig. 1. The SSTs are extracted from the FNOC analysis at the FGGE gridpoints. These values are used as surface temperature in COMP3, except over land where the FGGE 1000 MB air temperature is entered as the surface temperature. All fields discussed in this chapter utilize a  $53 \times 30$  section of the ECMWF analysis grid with  $1.875^\circ$  latitude and longitude resolution.

The diagnostic output is analyzed in the following sections to demonstrate model behavior and performance in a case of maritime explosive cyclogenesis. Comparisons with the FGGE analyses, satellite imagery and previous investigations are made to determine the realism of the model's diabatic parameterization response in this intense developing cyclone.

#### C. MODEL BOUNDARY LAYER TREATMENT

The model BL parameters in regions of strong sensible heating are characterized by an oscillatory tendency which becomes apparent as the BL is iteratively developed at each evaluation time. COMP3 is successively iterated at each time to allow for boundary layer development, as previously discussed. The BL parameters of thickness, and inversion jumps of wind, temperature and moisture are checked for convergence at each iteration. Oscillations, especially in the BL thickness, occur at points where stratus is diagnosed in the lowest layers. BL parameters at non-stratus gridpoints demonstrate

convergence within ten iterations. BL thickness oscillations with magnitudes in excess of 100 mb are observed at some gridpoints. Similar oscillations have been previously noticed in the operational version of the model and a minor code change was instituted to reduce the effect. Discussions with Mr. Steve Payne of the Navy Environmental Prediction Research Facility (NEPRF) and further investigation provide the following scenario for model behavior at gridpoints where oscillations in the BL thickness fields are observed.

The top of the boundary layer is restricted below the lowest sigma level (maximum BL thickness of about 200 mb). A layer cloud instability (LCI) test is performed at gridpoints where stratus is diagnosed by the model. Only stable stratus is permitted in the boundary layer. Unstable stratus occurs in areas where strong fluxes at the surface result in increased entrainment of dry air into the inversion region. This increased entrainment tends to eliminate the stratus deck, which is then treated as cumulus by the model. Since cumulus is not allowed within the boundary layer, the top of the boundary layer is lowered to the bottom of the cloud deck at gridpoints where unstable clouds are diagnosed. The moisture that was in the upper portion of the collapsing boundary layer is left behind to be removed as layer six large-scale precipitation.

Oscillations in the BL thickness field are a result of the above process. As the boundary layer is developed through successive iterations at a gridpoint where unstable

stratus is identified, the BL height is allowed to increase until the unstable stratus is located within the boundary layer. The top of the boundary layer is then collapsed to the base of the unstable cloud deck. In the next iteration, the boundary layer is allowed to grow again since unstable clouds are no longer within it. The following iterations will repeat this pattern and produce a bimodal oscillation in the BL thickness field.

Similar boundary layer behavior was observed by Elsberry et al. (1984) in an evaluation of the NOGAPS diagnosis of the diabatic processes in eastern Pacific Ocean post-frontal convective clusters. That study emphasizes the modification of the transfer coefficients used in the model surface flux parameterization which occurs when the BL height decreases to a minimum value. The model sensible heating parameterization is given by Deardorff (1972). His surface heat flux relationship is

$$H = \rho C_p (\theta_s - \theta_m) U_m C_u C_\theta \quad (2)$$

where  $C_u$  is the friction transfer coefficient,  $C_\theta$  is the heat transfer coefficient,  $\theta_s$  is the surface potential temperature,  $\theta_m$  is the mean BL potential temperature,  $U_m$  is the mean BL wind component,  $\rho$  is the density, and  $C_p$  is the specific heat at constant pressure. The coefficients  $C_u$  and  $C_\theta$  are increased at gridpoints where the boundary



layer thickness becomes extremely small ( $< 250$  m). The very large surface sensible heat flux maxima produced by NOGAPS may then be due, in part, to the increase of the transfer coefficients caused by the collapsing boundary layers in these areas.

The code change implemented in the operational version of the model, provided by Mr. Steve Payne of NEPRF, consists of an artificial boundary layer inversion which is inserted when LCI is diagnosed. This change reduces the magnitude of the oscillations that occur. A similar result was documented by Elsberry et al. (1984) when this change was implemented in their diagnosis.

All NOGAPS fields are averaged in time over the last six iterations to give more representative results. This averaging is necessary because the implemented code modification leads to some trimodal as well as bimodal variations of reduced magnitude. The first four iterations are excluded from the averaging process to allow for initial convergence of the BL parameters at stable gridpoints.

To verify model behavior in regions where instabilities are expected, fields of sensible heat flux, LCI, BL thickness and layer six large-scale precipitation are compared at each evaluation time. Fields from 12 GMT 13 January 1979 are shown in Figs. 2 and 3 for illustration purposes and are representative of other time periods. Figs. 2a and 2b present the surface sensible heat flux field and areas where LCI is

diagnosed by the model. A comparison at locations A and B of these figures clearly demonstrates that the model diagnoses unstable stratus and strong positive sensible heat flux in the same region.

Locations of the small (20 mb or less) BL thickness and layer six large-scale precipitation are mapped in Fig. 3. A comparison at locations A and B of Figs. 3a and 3b with those of Figs. 2a and 2b shows that areas of minimum BL thickness and layer six large-scale precipitation are associated with the sensible heat flux maxima and LCI fields. Regions of large-scale precipitation not associated with the layer cloud instability are assumed to be the result of large-scale processes only.

Comparisons of these figures support the scenario of model behavior as discussed previously. Evidence indicates that the model diagnoses unstable clouds where the sensible heating maxima occur. In these regions, the BL heights have collapsed, and moisture is removed as large-scale precipitation. This behavior illustrates an elaborate method for the model to account for the presence and effect of cloud streets and open-cell cumulus which form in the cold air where the surface sensible heating is strong. Although open-cell cumulus is actually a convective cloud, it is not labelled as such in the model.

#### D. EVALUATION OF SENSIBLE HEAT FLUX AND CLOUD FIELDS

The NOGAPS fields of surface sensible heat flux, convective and large-scale cloud location, and convective and large-scale condensation heating are evaluated through comparisons with ship reports, ECMWF FGGE analysis, satellite imagery and past studies. The purpose of the evaluation is to determine the validity of the fields as produced by the model. The 1000 mb wind analyses are produced directly from the FGGE wind components, while the diabatic heating, boundary layer thickness and layer cloud instability fields are taken directly from the model output. Convective and large-scale cloud maps are generated by assigning a value of one to each gridpoint where that type of precipitation is present in the model output, and a zero otherwise. The values at the six sigma levels are then summed at each time and the resulting fields are plotted. Contours of these composite fields indicate where, and at how many levels, convective or large-scale precipitation is present in the model.

##### 1. Sensible Heat Flux

The evaluation of the sensible heat flux is based on the bulk formulation where sensible heating is directly proportional to the air-sea temperature difference and the boundary layer wind speed at each gridpoint. The 1000 mb ECMWF wind field is taken as representative of the boundary layer wind field for this evaluation. The NOGAPS surface temperature and BL surface air temperature, which is a model

extrapolation of the 1000 mb FGGE air temperature, are used to compute the air-sea temperature differences. Figures of satellite imagery are referred to out of sequence in this section to support the sensible heat flux diagnoses without complicating the comparison with the model cloud maps in the next section.

a. 00 GMT 13 January 1979

The storm system organized during the previous 24 h, but has not reached the explosively deepening stage. The center of the disturbance is located approximately 600 n mi to the southeast of Japan on the warm side of a relatively weak sea-surface temperature gradient. An intense cyclone is located to the east of the Kamchatka Peninsula. This cyclone dominates the flow pattern in the boundary layer wind field as illustrated in Fig. 4a.

Two distinct features are evident in the sensible heat flux field (Fig. 4b). The first is a two-pronged positive flux maximum in the vicinity of, and to the north of, the storm center. A comparison with Fig. 4a indicates that this flux feature is tied closely to the BL wind field. The northern area, identified as 'A', results from the strong westerly flow to the southwest of the Kamchatka cyclone. This flow carries cold, continental air over a relatively warm sea surface, although the temperature gradient is weak. The magnitude and extent of this flux maximum is directly linked to the strength of the flow in the region, which peaks

at 27 m/sec, and the air-sea temperature difference, which is strongly negative over the area (-11 to -23°C). Verifying ship reports from this region generally support the range of air-sea temperature differences determined from the ECMWF analyses (observed differences: -9 to -20°C). However, the observed windspeeds are of only half the magnitude of those represented in the analyses.

The southern maximum area, identified as feature 'B' in the figure, results from a separation in the westerly flow to the north, which transports some of the cold flow southward across the sea-surface temperature gradient. This split in the flow pattern is a manifestation of the developing circulation of the incipient cyclone to the south. The wind speeds are generally lower, and the air-sea temperature difference (maximum: -17°C) is less than in the area of the northern maximum, which accounts for the smaller sensible heat flux diagnoses in this region. In situ measurements support the air-sea temperature difference and the windspeeds used in the model diagnoses for this region.

The second feature of interest in Fig. 4b is the maximum of negative flux, identified as 'C', found to the east of the developing storm center. Although sizeable negative surface fluxes are rare in a mid-latitude winter situation, this negative flux is driven in the model by the strong southerly flow which funnels warm, tropical air across the sea-surface temperature gradient over colder water. A

comparison of the figures indicates that the region of negative flux is coincident with this southerly flow. The largest negative flux is found where the magnitude of the southerly flow is highest (27 m/sec), and the air-sea temperature difference is most positive (+15°C). Ship measurements from this region support an air-sea temperature difference of only +2°C, and a maximum windspeed of 15 m/s. It appears that discrepancies in the ECMWF analyses force the model to diagnose excessive amounts of negative sensible heat flux.

A comparison of Fig. 4b with the visual imagery for this time (Fig. 9) indicates that the region of sensible heat flux maximum to the north (A) has an extensive cover of cloud streets and open-cell cumulus which verifies the presence of strong surface fluxes, while sensible heat flux maximum 'B' is covered by the main storm cloudiness. Feature 'C' appears to lie to the east of a zone of frontal cloudiness in the imagery, which would place it in the warm sector where low-level stratus would be expected.

b. 12 GMT 13 January 1979

The storm center moves northeastward over the largest sea-surface temperature gradient and enters the explosive stage. The general flux pattern (Fig. 5b) is similar to that of 00 GMT 13 January 1979. Maximum features in the positive flux field, identified as 'A' and 'B' in the figure, have become more distinct. This change in the flux pattern

occurs as the circulation associated with the developing cyclone intensifies and begins to dominate the flow pattern to the southwest, as depicted in the 1000 mb wind field (Fig. 5a). Verifying ship reports are not available for this time.

Positive flux feature 'A' has elongated from west to east as the westerly flow to the south of the Kamchatka low now extends farther to the east. This cold, continental flow over the ocean maintains at least a  $-5^{\circ}\text{C}$  air-sea temperature difference to  $180^{\circ}\text{E}$ . Again, the highest flux values are found where the combination of high wind speed and large negative air-sea temperature differences are located. The magnitude of the maximum which stretches to nearly  $170^{\circ}\text{E}$  ( $600 \text{ W/m}^2$ ) may be an overestimate through alteration of the drag coefficients by the oscillating boundary layer in this area.

A comparison with the sensible heat flux field from the previous time indicates that the model correctly diagnoses smaller fluxes where this westerly flow weakens along the coast of Sakhalin Island. This coastal maximum is decreased from approximately  $1300 \text{ W/m}^2$  to  $900 \text{ W/m}^2$  due to a 10 m/sec to 20 m/sec slackening of the wind in the region, while the air-sea temperature difference remains unchanged.

Feature 'B' of Fig. 5b has also become elongated in the east-west direction and the maximum flux value has decreased in magnitude. The northerly flow, which breaks

off from the cold airstream to the south of Kamchatka, broadens to the east as more of this flow is pulled into the vicinity of the storm center by the increased storm circulation illustrated in Fig. 5a. This northerly flow brings cold air due south across the sea-surface temperature gradient. The effect of this flow on the magnitude of the flux feature is diminished by the intrusion of tropical air to the east of the storm center. The location of the flux maximum of  $500 \text{ W/m}^2$  to the east of Japan is coincident with the position of the maximum air-sea temperature difference in the area ( $-15^\circ\text{C}$ ). The southern finger of feature 'B' is a manifestation of the colder, westerly flow which passes to the south of Japan with a windspeed maximum in excess of 27 m/sec.

The positioning of the negative flux feature 'C' in the figure is consistent with the previous period. Strong southerly flow is still indicated in Fig. 5a to the east of the developing cyclone, but the magnitude and extent of the windspeed maximum has decreased and its position has shifted to the northeast. The negative sensible heat flux maximum is decreased from the previous time and its position is shifted to the northeast, which is consistent with the changes in location and magnitude of the wind speed and positive air-sea temperature difference.

Visual satellite imagery from 1405 GMT 13 January (Fig. 12) clearly indicates the presence of cloud streets and open-cell cumulus in the cold air streams over both



positive sensible heat flux features in Fig. 5b. The negative flux feature to the southeast of the storm center is properly located in the warm sector to the east of the main frontal cloudiness depicted in the imagery.

c. 00 GMT 14 January 1979

The storm center continues to move northeastward, but is still located over the region of strongest sea-surface temperature gradient. Explosive cyclogenesis continues and the cyclonic circulation increases, with a wind speed maximum of 30 m/sec (Fig. 6a).

The diagnosed flux field (Fig. 6b) merges the two major positive features (A and B) as the cyclone moves toward the dominant Kamchatka system and its circulation joins in the cold flow to the west of the developing storm center (Fig. 6a). The  $800 \text{ W/m}^2$  maximum in feature 'B' (in the vicinity of  $45^\circ\text{N}$ ,  $165^\circ\text{E}$ ) is driven by the strong (15 m/sec) northerly flow of the storm circulation. The presence of this flow in an area with an air-sea temperature difference of approximately  $-15^\circ\text{C}$  supports the location of the flux maximum, although the magnitude is probably too high as noted previously. Ship reports from this region indicate that the observed air-sea temperature difference was approximately  $-12^\circ\text{C}$  and the wind speed was 12 m/s, which supports the ECMWF analyses.

Feature 'A' now extends across the North Pacific to Alaska, and accompanies the westerly flow which is present

in this region. The magnitude of this flux is decreased to the east, which reflects the diminished air-sea temperature difference as the cold air has been modified by the long path length over the ocean. It seems that the magnitude of this flux feature has been overestimated to the east of 180°E, but the moderate winds (10 m/sec) and relatively large air-sea temperature difference (-8°C) which extend into this area support the model flux diagnosis. Ship reports in the area generally support the computed air-sea temperature difference (observed: -4° to -8.3°C) and ECMWF wind speed (observed: 6 to 15 m/s).

A negative maximum of approximately 300 W/m<sup>2</sup>, identified as feature 'C' of Fig. 6b, is located on the eastern side of the developing cyclone. As in the previous cases, a strong southerly flow is driven by the large-scale circulation. This flow is located between 160°E and 170°W in the figure. It carries warm, moist tropical air over the colder ocean in the vicinity of the storm center, and results in positive air-sea temperature differences. Comparison of the figures shows that the negative flux maximum is located in the same position as the highest wind speeds (30 m/sec) over an area of positive air-sea temperature difference. It appears that the diagnoses of the presence of this feature is consistent with the analyzed low-level circulation for this time. No ship data are available for comparison in this area.

Visual satellite imagery from 0023 GMT 14 January 1979 (Fig. 15) shows extensive open-cell cumulus coverage above 45°N. This region corresponds to the upper portion of the positive flux feature in Fig. 6b. More open-cell cumulus is indicated in the imagery to the west of 165°E between 30°N and 35°N, which corresponds to the southern portion of the positive flux feature. The flow pattern in the vicinity of sensible flux maximum 'B' (40°N, 160°E) is distorted by a polar low which has propagated into the area from the west. However, it appears that open-cell cumulus verifies in the imagery at this location as well. IR imagery (Fig. 16) indicates the presence of closed-cell cumulus in the southern portion of negative flux feature 'C' to the east of the main frontal clouds which is consistent with the negative flux diagnoses. However, it appears that most of the region of diagnosed negative flux is covered by the main storm cloudiness.

d. 12 GMT 14 January 1979

The cyclone continues to grow explosively, and reaches peak intensity near this time. Fig. 7a illustrates a markedly different 1000 mb wind pattern to the north of the cyclone center from that previously analyzed. The westerly cold stream which has persisted to the south of Kamchatka is interrupted by the northward movement of this well-developed-cyclone, which is now positioned on the cold side of the sea-surface temperature gradient. Consistent with

the absence of the westerly cold stream to the north of the storm center at 1000 mb, the model diagnoses minimal sensible heat flux in this region, as illustrated in Fig. 7b. A weak, positive flux feature, identified as 'A' in Fig. 7b, is located to the west of the storm center. This maximum results from the 15 m/sec to 25 m/sec winds which separate from the relatively cold, southwesterly flow at about 48°N, 170°E. The positive 500 W/m<sup>2</sup> maximum to the south of Kamchatka is driven by the continental flow as it departs the coast at this higher latitude.

Feature 'B' of the figure identifies a very large and unrealistic negative flux maximum of more than 700 W/m<sup>2</sup> to the southeast of the storm center. This anomalous feature appears to originate with the ECMWF analyses rather than model error. Excessive windspeeds of greater than 50 m/sec have been analyzed in the southerly flow in this region. The model diagnosis seems consistent with this large magnitude of tropical flow in an area of positive air-sea temperature difference (8°C). Ship data are not available from this area for comparison.

Open-cell cumulus verifies in the visual imagery from 1205 GMT 14 January 1979 (Fig. 18) for the region of positive flux feature 'A' in Fig. 7b (65°N-45°N, 160°E-175°E). The IR imagery (Fig. 19) shows extensive closed-cell cumulus and stratus coverage in the warm air to the east of the frontal zone above 20°N. This area generally corresponds to the

region of negative flux diagnosed by the model. However, most of this diagnosed negative flux feature is covered by the main storm cloudiness.

e. 00 GMT 15 January 1979

The storm has occluded over the cold water in the vicinity of the Aleutian Islands at this time. A cyclone which has formed to the southwest of the storm center, and an anticyclone which is located to the southeast, tend to force a southerly flow into the storm region, as illustrated in Fig. 8a.

A negative flux feature of approximately  $200 \text{ W/m}^2$  is located to the southeast of the storm center. This feature is a consequence of the strong southwesterly flow (35 m/sec) to the southeast of the storm center, which is forced by the circulation of the incipient system and the large anticyclone to the southeast. Verifying ship observations are not available from this area. A comparison of the figures indicates that this maximum is located where the southerly flow splits just to the southeast of the storm center, in the region where maximum wind speeds of 20 m/sec to 25 m/sec occur. The positive air-sea temperature difference has been decreased due to the modification of the air as it reaches this high latitude. The presence and extent of this negative flux feature appears to be dominated in the model by the magnitude of the wind.

The location of the positive sensible heat flux feature to the west and south of the storm center, identified

as 'A' in Fig. 8b, is determined by the southwesterly and westerly flow in the vicinity of 50°N. This moderate, modified-continental flow serves as the source of the cold air to the west of the storm center and maintains a small negative air-sea temperature difference in the region. The small temperature difference and the general weakness of the flow leads to a model diagnosis of fluxes of  $100 \text{ W/m}^2$  or less to the west of the storm center. It is interesting to note that this feature begins to wrap around the storm center to the south for the first time. The intrusion of this feature into this area of the storm is indicative of the occlusion process which is taking place at this time.

f. Sensible Heat Flux Summary

The model boundary layer parameterization leads to diagnoses of sensible heating that are consistent with the forcing represented in the ECMWF analyses. The positive fluxes are confined to the cold air behind the front, which conforms to Petterssen's general cyclone model, and negative fluxes are located in the warm, tropical air to the east. The flux maxima are consistently placed where the greatest air-sea temperature difference and boundary layer windspeed coincide.

The magnitudes of the fluxes generated by the model seem to be excessive. The amount of positive flux is affected by discrepancies in the ECMWF analyses, as well as the artificial increase in the drag coefficients where the

boundary layer is collapsed by the model. The unrealistic magnitudes of the negative fluxes present in some of the fields appear to be related to spurious ECMWF 1000 mb wind analyses and the large positive air-sea temperature differences determined in these areas.

Maximum sensible heat flux values found by other investigators are included in Table I for comparison purposes. These values were compiled by Gall and Johnson (1971) with an addition from Bosart and Lin (1984). Units have been converted to  $W/m^2$  where applicable. The magnitude of the flux produced by NOGAPS is of the same order as that determined by previous investigators, and may be representative of the intense nature of this cyclone.

## 2. Cloud Verification

Storm-related composite cloud features, as generated by the model, are compared to Defense Meteorological Satellite Program (DMSP) imagery at each analysis time. The discussion focuses on three general model cloud forcing categories. These categories are convective, large-scale and cumulus, where cumulus identifies the open-cell cumulus and cloud streets that are diagnosed as layer-six, large-scale clouds in the model. Cumulus occurs where the sensible heat flux maxima are located, as discussed in Section C of this chapter.

### a. 00 GMT 13 January 1979

Visual and infrared (IR) imagery for this time are included as Figs. 9 and 10. The composite convective and large-scale clouds are mapped in Fig. 11.

(1) Convective Clouds. The major cloud feature associated with the system at this time is identified as 'A' in the figures. The convective cloud map (Fig. 11a) denotes a narrow band of convection which penetrates three sigma levels to the west of the storm center. A comparison of the visual and IR satellite imagery shows that significant convection did occur in the vicinity of the storm center at this time. However, much of this convection is located to the east of the center in an area roughly bounded by 32°N to 41°N and 150°E to 160°E. The clouds that are present to the northeast of the storm center in the imagery are not diagnosed as convective by the model.

An extensive band of convection is indicated to the east of the storm and is identified as feature 'B' in the figures. The IR imagery of Fig. 10 indicates that deep convection with low cloud-top temperatures occurs along the entire length of this band. The model correctly diagnoses deep convection which extends through four sigma levels as illustrated in the cloud map, but displaces it approximately 10 degrees to the west of the feature present in the imagery. The displacement of this feature is consistent with that observed in feature 'A'.

(2) Large-Scale Clouds. The IR imagery indicates that low-level clouds are present to the east of the storm center in the same region where large-scale cloudiness is diagnosed by the model (centered at approximately 34°N,



156°E). The three-level, large-scale cloud feature located north and northwest of the storm center appears to be representative of the clouds present in this region of the satellite imagery. This cloud location with respect to the storm center infers large-scale cloud development as the tropical flow, now involved in the developing cyclone circulation, overrides the colder air to the north. The depth of the clouds generated by the model in this area is consistent with the moderately low cloud-top temperatures indicated in the IR imagery. The model diagnoses of the large-scale process in the warm air to the east and northeast of the storm center appear to be representative, although the area coverage of the large-scale clouds observed in the imagery is more extensive than produced in the model. This difference in coverage may be due, in part, to inactive clouds which are present in the imagery, but can not be diagnosed by the model.

(3) Cumulus. The westward and northward extent of feature 'A' of Fig. 11b can not be verified by the imagery, but occurs where the cold air separates from the westerly flow to the north, and is caught in the circulation of this system. This portion of the large-scale cloud feature is co-located with an area of sensible heat flux maximum, and is more than likely representative of the open-cell cumulus. The extensive region of single level large-scale clouds to the north of the storm center (above 40°N) in the figure is

generated under similar conditions. In this area, the visual imagery clearly shows the presence of the open-cell cumulus in the cold, westerly flow streaming off Sakhalin Island. The presence of this cumulus in an area where low-level large-scale clouds are indicated supports the scenario of the boundary layer behavior as described in Section C.

b. 12 GMT 13 January 1979

The visual and IR satellite imagery for this time are shown in Figs. 12 and 13. Convective and large-scale composite cloud maps are displayed in Fig. 14. A more extensive storm-related cloud mass is present in the imagery as the cyclone enters the explosive stage.

(1) Convective Clouds. The satellite imagery depicts an extensive, comma-shaped cloud pattern associated with this cyclone, with significant convection occurring in the vicinity of the storm center. The tail of the comma extends from about 35°N southeast to 20°N. The IR imagery indicates that deep convection occurs in a narrow band, roughly 120 n mi in width, along the front edge of the tail. The convective cloudiness, as mapped by the model, displays a relatively deep and extensive pattern in the vicinity of the storm center. Portions of this model feature to east of 165°E extend beyond the coverage of the imagery.

A comparison of the imagery and the convective cloud map, Fig. 14a, reveals that the moderate storm convection to the west of the center, identified as feature 'A' in the figures, is represented accurately by the model.

As in the previous time, convection is not indicated to the northeast of the center where significant deep cloud coverage is shown in the imagery. The model also overestimates the extent of the convective activity in the frontal band. The model diagnoses convection (Fig. 14a) extending through four sigma levels over a much broader region than can be supported by the imagery in this zone. The positions of areas of deep convection that are displayed in the imagery and cloud map correspond well. This comparison indicates that the model diagnosis is basically correct, although the modeled clouds are extended too far to the east. The extensive area of convective coverage farther to the south is considered a model anomaly. Overestimation of convection by the model along the southern border is present at each of the subsequent times. This behavior is described in more detail in Subsection D.3 of this chapter.

(2) Large-Scale Clouds. Model-diagnosed, large-scale clouds are present in one to three sigma levels to the east and northeast of the storm center. This position and area of coverage are consistent with what is observed in the imagery for this region of the cyclone. Low cloud-top temperatures inferred from the IR imagery indicate that these clouds are not shallow, which supports the multi-level model diagnoses. As noted previously, the model correctly associates this cloudiness with the large-scale tropical flow in the region. When this cloud feature is combined with the

convective map, a representative depiction of the cloudiness as observed in the imagery is produced.

(3) Cumulus. The single-level, large-scale cloudiness to the west and northwest of the storm center (Fig. 14b) corresponds to the location of the sensible heat flux maximum in the storm area. The visual imagery shows that open-cell cumulus is present in the cold air streaming behind the front in this area. A similar open-cell cumulus pattern is indicated to the north of this system where single-level, large-scale clouds are mapped over the sensible heat flux maximum in the westerly flow off Siberia. The diagnosis in these areas where the oscillating boundary layer behavior was observed is consistent with the expected treatment of the open-cell cumulus by the model.

c. 00 GMT 14 January 1979

The visual and IR satellite imagery is included as Figs. 15 and 16. The convective and large-scale composite cloud maps are included as Fig. 17. The satellite imagery for this time illustrates the continued development of this system, with enhanced cloud cover extending above 40°N.

(1) Convective Clouds. As in the previous analysis times, the region of most extensive deep cloud coverage to the northeast of the storm center is not identified as convective. The cloud pattern generally maintains a comma shape with more organized deep convection to the west and northwest of the storm center (Fig. 16). A much broader

band of deep convection is present in the frontal zone extending to the southwest. The structure of this frontal convection is diagnosed correctly by the model. A comparison of Fig. 17a with the IR imagery shows that the model provides a representative display of the orientation, depth and extent of the frontal convection as it occurred above 30°N. However, the overall feature is displaced between five and ten degrees to the west of the frontal feature observed in the satellite imagery. A similar displacement is also noted in the 00 GMT 13 January 1979 convective field. It appears the convective process is overestimated to the south of 30°N.

The small disturbance which is entering the storm region from the west is identified as feature 'A' in the satellite imagery. This disturbance may be captured in feature 'A' of the model diagnosis (Fig. 17a). The three-level convection indicated by the model is consistent with the moderately low cloud-top temperatures inferred from the IR imagery. The leading edge and northward extent of this feature are well positioned by the model, but the overall area coverage is too extensive. A second possibility is that this diagnosed convective cloud area is a western displacement of convection associated with the major cloud system.

(2) Large-Scale Clouds. The diagnosis of the large-scale clouds (Fig. 17b) is similar to the previous analysis time. Multi-layered large-scale clouds are indicated to the north and northeast of the storm center in the

satellite images. The model diagnoses large-scale clouds at up to four sigma levels where some of the deepest clouds are present in the satellite imagery. The single-level, large-scale feature, identified as 'B' in the figures, corresponds to the position of the low-level stratus present behind the frontal band (see especially Fig. 16).

(3) Cumulus. The single-level, large-scale cloud feature to the west and northwest of the storm center in Fig. 17b is coincident with the sensible heat flux maximum diagnosed at this time. The visual imagery indicates the presence of some open-cell cumulus to the west of the storm center and an abundance of this cloud type to the northwest. This cumulus distribution falls within a region diagnosed by the model as having low-level, large-scale clouds. This treatment of the open-cell cumulus is consistent with the previous evaluation times.

d. 12 GMT 14 January 1979

The visual and IR satellite imagery for this evaluation time are given in Figs. 18 and 19. The convective and large-scale composite cloud features are mapped in Fig. 20. The visual imagery indicates that the cyclone is well-developed. The storm center is now completely surrounded by an extensive cloud mass except for an area of cold air penetration from the south.

(1) Convective Clouds. The IR satellite imagery displays moderate convection in the vicinity of the storm

center. Deep convection occurs to the east and along two bands in the frontal zone, where it appears that a secondary front has formed. The disturbance that was previously noted to the west has developed considerably during the previous 12 h. This disturbance is now located to the southwest of the storm center and is identified as feature 'A' in the figures. A comparison of the imagery and the convective cloud map again shows that the deep clouds to the east and northeast of the storm center are not identified as convective by the model. The convective feature that is associated with this cyclone and that of disturbance 'A' have been merged by the model to the west of the storm center (Fig. 20a). The east-west and north-south extent of feature 'A' has been exaggerated in the model in comparison with the satellite imagery. The position of the frontal band (Fig. 20a) corresponds very closely to that of the secondary front in the IR imagery. The band of deep convection to the east of this frontal feature is not represented in the model display.

(2) Large-Scale Clouds. The model-generated, large-scale cloud map again complements the convective map. As in previous times, multi-layered, large-scale clouds are positioned to the northeast of the storm center. However, the diagnosed area coverage of the cloudiness in this region is much less than observed in the satellite imagery. The location of the large-scale clouds in the frontal band (Fig. 20b) produces a very representative display of the position of the

observed cloudiness, especially in the eastward extent of the frontal band. For the first time, multi-layered (three level) large-scale clouds are located in the frontal zone. The presence of these clouds in the model is supported by the deep clouds that are located in this region of the IR imagery, and may be indicative of greater large-scale frontal activity as the storm reaches its peak intensity. Most of the frontal clouds are diagnosed as single-level however, and can not account for the deep penetration indicated in the IR imagery to the east of the storm center. Low-level clouds are present throughout the frontal band in the IR imagery, as well as in the warm sector to the east. The broadening of the large-scale frontal feature in the model cloud map to the north of 40°N appears to capture some of this warm sector stratus.

(3) Cumulus. The single-level, large-scale cloud feature, identified as 'B' in Fig. 20b, corresponds to the position of the positive sensible heat flux maximum. The location of the open-cell cumulus, as shown in the imagery, is primarily to the northwest of 50°N, 170°E. Only the northwest corner of feature 'B' verifies as open-cell cumulus, with the remainder of the feature occupied by the main cloud cover of the cyclone. The open-cell cumulus to the north of 55°N in the imagery also is not captured in the model diagnoses. The small finger of feature 'B' which extends to the east and connects the body of the feature with the storm center, is not located in an area of positive flux. The IR



imagery indicates that the clouds in the cold air in this area are limited to the low level and are probably large-scale in nature. Convection would be impeded in this area by the presence of the positive air-sea temperature difference.

e. 00 GMT 15 January 1979

Satellite imagery for this time (not shown), and the previous analysis of this system by Calland (1983) shows that the cyclone has entered the occluded stage.

(1) Convective Clouds. The convective cloud map (Fig. 21a) indicates that no storm-related convective clouds are diagnosed by the model. The large area of convection which is mapped to the west of the storm center is associated with the second disturbance previously mentioned. The diagnosis of no convection at this time seems extreme in light of satellite imagery from this period and later periods which indicates that the system retains a considerable cloud pattern. However, this diagnosis is consistent with the occluded nature of the cyclone. The storm has moved over much colder water and the convective process has been effectively shut off in the model.

(2) Large-Scale Clouds. The large-scale cloud features (Fig. 21b) do indicate that extensive cloud cover is still associated with this system. This large-scale pattern about the storm center includes multi-layered clouds to the north and northwest, and a blurred, single-level

frontal zone curving to the southwest. This pattern and general coverage are very similar to that observed in the satellite imagery for 1005 GMT 15 January 1979 (not shown).

(3) Cumulus. The model behavior in the region of positive sensible heat flux appears to be similar to that of the previous times. The large-scale cloud feature in the cold air to the south, west and northwest of the storm center is positioned where the maximum positive sensible heat flux has been diagnosed by the model. Open-cell cumulus verifies in this region of the imagery.

#### f. Cloud Comparison Summary

The model-generated convective cloudiness is generally representative of the storm environment as verified by the satellite imagery. The outbreak of convection in the vicinity of the storm center and the deep convection over the frontal surfaces are correctly diagnosed. However, there is a tendency to displace or extend these features several degrees to the west of the verifying position.

The open-cell cumulus and cloud streets located in the cold air streams are treated as large-scale convection in the NOGAPS boundary layer parameterization. If this interpretation is accepted, the generation of this cloud type is handled well by the model.

Large-scale clouds are consistently placed to the north and northeast of the storm center, as well as along the frontal surfaces. The most extensive cloud mass is observed in the imagery in these areas during the period of cyclone

growth. The identification of large-scale cloud forcing in these cyclone regions appears correct. When the model output from the three forcing categories is combined, a reasonably accurate depiction of the storm clouds which are present in the imagery is produced.

### 3. Cumulus and Large-Scale Cloud Model Heating Rates

The rate of condensation heating in each model sigma layer is a sum of the heating from the existing cloud types. Precipitation rates are combined in the model to produce a total precipitation field for each evaluation time (not shown).

Temperature tendencies from latent heat release for the six sigma layers are averaged to produce a column temperature change from cumulus and large-scale precipitation. The layer temperature changes are weighted by the thickness of the individual layers prior to column averaging. It should be noted that the large-scale clouds are confined primarily to the lowest two sigma layers, while the deep convective clouds extend well into the upper layers of the atmosphere. Column averaging is more meteorologically significant for convective condensation heating, because of the greater vertical extent of this cloud type. Averaging of the large-scale heating field artificially spreads its low-level contribution over the column. However, column averages allow a consistent comparison between the two precipitation sources and indicates the relative contribution of large-scale condensation heating to the total column temperature change.

A general feature which is noticed at all times is the excessive convective heating rates that are generated along the southern border of the figures. Here the model apparently responds to the tropical air and produces large areas of anomalous deep convection.

In his semi-prognostic test of the Arakawa-Schubert cumulus parameterization, Lord (1982) found that the model-generated cumulus warming of the column and associated precipitation rates closely matched observations. His profiles of cumulus warming and time series of precipitation from cases of moderate tropical convection generally gave column-averaged layer heating rates of less than 5 deg/day and time-averaged precipitation rates of 10 mm/day to 20 mm/day. Low-tropospheric values of cumulus warming ranged between approximately 3 deg/day to 6 deg/day. The maximum precipitation rates observed were about 35 mm/day.

a. 00 GMT 13 January 1979

The convective and large-scale condensation heating fields are illustrated in Fig. 22. At this early stage of cyclone development, the largest extent of heating is provided by the large-scale processes as shown in Fig. 22a. The low-level heating rates for this area are about 2.5 deg/day, which compares favorably with the GATE observations used in Lord's study.

Storm-area convective heating (Fig. 22b) is confined to a small area to the west of the storm center, with

a column-averaged rate of about 5-10 deg/day. This heating is also consistent with Lord's findings for cases of moderate convection. The large feature to the east of the storm center indicates convective heating in excess of 30 deg/day to the north of 30°N. The convective heating rates to the south of this latitude are excessive and unrealistic.

b. 12 GMT 13 January 1979

A large-scale column average condensation heating maximum of 0.5 deg/day is indicated to the west of the storm center in Fig. 23a, which actually is associated with a maximum heating rate of 2.5 deg/day in the lowest layer only. The bulk of this heating is derived from the open-cell cumulus, which verifies for this area in the imagery. The 3.0 deg/day heating feature to the east of the storm center reflects a single gridpoint diagnosis which has been contoured as an area.

The storm center is adjacent to an area of convective heating with a column-averaged maximum of 30 deg/day. This convective heating appears to be excessive, but is supported by a surface precipitation rate of approximately 12 cm/day. Although this rate is much higher than in Lord's study, it is not unbelievable given the explosive nature of the cyclone. An area of much greater heating is present in the feature below 28°N. This excessive heating is produced by the anomalous convection along the southern portion of the grid mentioned previously.

c. 00 GMT 14 January 1979

Large-scale condensation heating occurs to the west, northwest and northeast of the storm center (Fig. 24a). The column-averaged heating rate maximum for the region to the west is approximately 2.5 deg/day. Since this heating area corresponds to the moderate convection of the open-cell cumulus in the cold air behind the storm center and to the north, it appears that the model calculations are of the correct magnitude.

The convective precipitation heating rates (Fig. 24b) are in excess of 30 deg/day in the frontal region of the cyclone. This heating rate seems excessive, as in the previous evaluation time, but it is supported by a diagnosed surface precipitation rate maximum of approximately 16 cm/day. This precipitation rate is almost 4.5 times greater than the maximum observed by Lord (1982). An increase in the heating rate can be identified in this field at about 31°N which separates the storm frontal convective heating from the region of anomalous heating to the south.

d. 12 GMT 14 January 1979

The maximum in the large-scale heating field (Fig. 25a) is located in the frontal zone to the southeast of the storm center. The actual low-level heating rate for this area is 6 deg/day, which is reasonable given the intensity of the system.

The magnitude of the convective heating is significantly reduced (Fig. 25b) over previous times. A distinction

can be made between the storm area heating and the excessive anomalous heating to the south in this field, as in the previous analyses.

e. 00 GMT 15 January 1979

The large-scale, column-averaged condensation heating rate is realistically diagnosed as 1.0-1.5 deg/day in the frontal zone, and 0.5-2.0 deg/day to the west and southwest of the storm center. The positioning of this large-scale heating properly accounts for the contribution of the open-cell cumulus in this area.

No convective heating is indicated by the model in the vicinity of the storm. This behavior is a reflection of the occlusion process which has been correctly diagnosed by the model. The convective heating field (Fig. 25b) shows a region of intense heating to the south of the storm center. This heating feature can be attributed to the second disturbance which has moved into the area, but may also include some of the anomalous heating that is observed at every other evaluation time.

f. Condensation Heating Summary

The column-averaged, convective condensation heating rates in the frontal zones were found to be approximately 30 deg/day, which appears to be high, but is not inconsistent with the surface precipitation generated by the model in the storm area. Surface precipitation on the order of 10 cm/day is not implausible given the intense nature of this cyclone.

Therefore, the large frontal convective heating rates diagnosed by the model are probably representative of the FGGE forcing. Convective heating is definitely overestimated along the southern borders of the domain. It seems that the model is responding to both the tropical environment and the southern boundary in these regions. It is noted that NOGAPS does not see a boundary of this type in an operational run. The overestimation along the border therefore, is probably an artificial inducement not representative of NOGAPS performance.

Large-scale heating is well represented by the model, especially where open-cell cumulus and cloud streets are present. In general, the low-level temperature change rates correspond to those reported by Lord (1982), and the range of the column-averaged temperature change rates (0.5-2.5 deg/day) is physically reasonable for this category of cloud forcing. The largest contribution of large-scale condensation heating was properly diagnosed in the frontal regions during the last two evaluation times when the cyclone reached peak intensity. Column-averaged heating rates in regions where cloud streets and open-cell cumulus verified in the imagery were consistent with Lord's results for cases of moderate convection.



#### IV. ADVECTIVE AND DIABATIC TEMPERATURE CHANGES DURING CYCLOGENESIS

##### A. GENERAL

The diabatic contribution to column temperature change in the storm environment is estimated through the application of a quasi-Lagrangian thermodynamic energy budget and from the NOGAPS diabatic diagnostics. The equation employed in the budget routine is derived from the first law of thermodynamics using the potential temperature as described by Holton (1979),

$$\frac{\dot{q}}{C_p} = \left[ \frac{\partial \ln \theta}{\partial t} + \mathbf{V} \cdot \nabla \ln \theta + \omega \frac{\partial \ln \theta}{\partial p} \right] \times T \quad (3)$$

In (3),  $\dot{q}$  is the diabatic heating,  $C_p$  is the specific heat at constant pressure, term 1 is the 12-hour time tendency of  $\ln \theta$ , term 2 represents the horizontal advection, term 3 is the vertical advection, and  $T$  is the temperature in the layer. The units of  $\dot{q}/C_p$  are K/day.

The first procedure is to infer the right side of (3) using the quasi-Lagrangian budget technique as discussed by Calland (1983). The second procedure is to estimate the contribution of this heating term from the diagnostic results of the NOGAPS heating package.

The storm-area diabatic temperature changes are computed by layer and averaged to produce column diabatic temperature

change for the storm volume. Column-averaging permits a direct comparison of the budget results in isobaric coordinates with NOGAPS results in sigma coordinates, and yields a more accurate representation of the net effect of the thermal processes in the storm volume. Weighting factors are applied to layer heating values to normalize the results to a standard 100 mb layer prior to column-averaging. The weighting factors that are applied to the budget pressure layers and the NOGAPS sigma layers at 12 GMT 13 January are listed in Table II for illustration. Date-times that are included in the figures represent 12-h time periods. For example, 1206 refers to 00-12 GMT 12 January 1979.

## B. THERMODYNAMIC ENERGY BUDGET CALCULATION

### 1. Procedure

The quasi-Lagrangian thermodynamic energy budget program includes interpolation of the basic observed variables of temperature, horizontal velocity and vertical velocity to a given storm volume in increments of one degree radii from the storm center. Observed temperature tendencies, horizontal temperature advection and vertical temperature advection are determined from these interpolated fields. The budget terms are area-averaged by layer over the storm volume.

#### a. Finite Differencing and Averaging

Locations of the variables in the budget computation are displayed in Fig. 27a. The budget terms are

structured to produce layer results. Temperatures and velocities are averaged to the center of each layer except where vertical advection is determined. The vertical advection computation uses a layer-averaged omega, but carries the level temperatures to allow the finite difference  $(\partial \ln \theta / \partial P)$  to be centered in the layer. The final form of the budget equation is:

$$\frac{1}{C_p} \frac{d\bar{\theta}}{dt} = \left( \frac{d\bar{\ln \theta}}{dt} + \bar{V} \cdot \nabla \bar{\ln \theta} + \bar{\omega} \partial \ln \theta / \partial P \right) \times \bar{T} \quad (4)$$

where the terms are as defined previously and the overbars indicate layer and area averages, and  $V$  is the wind velocity relative to the storm.

ECMWF temperature analyses are available at 00, 06, 12 and 18 GMT for each day. Because of the possible errors in the 06 and 18 GMT potential temperature analyses (Calland, 1983) only the 00 and 12 GMT analyses are utilized in this study. Time resolution is sacrificed for added confidence in the temperature time tendencies using the 00 and 12 GMT data.

The time difference of  $\ln \theta$  is determined between adjacent observations as illustrated in Fig. 27b. The diabatic temperature change results are determined from the 00 and 12 GMT analyses and are valid for the 12 h period centered at 06 and 18 GMT due to the centered time differencing and the time-averaging of the advection terms. Vertical time

sections are constructed using the weighted results from 06 and 18 GMT for the period 12-14 January 1979.

b. Data

Kinematic vertical velocities are used in the budget calculation because the ECMWF FGGE vertical velocities are not the product of direct analysis, but are determined during the initialization step of the 4-dimensional data assimilation technique employed at ECMWF (Bengtsson, et al., 1982). The kinematic fields are chosen to ensure that the horizontal and vertical velocities, as well as the vertical finite differencing of the thermodynamic energy equation, are consistent with the continuity equation. The magnitude of the kinematically-derived omega is nearly two times that of the initialized FGGE omega.

Mandatory-level temperatures are vertically averaged (linear on pressure) to obtain layer mean temperatures. These temperatures were determined during the initialization phase of the data assimilation cycle at ECMWF. To determine the magnitude of the differences between the initialized and analyzed thermal structures, the ECMWF layer temperatures are compared to equivalent layer temperatures computed by the hypsometric equation using the ECMWF height field. These heights are determined during the analysis cycle of the data assimilation. A comparison of these two temperature fields lends confidence to the ECMWF level temperature data in the troposphere in the vicinity of the developing

cyclone. Temperatures determined by the two methods for the 500-700 mb layer at budget radius 6 are displayed in Fig. 28. These temperatures are generally in agreement, but some significant differences do exist. A 2.5 K difference is present in Fig. 28 at time period 6. Departures of this magnitude may adversely affect the budget calculation.

The largest deviation between the two temperature fields is found in the stratospheric layers, which suggests a problem with the ECMWF initialization in the upper three levels. The average deviation between the ECMWF and calculated temperatures in the troposphere is 0.84 K. The average stratospheric deviation is 2.73 K. The largest single departure in the troposphere is 3.0 K, while the maximum stratospheric departure is 7.3 K. The RMS difference between the initialized and calculated layer temperatures at radius 6 for all levels at all times is 1.86 K. The initialized ECMWF temperatures were elected for the budget calculations to be consistent with the NOGAPS diagnosis, which was performed with this data.

Since the analyzed temperatures are only carried at discrete levels, the model lapse rate will smooth out inversion features within the layers. This smoothed lapse rate could potentially introduce errors into the budget calculation, but the effect is greatly reduced through column-averaging.

### c. Heating and Temperature Change

The budget residual represents a layer temperature change in units of K/day due to diabatic heating and accumulated errors in the budget calculation. This temperature change is expressed in per unit mass (Kg) and is proportional to the amount of heating ( $\dot{q}$ ) applied to the layer. These temperature changes cannot be compared directly because the layers in the column are of varying thickness (mass). To compare temperature change rates from layers of unequal mass, all layer temperature change values are normalized to a standard layer of 100 mb thickness. The resulting weighted temperature tendencies are not indicative of the actual sigma or mandatory layer temperature changes which occur, but are proportional to the amount of heating that is applied vertically to the storm volume.

Column-averaged temperature change rates are computed by vertically summing the weighted layer temperatures and dividing by the sum of the weighting factors. The result of this calculation is representative of the actual average column temperature change rate; assuming the budget calculation is free of errors.

### 2. Budget Analysis

Vertical time sections of the results from the budget calculation are analyzed for the inner and outer storm volumes of six and ten degree radii, respectively.

#### a. Temperature Time Tendency

The temperature tendency term for the inner volume (Fig. 29a) shows a temperature increase through the column to 175 mb during the first two time periods. Most of the calculated temperature increase is confined to the low levels with a maximum at 775 mb at 1218. A weaker area of upper-level increase is reflected during this period as well. This calculated temperature increase precedes the onset of explosive cyclone development by approximately 12 h. The location and distribution of this temperature increase reflects forcing which will enhance cyclone intensification.

Negative values dominate the tropospheric temperature tendency during all periods after 1306. This feature is expected in the lower troposphere as the storm center moves northward into colder air. The zero contour which marks the top of this negative tendency feature can be treated as an indicator of tropopause behavior. The tropopause lowers between 1318 and 1406, indicating that the storm center transits into a colder air mass during these periods. The large negative maximum ( $-22.5$  K/day) present at 1406 occurs concurrently with the movement of the storm across the atmospheric and oceanic baroclinic zone. This maximum reflects the large low-level volume temperature change which occurs as the cyclone moves rapidly into the cold air. The location of this negative temperature tendency maximum at 600 mb places it within the cold dome as well.

The vertical extent of the negative temperature tendency during the explosive period is inconsistent with continued cyclogenesis. The temperature changes represented in Fig. 29a suggest that the column contracted during the period of most intense development, when the opposite should have occurred. Although negative temperature tendencies were expected in the lower troposphere as the storm moved north, the lack of compensating warming in the upper levels is suspect. Previous evaluation of the initialized ECMWF temperature fields indicated that some discrepancies exist in the upper-level temperature analyses. These temperature discrepancies may have contaminated the budget tendency term in the upper levels.

The temperature tendency time section for the outer budget volume (Fig. 29b) is similar to that of the inner volume. Many of the features have been smoothed and reduced in magnitude, which reflects the averaging over a larger region.

#### b. Advective Temperature Tendency

The advective tendency term at the inner volume (Fig. 30a) generally indicates a strong temperature decrease in the lower troposphere with a weak increase in the upper layers. Initial upper-layer positive temperature advection is centered at 275 mb. Horizontal warm advection dominates the upper-layer advective temperature tendency until explosive development becomes established after 1306. The sign



of this term within the troposphere is then determined by the increased magnitude and extent of the negative tendency due to vertical advection.

The strong lower tropospheric negative temperature tendency, which is present throughout the development of this cyclone, is primarily a manifestation of the negative advection associated with the upward vertical velocities in the storm volume. This temperature decrease is consistent with the advective processes affecting the storm volume in the lower layers, but the penetration of the large negative temperature tendency to 200 mb after 1318 would cause excessive local cooling of the column in the absence of diabatic processes. Excessive cooling of the column is inconsistent with continued cyclogenesis, as mentioned previously. The magnitude of this negative upper-layer feature has probably been overestimated by the use of the kinematic omega in the budget calculation.

The advective time section for the outer volume (Fig. 30b) shows significant reduction in the rate of temperature increase in the upper layers above 400 mb. This change in the heating pattern between the volumes suggests that a greater amount of warm advection is concentrated in the upper layers at the inner budget volume.

c. Thermodynamic Energy Budget Diabatic Residual

The residual temperature change time section for the inner budget volume (Fig. 31a) contains several interesting features. Strong lower tropospheric diabatic effects

are indicated at the first two time periods (1206 and 1218), which is consistent with the initial, shallow cyclone growth. This warming feature attains its maximum value at 775 mb during the second time period. The distribution of this heating is consistent with the strong sensible heating and shallow convection during the formative period of this cyclone.

A pause in residual diabatic warming occurs during the third time period (1306). A small amount of cooling is indicated in a layer extending from approximately 500-250 mb. Cooling at these levels during this early stage of cyclone growth is physically unreasonable. A similar pause was noted in the vorticity tendencies by Calland (1983), which suggests that a problem exists at this time period in the ECMWF FGGE analyses.

Diabatic heating is re-established in the column by 1318, except in the lowest layer and above 250 mb. The magnitude of this warming is less than during the early stages of development, but the vertical growth of the feature properly reflects the deeper convection which is present during this period. Although the sign of diabatic heating is correct, the magnitude appears to have been underestimated, considering the amount of convective and large-scale activity associated with the system at this time.

The diabatic cooling feature located in the lower layers after 1306 is not physically reasonable. The budget determination of this cooling results, in part, from inaccuracies in the estimation of the lower tropospheric advection

tendency as the storm transits into a colder air mass between 1318 and 1406. Although thermal gradients are properly resolved at the evaluation times, the 12-h time average of the advection term probably underestimates the true horizontal advection during this period. This artificial decrease in advective cooling after 1318 leads to a less positive diabatic residual in the budget formulation. The 12-h time resolution of the data is not sufficient to resolve the strong thermal advective effects when the cyclone moves rapidly into the cold air.

During the last time period (1418), strong diabatic effects with a maximum at 600 mb are indicated in Fig. 31a. The restriction of this warming feature to the mid-troposphere is consistent with the diabatic process as the cyclone peaks in intensity and then occludes. The magnitude of this feature (35 K/day) seems to be excessive, but may be a reflection of the intensity reached by the cyclone during this period.

Outer budget volume results (Fig. 31b) are again similar to those of the inner volume, except for the smoothing associated with the larger area.

#### d. Column-Averaged Results

The area-averaged, column-averaged temperature changes due to the diabatic residual and advective tendency terms of the thermodynamic energy budget for the inner and outer storm volumes are compared in Fig. 32. During the period 00 GMT 12 January 1979-00 GMT 13 January 1979, the storm

center moves primarily to the east and is relatively near the Asian east coast conventional, rawinsonde and other data sources. The estimation of the horizontal advection tendency is relatively accurate as there is little thermal gradient in the zonal direction, therefore the diabatic residual tendency calculation is believed to be most accurate during the first two time periods. Residual diabatic effects reach a maximum of 8.2 K/day in the column at storm radius 6, and 7.6 K/day at storm radius 10 by 1218. This warming maximum exceeds the maximum advective cooling (-7.7 K/day at radius 6 and -6.8 at radius 10) which is not registered until 1406.

The pause in diabatic warming noted in the vertical time sections at 1306 is reflected in both the diabatic residual and adiabatic results for this time. Residual diabatic effects suffer a sharp, physically unrepresentative decrease between 1218 and 1306. This large decrease in magnitude is most probably the result of a problem in the ECMWF analyses during this period as previously mentioned.

One important inference can be drawn from the results of the earlier, relatively uncontaminated time periods. These results indicate that the magnitude of the contribution of diabatic heating to the total column temperature change is as large or larger than the advective term, which suggests that the diabatic effects are as important as the combined effects of horizontal and vertical advection in maritime cyclogenesis.

### C. DIABATIC EFFECTS ESTIMATED BY NOGAPS

Independent estimates of the total diabatic heating and the component terms generated by the NOGAPS diagnostics package are interpolated to the storm volume and area-averaged. Vertical time sections of the weighted temperature changes are constructed for each of the terms. The weighted NOGAPS diabatic layer temperature changes are column-averaged to produce total column temperature tendencies. These tendencies are compared directly with the thermodynamic energy budget results.

#### 1. Procedure

Diagnostic fields of layer temperature change from total diabatic heating and the component terms of convective condensation heating, large-scale condensation heating, eddy transport of sensible heating, long-wave radiation heating and short-wave radiation heating are generated by NOGAPS from the ECMWF FGGE analyses. The temperature tendencies at the six sigma levels in the NOGAPS model are assumed to be representative of heating in the layers centered on these levels. The sigma value at each interpolated gridpoint is converted to a pressure value using the relationship

$$P = \sigma(P_s - 50) + 50$$

where 50 mb is the top of the atmosphere in the NOGAPS model,  $P$  is the pressure at a given sigma level, and  $P_s$  is the surface pressure. Pressure layers are constructed around the

converted sigma levels at each gridpoint, and weighting factors are computed to normalize these layers to 100 mb, as before. The pressure layers and associated weighting factors from time 1312 are listed in Table II for illustration. These weighting factors are applied to the interpolated NOGAPS gridpoint temperature change values at their respective levels, and the result is area-averaged over the storm volume.

The NOGAPS temperature changes, which are generated at 00 and 12 GMT, must be time-averaged to be consistent with the thermodynamic energy budget (06 and 18 GMT). Vertical time sections are constructed for the total diabatic temperature tendency and each of the component heating terms. These time sections indicate the magnitude of diabatic heating that is applied to the storm volume by layer during cyclone development. Column averages are calculated from the layer-weighted temperatures as discussed in the previous section.

Total diabatic input ( $W/m^2$ ) to the storm volume is calculated for the NOGAPS results using the column-averaged diabatic temperature tendencies at radii 6 and 10 for 06 and 18 GMT each day. The energy input from NOGAPS latent heat release in the storm volume is calculated separately for comparison with literature. The energy input to the storm volume is determined by

$$\frac{\Delta T}{\Delta t} \text{ (K/day)} \times C_p \text{ (J/Kg-K)} \times \frac{1}{86400} \text{ (day/s)} \times \text{mass (Kg/m}^2\text{)} = \dot{q} \text{ (W/m}^2\text{)}$$

where  $\Delta T/\Delta t$  is the column-averaged temperature change due to the diabatic heating, and the mass is determined for the storm volume from the area-averaged surface pressures. This mass is adjusted for the model atmosphere which has its top at 50 mb. The resulting energy flux values are discussed in the next section.

## 2. Analysis

### a. Diabatic Time Sections

The area-averaged, weighted NOGAPS total diabatic fields for storm radii 6 and 10 are plotted as time sections in Fig. 33. The overall warming feature for radius 6 appears to present a physically reasonable depiction of the diabatic process as it occurs over the growth of this intense cyclone. During the early stage of cyclone development, warming is confined to the lower layers, with cooling indicated above. A similar pattern is present in the diabatic residual from the temperature budget analysis (Fig. 31a) at times 1206 and 1218. The warming shown in Fig. 33a increases in magnitude and vertical extent with time, until a maximum in both is reached at 1318 after the explosive development has been established. The rapid upward extension of diabatic warming through four sigma levels between 1218 and 1306 is consistent with the intense, 12-h vertical development which organizes around the storm center just prior to the onset of explosive deepening. The vertical retreat of this warming feature between 1406 and 1418 indicates that the model diagnoses a

weakening in the diabatic process during this period; and a termination by 00 GMT 15 January 1979. The maximum of diabatic warming leads the peak in storm intensity, which occurs at approximately 1800 GMT 14 January 1979, by 18 to 30 hours. This phase difference between the diabatic heating and cyclone intensification appears to be reasonable if the diabatic forcing is responsible for, or at least is contributing to, the atmospheric response.

The diabatic effect that is diagnosed for the outer storm volume in Fig. 33b is very similar to that of the inner storm volume, except that it has been smoothed and reduced in magnitude from averaging over a larger region. This similarity in the diabatic term between the storm volumes indicates that the most significant diabatic heating is not confined to the inner storm volume, but is spread over a much larger region around the storm center. The only significant difference in the heating time sections between the storm volumes is in the location of the warming maximum at radius 10, which has been shifted forward by 6 hours to time period 1318. This shift is later shown to be the result of the distribution of the sensible heat flux.

Individual contributions to the diabatic term are evaluated in the time section format. The vertical contribution of model-diagnosed convective precipitation, large-scale precipitation, eddy transport of sensible heating and long-wave radiation to total diabatic heating are



included in Figs. 34-37. Short-wave radiation time sections are not shown in the figures, but are discussed below.

The convective condensation heating field includes both deep and mid-level convection. After time period 1218, this heating input in the inner volume (Fig. 34a) determines the bulk of the total diabatic temperature tendency present in Fig. 33a. The convective contribution to the outer volume is similar, except that more heating is indicated during the first two time periods. This early increase in heating is due to unrelated convection to the south of the storm center which is included in the larger budget volume.

The model properly attempts to center the maximum of convective heating in the lower troposphere during time period 1318. It establishes this maximum just above sigma level 6 (792 mb) at both storm radii, which is not unreasonable, but may be somewhat low considering the deep convection which develops in the vicinity of the storm center during this period.

The vertical eddy transport term makes its most significant contribution to total diabatic heating in the lowest sigma layer within storm radius 6, as illustrated in Fig. 35. The bulk of the diabatic heating at the inner volume during the first two time periods is determined by this term. This early influence of the sensible heat flux on total diabatic heating within the inner storm volume is not unexpected, since the storm center is embedded in a

strong surface sensible heat flux feature from 12 GMT 12 January 1979 to 00 GMT 13 January 1979.

The cooling feature present in the lowest layer during the last two time periods in Fig. 35a results from a model-diagnosed, downward sensible heat flux in advance of the storm center. As described in the previous chapter, the magnitude of this feature is physically unreasonable. In combination with the long-wave radiational effects, this feature accounts for the inaccurate diagnosis of low-level diabatic cooling at radius 6 during this period (Fig. 33a).

The vertical eddy transport time section for the outer storm volume (Fig. 35b) is very similar to that of the inner volume. The addition of sensible heat to the storm volume is extended in time to 1406, as the larger area covered by this storm radius encompasses more of the sensible heat flux features to the west of the storm center. The effect of the sensible cooling during the last two time periods is greatly reduced within radius 10, as the sensible cooling maximum is primarily confined to the inner budget volume.

Large-scale condensation heating that is diagnosed by NOGAPS (Fig. 36) contributes little to the total diabatic term. The relative insignificance of large-scale heating initially seems unreasonable, when it is considered that this cloud source accounts for the bulk of the extensive cloud mass which is located to the northeast of the storm center throughout most of the evaluation sequence. However, the

magnitude of the vertical motion is small until explosive deepening is established at 1318. By this time, the storm is in relatively cool air where the saturation vapor pressure is low, which restricts the magnitude of the potential condensation heating.

The vertical time section from the inner storm volume (Fig. 36a) indicates that the effect of large-scale heating is confined to the lowest sigma layer until explosive cyclogenesis is established at 1318. Large-scale condensation heating then extends through four sigma layers, which is consistent with the diagnosed deepening of the clouds to the northeast of the storm center during the explosive stage of development. However, the temperature tendencies associated with this term are an order of magnitude less than the convective term, which illustrates why deep convection is so important in cyclogenesis. The outer storm volume (Fig. 36b) provides similar results, although the heating maximum is shifted forward by 12 h to 1406. The upper level contribution is smoothed out as it is averaged over the larger storm area, but the contribution in the lowest layer is increased slightly at the later time periods as the more extensive low-level cloudiness is included in the larger storm volume.

The long-wave radiation time sections (Fig. 37) reflect cloud-top cooling and atmospheric IR cooling. The most significant long-wave cooling occurs in the lowest sigma layer where the most extensive cloudiness is located. This

cooling is strongest during the last two time periods, and provides a weighted contribution of -9 K/day to the low-level cooling feature in the total diabatic temperature tendency time section at radius 6 (Fig. 33a). The strong, low-level, long-wave radiative cooling contribution as determined in the NOGAPS radiation parameterization infers a cloud-top instability mechanism similar to that described by Petterssen, et al. (1962). Vertical time sections of short-wave radiation heating are not shown. Diagnosed heating contributions from short-wave radiation are negligible (weighted maximum of 0.2 K/day) and have little effect on the total diabatic term.

b. Column Averaged Results

The column-averaged, storm volume temperature tendencies are computed for total diabatic heating and the component terms. These results are compared for the inner and outer storm volume in Fig. 38. As noted in the evaluation of the NOGAPS time sections, a remarkable similarity exists in the display of the results for radius 6 and radius 10, which reflects the large storm volume affected by similar diabatic processes.

A nearly linear increase in the total diabatic term is indicated in Fig. 38 until a maximum is reached when explosive deepening is established at 1318. A linear decrease in this warming then follows. This representation of diabatic heating is very reasonable. The maximum diabatic column temperature change rate of 6.96 K/day at radius 6 compares

favorably with results from Yanai, et al. (1973) and Lord (1982) who showed average column temperature changes from diabatic heating in tropical cloud clusters of approximately 5 K/day.

An inspection of Fig. 38 reveals that latent heat release accounts for almost all of the net diagnosed warming. Only a small portion of this latent heat release is attributed to large-scale cloud processes. The vertical eddy transport of sensible heat from the surface makes a significant contribution to diabatic warming (radius 6) during the early time periods, but reverses in sign at time period 1406 when (questionable) sensible cooling is diagnosed to the southeast of the storm center. Much of the column warming by the surface flux during the early period of cyclone development is offset by long-wave radiative effects, which cool the column by 1.5-2.0 K/day. Short-wave radiative warming of the column is less than 0.02 K/day and is not plotted in the figure.

c. Energy Input from NOGAPS Latent Heat Release

The diabatic energy input to the storm volume from NOGAPS-diagnosed latent heat release is computed for the inner and outer storm radii. A comparison of the energy input within the inner and outer storm volumes (Fig. 39) indicates that the level of input remains relatively unchanged between the volumes. Differences at the first time period are attributed to the inclusion of an unrelated cloud mass to the south in the outer storm volume.

The diabatic energy input from latent heat release for radius 6 has a maximum of  $841 \text{ W/m}^2$  at time 1318, with an average input for all time periods of  $352 \text{ W/m}^2$ . These values differ radically with those determined from case studies of continental cyclogenesis by Danard (1966) and Bullock and Johnson (1971), who found the average storm volume energy input from latent heat release to be  $11 \text{ W/m}^2$  and  $8 \text{ W/m}^2$ , respectively. A much more favorable comparison is made with results from Yanai, et al. (1973) for latent heating in tropical cumulus cloud clusters over the Marshall Islands. They determined an average energy input of  $485 \text{ W/m}^2$  from latent heating in the column. This comparison underscores the enhanced role of diabatic heating in maritime cyclogenesis. In relation to latent heating, the energy input from net diabatic heating for radius 6 reaches a maximum of only  $760 \text{ W/m}^2$  at 1318. The average net diabatic energy input to the inner storm volume for all time periods is  $266 \text{ W/m}^2$ .

#### D. NOGAPS AND BUDGET COLUMN WARMING COMPARISON

A comparison of NOGAPS total diabatic warming and the thermodynamic energy budget residual diabatic warming (Fig. 40) indicates that the magnitudes of the maxima are similar ( $8.2 \text{ K/day}$  vs.  $6.96 \text{ K/day}$  at radius 6), but the NOGAPS maximum lags that from the budget diagnosis by 24 h. This comparison is not completely fair since problems are indicated with the budget calculation, and the budget residual

diabatic warming probably did not peak during time period 1218, as shown. In any event, the temperature tendency maxima appear to be of the same magnitude, and the timing of the NOGAPS diabatic heating seems to be more physically representative. A similar comparison holds for the outer storm volume (Fig. 40b). It seems that the NOGAPS diabatic package responds to the large-scale forcing of the FGGE data much better than the thermodynamic energy budget over the open ocean. This difference in the quality of heating estimates is probably connected to the sophisticated BL physics included in the NOGAPS diagnosis, but missing from the budget analysis. The NOGAPS package permits a direct evaluation of the diabatic heating over the ocean while a budget computation can only infer this process indirectly.

## V. CONCLUSIONS AND RECOMMENDATIONS

The contribution of diabatic heating in a case of explosive cyclogenesis in the western North Pacific Ocean during FGGE was investigated in this thesis. An evaluation of the NOGAPS heating package was conducted using the ECMWF analyses for this cyclone during 13-15 January 1979. The storm-related thermal budget was computed with the application of quasi-Lagrangian diagnostics to the analyses. The diabatic temperature tendencies from the NOGAPS diagnostics and the temperature budget were examined and discussed.

### A. RESULTS

#### 1. NOGAPS Boundary Layer and Cloud Parameterization

The model boundary layer parameterization yields correct positioning of the sensible heat flux features relative to computed air-sea temperature differences and the boundary layer (ECMWF 1000 mb) wind fields. Generally, positive flux features are confined to the cold air behind the front and negative fluxes are located in the warm sector to the east of the front. The large negative flux maxima generated by the model at later time periods are a reflection of the ECMWF wind and temperature analyses and not the NOGAPS model performance. The magnitudes of the diagnosed positive sensible heat flux maxima are high, but not excessive compared to previous studies given the intense nature of this cyclone.



The top of the model planetary boundary layer is collapsed to extremely low heights in regions where sensible heat flux maxima are diagnosed. Modification of the drag coefficients in these regions may lead to an artificial increase in the sensible heat flux values in the model.

The combined cloudiness diagnosed in the model is representative of the verifying satellite imagery. Outbreaks of convection observed in the vicinity of the storm center, as well as observed deep frontal convection, are handled well by the model parameterization. A tendency to displace these features slightly to the west of their verifying positions is noted at several of the evaluation times. Cloud streets and open-cell cumulus clouds in the cold air streams are treated as unstable stratus in the parameterization. This model-generated, large-scale cloud feature is diagnosed over regions of strong sensible heat flux. The boundary layer is collapsed at gridpoints where these clouds are diagnosed in the boundary layer. The model depiction of the large-scale cloudiness properly accounts for the large cloud mass to the northeast of the storm center, as well as a portion of the frontal clouds, throughout most of the storm sequence.

Model-diagnosed temperature tendencies associated with large-scale condensation heating are reasonable. Temperature tendencies associated with convective condensation heating appear to be excessive, but are related to the very large convective precipitation rates determined by the model for this system. These precipitation rates are not totally inconsistent with the observed intensity of the cyclone.

## 2. NOGAPS and Thermodynamic Energy Budget Diabatic Heating

The maximum of NOGAPS-diagnosed diabatic heating precedes the peak in storm intensity by approximately 24 h. This temporal distribution of the heating is a reasonable reflection of the explosive development of the cyclone and the time lag required between atmospheric forcing and atmospheric response.

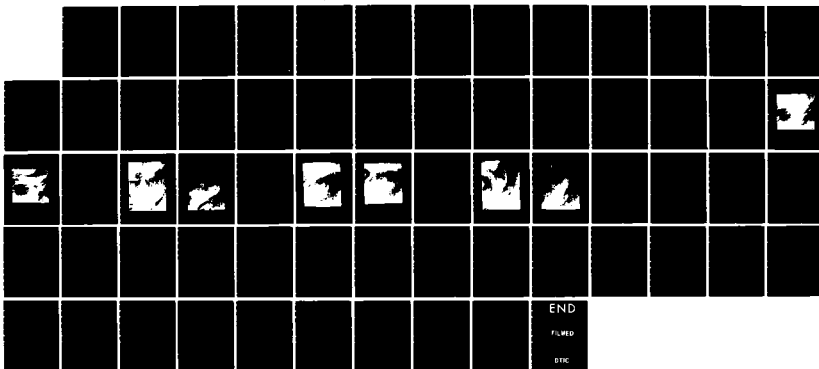
NOGAPS-diagnosed total diabatic heating is primarily composed of latent heat release in the column. The great bulk of the latent heating is convective in nature, with large-scale processes accounting for only a small percentage of the heating. All other NOGAPS heating terms are small in comparison to the latent heat release.

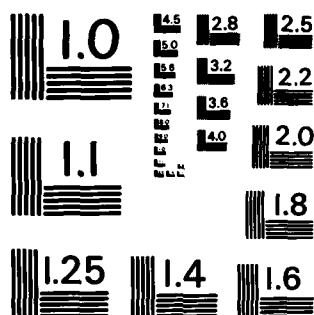
The NOGAPS average diabatic energy input to the storm volume through latent heat release is an order of magnitude larger than estimates based on continental cyclogenesis. The results are in general agreement with a previous study of latent heating in maritime, tropical cumulus cloud clusters. The large, diagnosed contribution of latent heat release to the energy of the system in this case of maritime cyclogenesis underscores the increased importance of the diabatic processes in cyclogenesis over the oceans.

A significant amount of diabatic heating is determined from thermodynamic energy budget calculations during the first two time periods (1206-1218), as the cyclone experiences initial growth. The magnitude of the budget diabatic residual

242

NL





MICROCOPY RESOLUTION TEST CHART  
NATIONAL BUREAU OF STANDARDS-1963-A

decreases unrealistically as the storm moves away from land after the third time period (1306). This calculated deterioration of the diabatic process coincides with the explosive development of the system, when the contribution from the diabatic term is expected to be greatest. The magnitude of diabatic heating increases significantly during the last time period (1406) when the system reaches peak intensity and the storm center is again near land where the quality of the data is much better.

Errors occur in the thermodynamic energy budget where the storm tracks over the open ocean. The temperature time tendency and advective terms of the thermodynamic energy equation do not appear to be properly represented using the 12-h, large-scale FGGE forcing as the storm center moves away from land.

Adiabatic temperature advection produces net cooling in the column at all times. The magnitude of the diabatic warming is larger than this cooling during the early stages of cyclone development when the diabatic calculation appears to be relatively unaffected by budget error.

Differences in the magnitude of the maximum diabatic column temperature change as determined by NOGAPS and the thermodynamic energy budget are less than 15%, with the thermodynamic energy budget producing the greater maximum. The apparent 24-h lag between the maxima appears to be artificially induced by discrepancies in the ECMWF analyses and

the smoothing effect of the 12-h time averaging of the advective terms in the budget formulation.

Maximum diabatic forcing in NOGAPS precedes the maximum advective cooling calculated in the thermal budget by 12 h. The comparison indicates that the NOGAPS-diagnosed diabatic heating is of the same magnitude as, and maintains the proper temporal distribution with, the calculated advective cooling. The similarity of results from the inner and outer storm volumes indicate that the diabatic effects are spread evenly over a relatively large region around the storm center.

The results of this study indicate that the large-scale forcing by the FGGE data is sufficient to produce reasonable heating estimates from the NOGAPS diabatic package, but is not sufficient to adequately resolve the diabatic heating through application of a thermodynamic energy budget calculation over the open ocean.

#### B. RECOMMENDATIONS FOR FUTURE RESEARCH

Further investigation of NOGAPS boundary layer behavior in regions of strong sensible heating is required to evaluate the effect of the collapsing boundary layer and resulting modification of the drag coefficients on the diagnosis of the surface sensible heat flux.

The thermodynamic energy budget calculation and NOGAPS diagnostics should be applied together in other cyclone evaluations to verify the apparent superiority of the NOGAPS

diabatic heating estimates over open ocean regions which was observed in this study. The flux form of the thermodynamic energy equation should be applied in the budget to see if any improvement in the calculations result.

The thermodynamic energy budget calculation and NOGAPS diagnostics should be performed using temperatures derived from the ECMWF height fields to determine if the initialized temperatures were a large source of error in the calculations. A storm-area moisture budget should be determined as the next phase in the evaluation of this storm system.

#### C. FINAL CONCLUSION

Diabatic heating produces significant storm-area column temperature changes in explosive maritime cyclogenesis, which enhances system intensification. Proper model parameterization of these processes are essential if accurate numerical weather forecasts are to be realized over the oceans.

APPENDIX A  
SYNOPTIC SYMMARY

A complete synoptic discussion of the western Pacific Ocean storm system evaluated in this thesis is given by Calland (1983). The significant events of cyclone development are summarized by time period to present an overview of cyclogenesis as it occurred during 12-15 January 1979.

The large-scale flow pattern at 00 GMT 12 January 1979 transports cold, continental air southward into the vicinity of a warm, southerly flow from the tropics. A region of strong, low-level baroclinity develops to the east of Japan. A quasi-stationary, long-wave trough is located over the region in the mid-troposphere. This trough supports a steady flow of cold air off the Siberian coast. The mid-level flow over the area of the incipient system is primarily zonal. A broad jet is present in the upper troposphere, and reflects the baroclinity in the low levels. A jet streak ( $> 15$  m/s) remains well upstream of the region of the developing disturbance.

A. 00 GMT 12 JANUARY 1979-00 GMT 13 JANUARY 1979

The incipient storm has a closed center of 995 mb. A weak thermal ridge is established near the surface center and indicates continued frontogenesis. The combination of



flow from a strengthening Siberian High to the north and a nearly stationary cold low to the east pumps cold air southward over the warmer sea surface, which continues the destabilization of the surface layer. A polar low has formed to the west of the incipient system over the southeast tip of Japan.

In the mid-troposphere, a short wave which incorporates a broad area of positive absolute vorticity has formed about 800 n mi upstream of the incipient system. A small region of positive vorticity has formed over the storm center. The jet core in the upper level is superposed over the surface low center and the jet streak continues to approach from the west.

B. 00 GMT 13 JANUARY 1979-00 GMT 14 JANUARY 1979

The storm enters the explosive stage during this period, as the central pressure falls to 977 mb. The surface low accelerates to the northeast into the vicinity of the maximum sea-surface temperature gradient. A diffluent trough begins to form in the mid-troposphere. Mid-level vorticity increases as the jet streak propagates into the region from the west and enters the diffluent trough.

The storm system experiences increased vertical development following the jet streak interaction. The arrival of the jet streak at 250 mb (max > 85 m/s) over the surface system enhances low-level circulation. The diffluence and cyclonic shear that are associated with this streak increase

both vertical motion through the mid-troposphere, and storm circulation in general. The short-wave that was present over Japan during the previous period is now absent, indicating that further explosive development is not sustained by short-wave, positive vorticity advection aloft.

C. 00-12 GMT 14 JANUARY 1979

The central pressure falls to 965 mb during this 12-h period. The amplitude of the surface thermal ridge increases, indicating enhanced circulation in the lower troposphere. Self-amplification continues at 500 mb. The apparent lack of significant vorticity advection indicates that the continued intensification of the cyclone system is not forced in the mid-troposphere. Cyclonic shear and curvature to the left of the jet axis increases cyclonic vorticity at 250 mb and enhances low-level storm circulation. Vertical velocities increase and cyclone development extends to higher levels in the troposphere.

D. 12 GMT 14 JANUARY 1979-00 GMT 15 JANUARY 1979

The first half of this period marks the most explosive stage of cyclone development. The surface pressure falls an additional 18 mb and the cold air begins to wrap around the vortex, which signals the onset of occlusion. The mid-level trough continues to amplify, but its vorticity center elongates. This change in the vorticity pattern foreshadows weakening of the system. The jet stream is still in a

favorable position over the surface low to promote continued intensification, but the rapid movement of the cyclone to the northeast will reduce this jet influence.

E. 00 GMT 15 JANUARY 1979

The surface low is located over the Aleutian Islands at this time. The central pressure reaches 947 mb as the system begins to occlude. A closed circulation has formed at 500 mb and negative vorticity advection into the region induces subsidence and filling. The jet has decreased in intensity with the weakened low-level baroclinity, and the cyclone center is located to the north of the jet axis.

## APPENDIX B

### FGGE DATA

The data base used in this study is the First GARP Global Experiment (FGGE) Level III-b objectively analyzed meteorological fields. These analyses were produced by the European Center for Medium-range Weather Forecasting (ECMWF) from the first Special Observing Period (SOP-1) for the region covering the track of the western Pacific cyclone of interest. This data set is the product of an intensive one year worldwide data collection effort which utilized conventional surface, aircraft, rawinsonde, pilot balloon, drifting buoy and satellite observations to produce global meteorological fields for research purposes. The data collection for this project was carried out under the auspices of the Global Atmospheric Research Program (GARP) for the year 1979. SOP-1 covered the first two months of the project (5 January--5 March 1979) and is significant in that more observation platforms were brought to bear during this period with the resulting analyzed fields archived in 6 vice 12-h intervals.

In FGGE level III-b, the processed temperature, moisture, wind velocity and height data have been transformed into dynamically-derived meteorological fields through a four-dimensional data assimilation technique described by Bengtsson et al. (1982). These fields were produced in 15 vertical levels with a horizontal resolution of  $1.875^\circ$  in

latitude and longitude. The data was error checked at the ECMWF by comparison of first guess fields and nearby observations level by level. As reported by Bengtsson et al. (1982), the SOP-1 data was generally found to be of excellent quality. The fields available in the FGGE data are compiled by level in Table III.

Validation of the ECMWF analyses has been performed in several studies including that of Calland (1983) in his assessment of the analyses used in this thesis. Through a comparison of the ECMWF level III-b, NMC and FNOC analyses during the period of storm development, Calland found the ECMWF analyses to be very good overall. He did note, however, that the 0600 and 1800 GMT analyses contained spurious potential temperature biases which adversely affected his budget computations.

FGGE vertical velocity and temperature fields were taken from the initialization stage of the data assimilation at the ECMWF, rather than from the analysis stage. The magnitudes of the resulting FGGE vertical velocities were small compared to those determined kinematically. Kinematic vertical velocities are substituted for the FGGE values in the data set utilized in this evaluation. The FGGE temperatures are verified against the height (mass) field to ensure consistency.

## APPENDIX C

### THE NAVY OPERATIONAL GLOBAL ATMOSPHERIC PREDICTION SYSTEM (from Ranelli, 1984)

The Navy Operational Global Atmospheric Prediction System (NOGAPS) used at the Fleet Numerical Oceanography Center (FNOC) is a slightly modified version of the UCLA general circulation model. NOGAPS has been the Navy's operational atmospheric forecast model since August 1982. The following sections describe the various features of NOGAPS as used during the experiment. The complete model has been described by Rosmond (1981).

#### A. DYNAMICS

The dynamics of the UCLA GCM are described in detail by Arakawa and Lamb (1977) and are only discussed briefly here. NOGAPS is a primitive equation model. The prognostic variables are horizontal velocity,  $V$ , temperature,  $T$ , surface pressure,  $p_s$ , and specific humidity,  $q$ . Additional prognostic variables associated with the planetary boundary layer (PBL) will be described below. The finite difference scheme used has a spatial resolution of  $2.4^\circ$  lat by  $3.0^\circ$  long. The variables are staggered in the horizontal according to Arakawa scheme C. The center grid point contains the  $T$  value. The meridional wind component,  $v$ , is carried at points north and south of the center point and the zonal wind component,  $u$ , is

carried at points east and west of the center point. The numerical differencing scheme is both energy and enstrophy conserving.

NOGAPS uses a sigma coordinate system in the vertical defined as:

$$\sigma = (p - p_i) / \pi$$

where:

$$p_i = 50 \text{ mb} \quad \text{and} \quad \pi = p_s - p_i,$$

$p$  is pressure and  $p_s$  is surface pressure. There are six model layers in the vertical with the top of the model atmosphere at 50 mb. All prognostic variables except vertical velocity,  $\dot{\sigma}$ , are carried at the middle of each layer. Vertical velocity is carried at the layer interfaces.

NOGAPS uses a second order (leapfrog) time difference scheme with a four minute time step. Model diabetics are executed every forty minutes. A Matsuno time step is used every fifth time step. This is used to control the computational mode and to assist in the assimilation of the diabatic effects. In regions above 60° latitude, a special Fourier filter is used to avoid an extremely short time step. Whereas a simple three point filter is used equatorward of 60 deg. This filtering reduces the amplitudes of the zonal mass flux and pressure gradients and maintains computational stability.

## B. MODEL DIABATICS

The sophisticated model diabatrics contained in NOGAPS is an important component in this experiment. This treatment of the diabatic processes is necessary to adequately simulate fluxes across the air-sea interface and to propagate the full effect of these changes throughout the atmosphere. NOGAPS directly computes the physical processes for:

- dry convective adjustment
- large-scale precipitation
- diagnosis of stratus cloud depth
- mid-level convection
- ground hydrology
- surface friction
- horizontal diffusion of momentum
- radiative transfer processes
- cumulus convection

### 1. Planetary Boundary Layer

The planetary boundary layer (PBL) is defined as a well mixed layer in moisture, moist static energy and momentum. It is assumed to be capped by discontinuities in temperature, moisture and momentum. The PBL treatment in this model follows Deardorff (1972) and has been formulated for the UCLA GCM by Randall (1976). It allows for interaction between the PBL and cumulus cloud ensembles and/or a stratus cloud layer at each grid point. Surface fluxes are determined using a bulk Richardson number based on the values of the sea surface temperature and the values of  $V$ ,  $T$  and  $q$  from the adiabatic portion of the model. These values are then used



to predict a new PBL depth and the strength of the inversion jumps.

The NOGAPS PBL is constrained to remain in the bottom sigma level of the model. This differs from the original formulation of the UCLA GCM, in which the PBL was allowed to pass out of this layer. An overly deep PBL can result in serious computational problems with the model. Constraining the PBL this way imposes a maximum depth of about 200 mb on the PBL.

## 2. Cumulus Parameterization

Cumulus parameterization in NOGAPS follows the scheme of Arakawa-Schubert (1974) as introduced into the model by Lord (1978). In the model, cumulus clouds must have their bases at the top of the PBL. Cloud tops can be at all sigma levels above the PBL. Cumulus clouds are modeled as entraining plumes in which environmental air is mixed with the PBL air from which the cloud originated. Tendencies of moisture, temperature and momentum are diagnosed as well as the cloud mass flux. The cloud base mass flux removes mass from the PBL, which decreases the PBL depth. Condensation occurs at each grid point where the air becomes supersaturated. A moist convective adjustment procedure removes convective instability between mid-tropospheric layers that is not eliminated by clouds originating from the PBL.

## 3. Radiation

The radiation parameterization follows Katayama (1972) and Schlesinger (1976). It includes both a diurnal

variation and interaction with the cloud distribution. Radiative transfer processes for incoming solar radiation are computed. Effects of water vapor, Rayleigh scattering by air molecules and absorption and scattering by water droplets in clouds are included. Reflection due to clouds is also calculated. The model cloud cover predicted by the PBL, the cumulus parameterization and large-scale precipitation interact with the long wave radiation. The net surface heat flux is computed as a function of the incoming solar heat flux, long-wave radiation and sensible heat flux. In the present model, this affects only the surface temperature over bare land and ice and has no effect on sea-surface temperature.

# APPENDIX D

## TABLES

TABLE I  
SENSIBLE HEAT FLUX COMPARISON

INVESTIGATOR	MAX FLUX W/m <sup>2</sup>	EVALUATION TIME	MAX FLUX W/m <sup>2</sup>
Petterssen (1962)	699	13/0000	1400
Pyke (1964)	105	13/1200	900
Manabe (1958)	498	14/0000	1100
Gall & Johnson (1970)	1080	14/1200	500
Bosart (1984)	800	15/0000	300

TABLE II

SIGMA AND PRESSURE LAYER RANGES AND WEIGHTING  
TIME PERIOD 12 GMT 13 JANUARY 1979

<u>SIGMA LAYER</u>	<u>PRESSURE LIMITS (MB)</u>	<u>WEIGHTING FACTOR</u>
6	994-696	3.0
5	696-497	2.0
4	497-298	2.0
3	298-149	1.5
2	149-75	0.74
1	75-50	0.24

<u>PRESSURE LAYER</u>	<u>LIMITS (MB)</u>	<u>WEIGHTING FACTOR</u>
1	994-850	1.5
2	850-700	1.5
3	700-500	2.0
4	500-400	1.0
5	400-300	1.0
6	300-250	0.5
7	250-200	0.5
8	200-150	0.5
9	150-100	0.5

TABLE III  
 AVAILABILITY OF FGGE DATA  
 (From Bengsston, 1982)

	Z	U	V	T	W	RH
10 mb	x	x	x	x	x	
20 mb	x	x	x	x	x	
30 mb	x	x	x	x	x	
50 mb	x	x	x	x	x	
70 mb	x	x	x	x	x	
100 mb	x	x	x	x	x	
150 mb	x	x	x	x	x	
200 mb	x	x	x	x	x	
250 mb	x	x	x	x	x	
300 mb	x	x	x	x	x	x
400 mb	x	x	x	x	x	x
500 mb	x	x	x	x	x	x
700 mb	x	x	x	x	x	x
850 mb	x	x	x	x	x	x
1000 mb	x	x	x	x	x	x

# APPENDIX E

## FIGURES

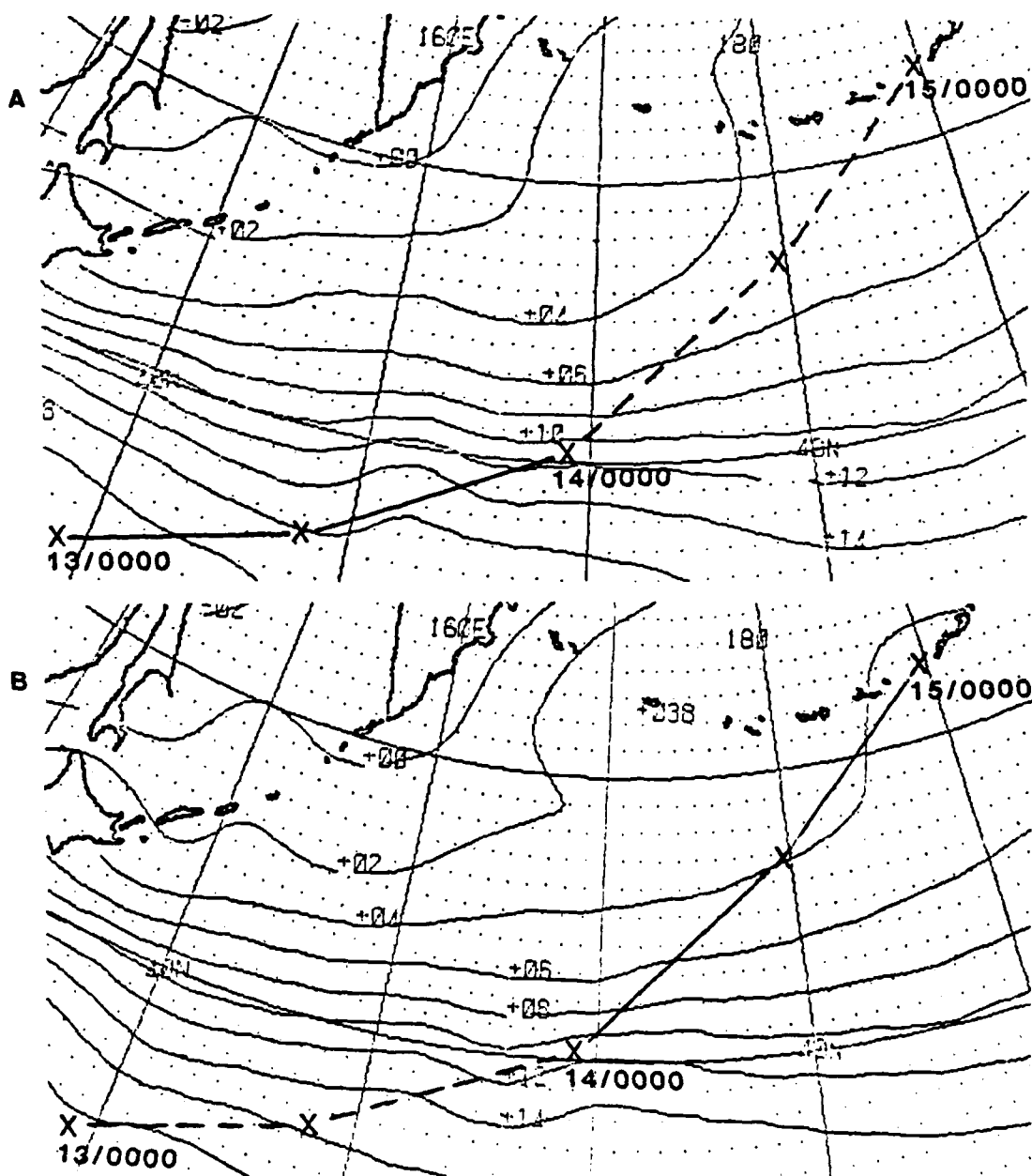


Figure 1. Storm Track and FNOC Sea-surface Temperature Analysis for (A) 00 GMT 12 January 1979, (B) 12 GMT 16 January 1979. Contour Interval is 2°C. Dashed Portion of the Track not Covered by the Analysis. Label X Identifies 12 h Storm Center Positions.

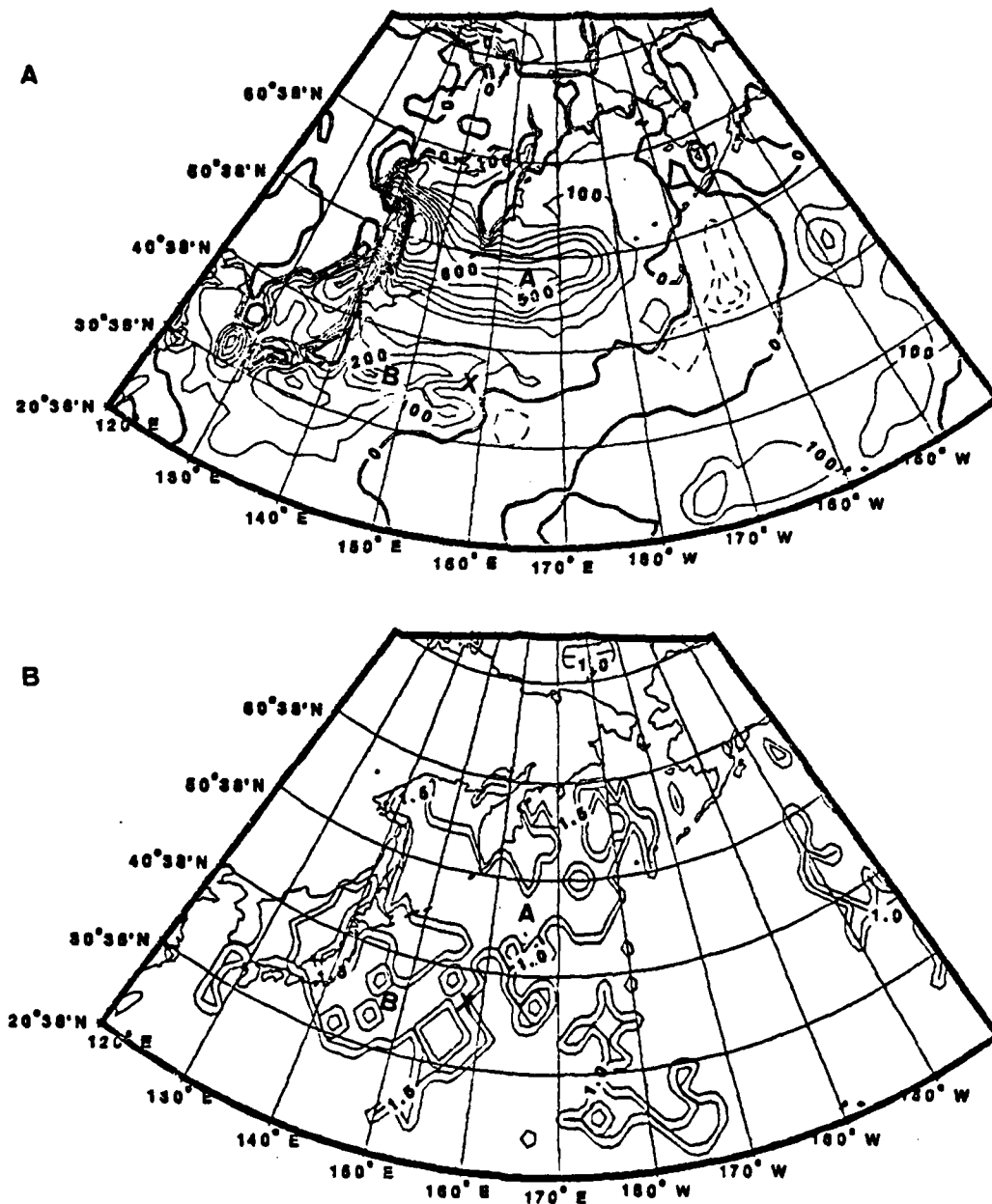


Figure 2. NOGAPS BL Diagnoses 12 GMT 13 January 1979 of (A) Sensible Heat Flux and (B) LCI. Flux Contour Interval is 100 W/m<sup>2</sup>. Dashed (Negative) Values Indicate Flux into the Ocean. LCI Greater than 1.0 Indicates Unstable Stratus. Label X Identifies the Storm Center.

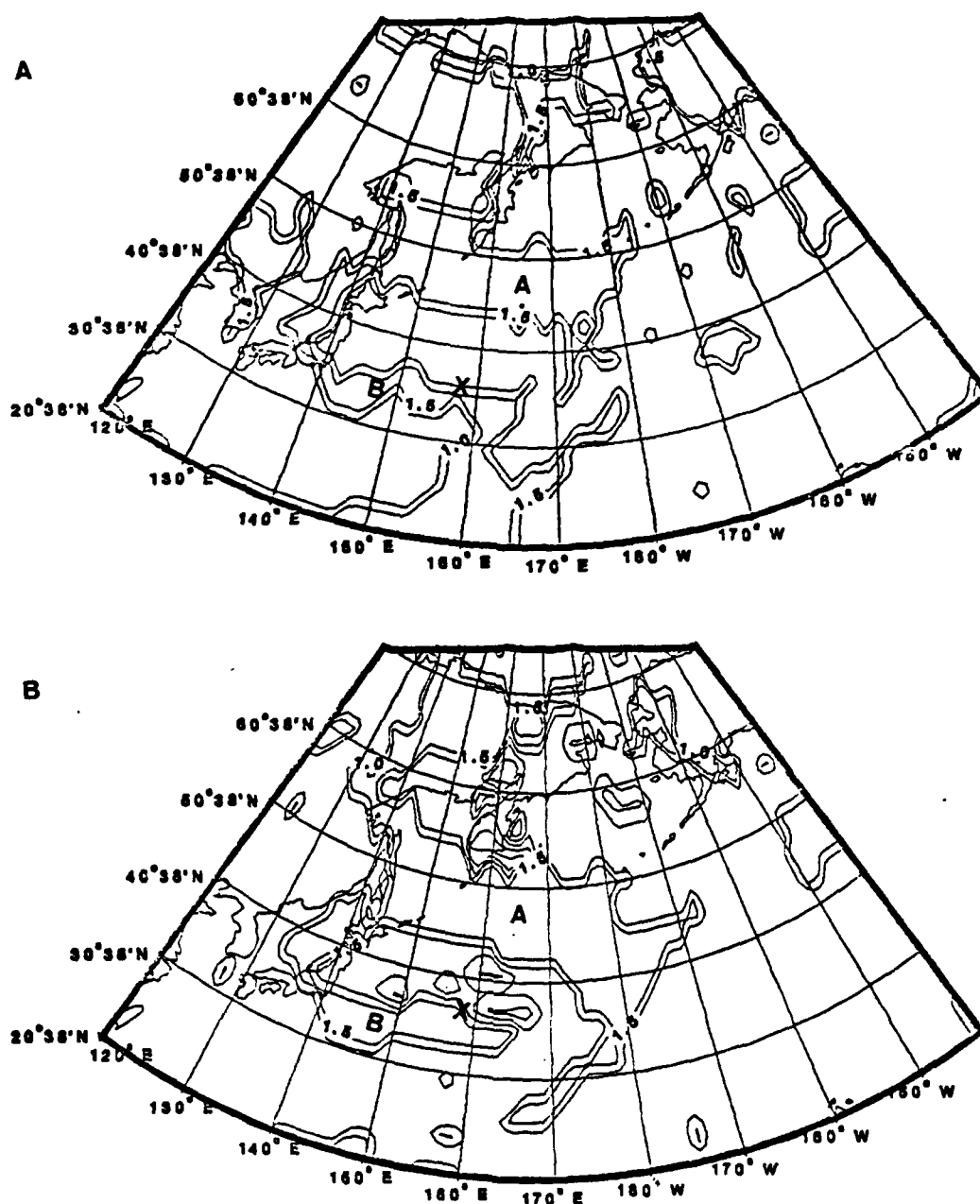


Figure 3. NOGAPS BL Diagnoses 12 GMT 13 January 1979 of (A) BL Thickness < 20 mb and (B) Sigma Level 6 Large-scale Precipitation. Contours > 1.0 Indicate Location of Respective Fields. Label X Identifies the Storm Center.



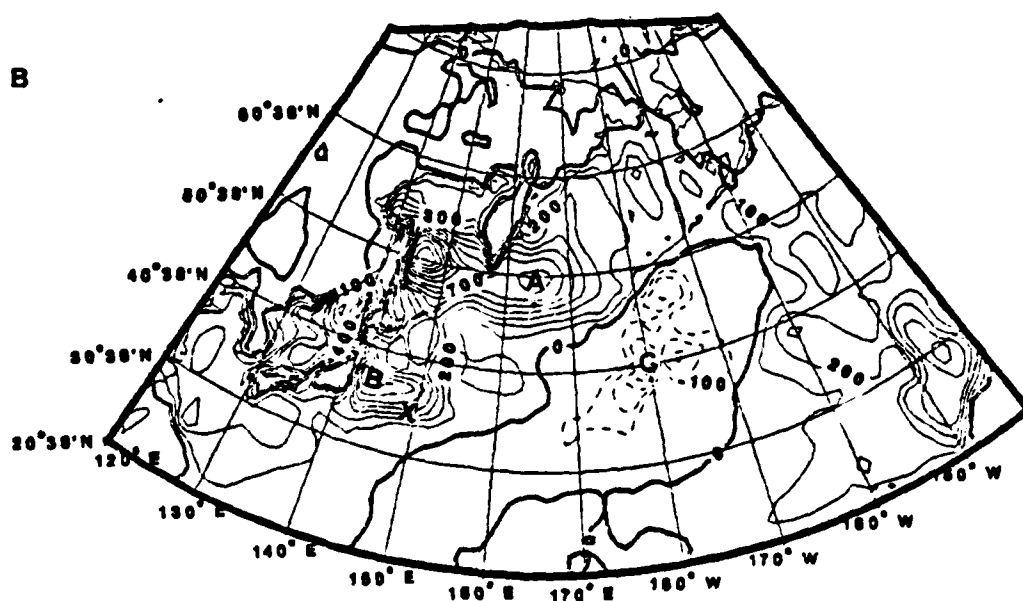
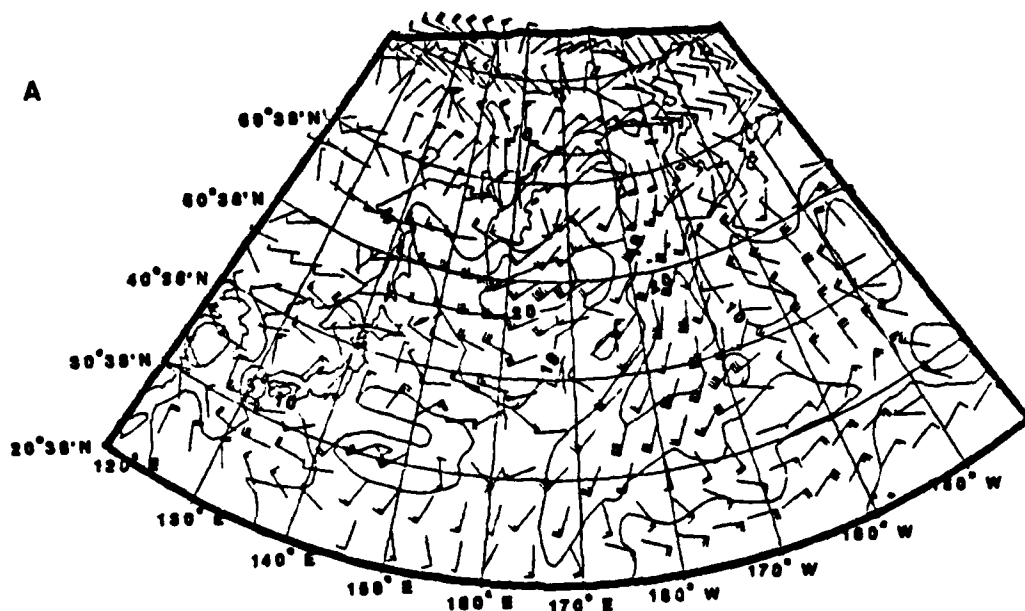


Figure 4. BL Wind and Flux Fields for 00 GMT 13 January 1979 of (A) FGGE 1000 mb Wind Field and (B) Sensible Heat Flux Field. Isotach Contour Interval is 10 m/s. Wind Barbs Indicate Knots. Flux Unit and Contour Interval as in Figure 2. Label X Identifies the Storm Center.

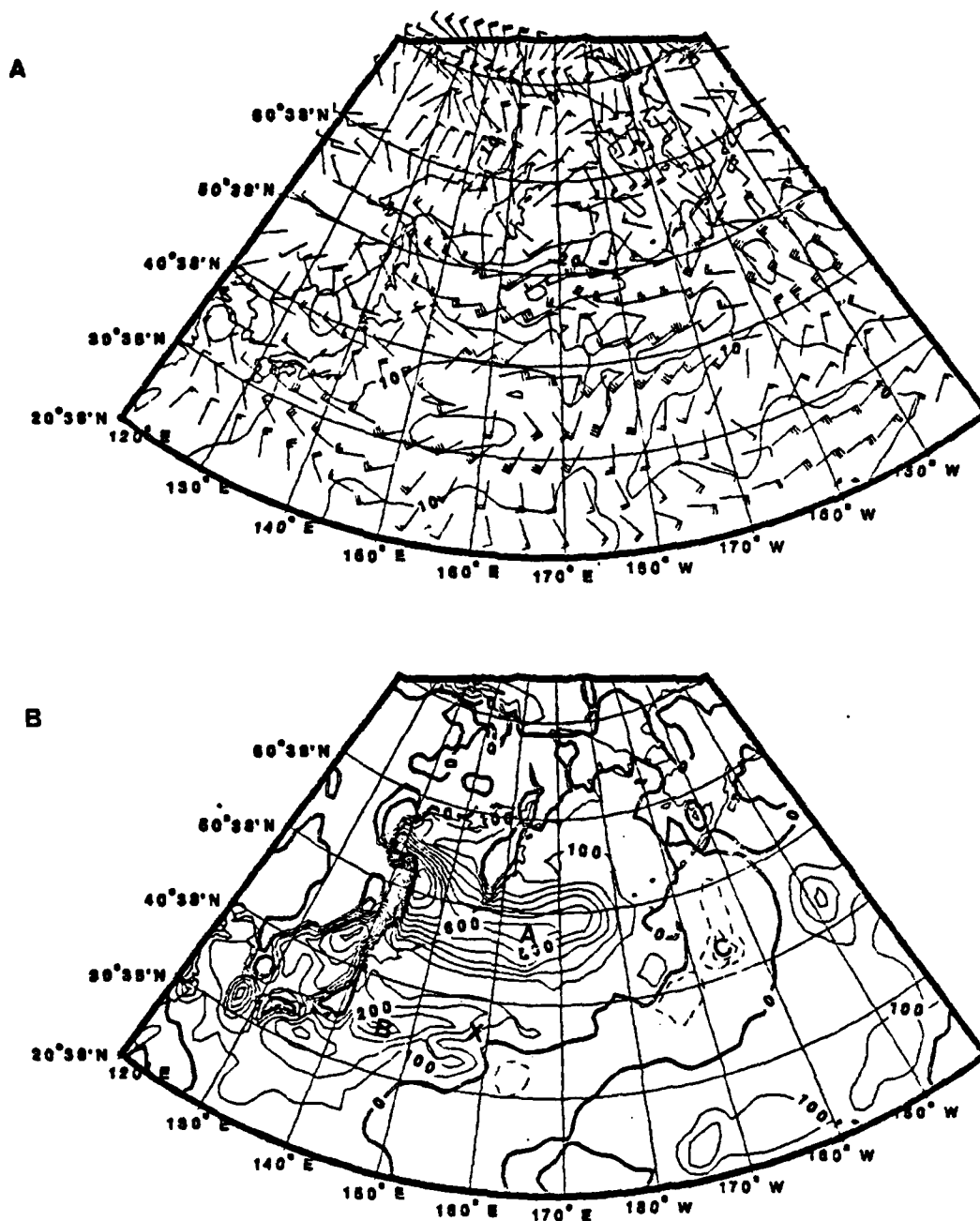


Figure 5. Similar to Figure 4 Except for 12 GMT 13 January 1979.

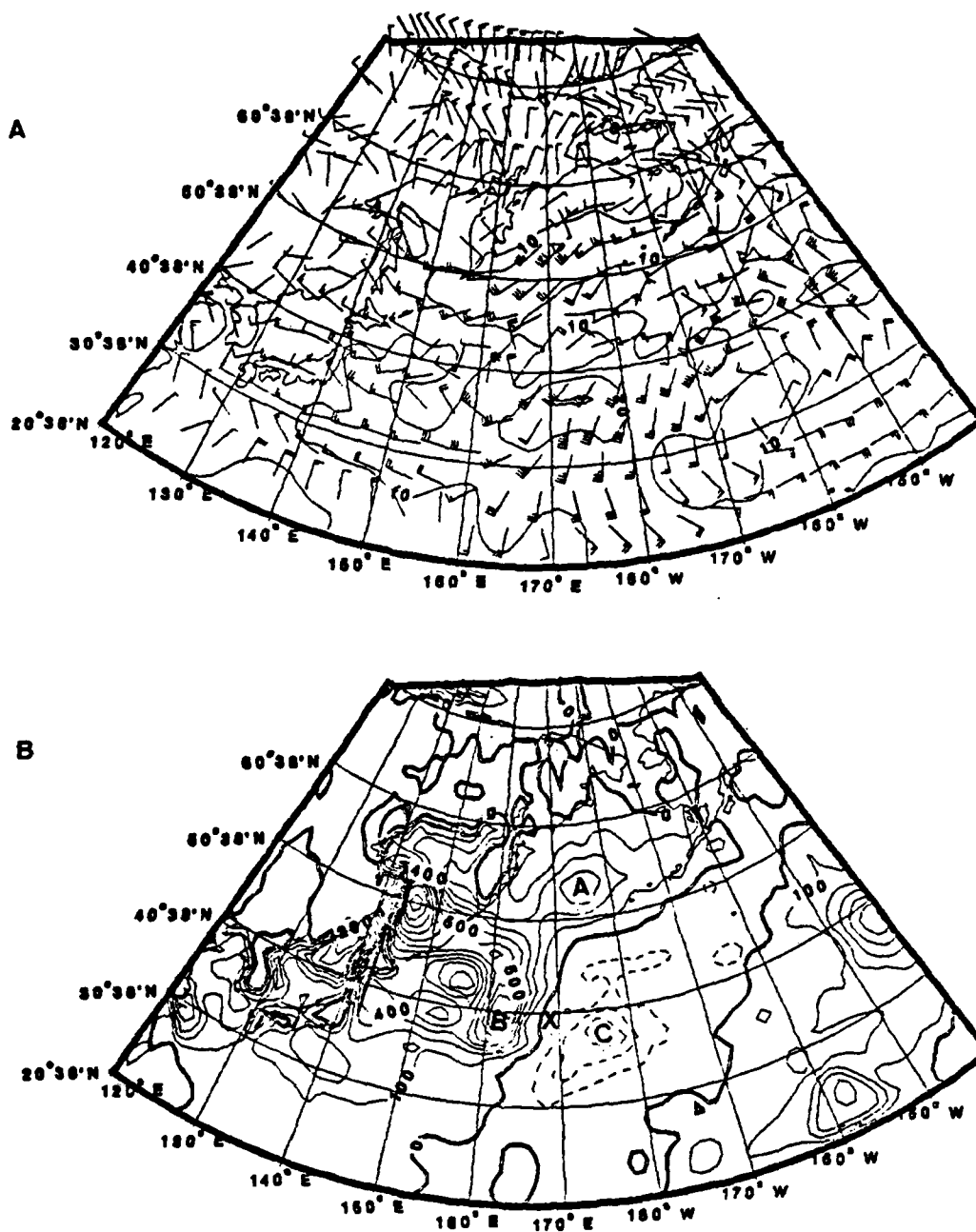


Figure 6. Similar to Figure 4 Except for 00 GMT 14 January 1979.

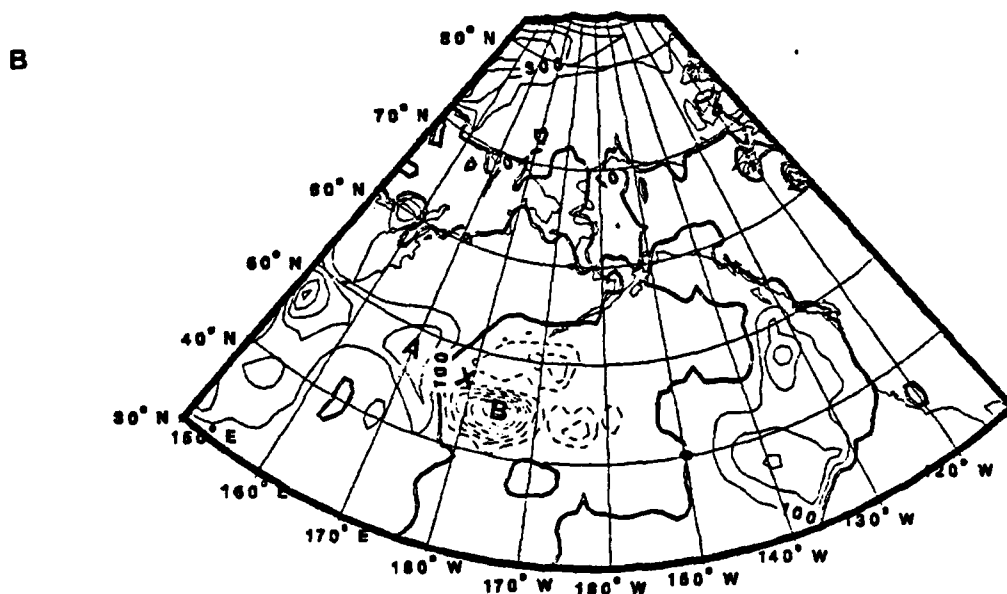
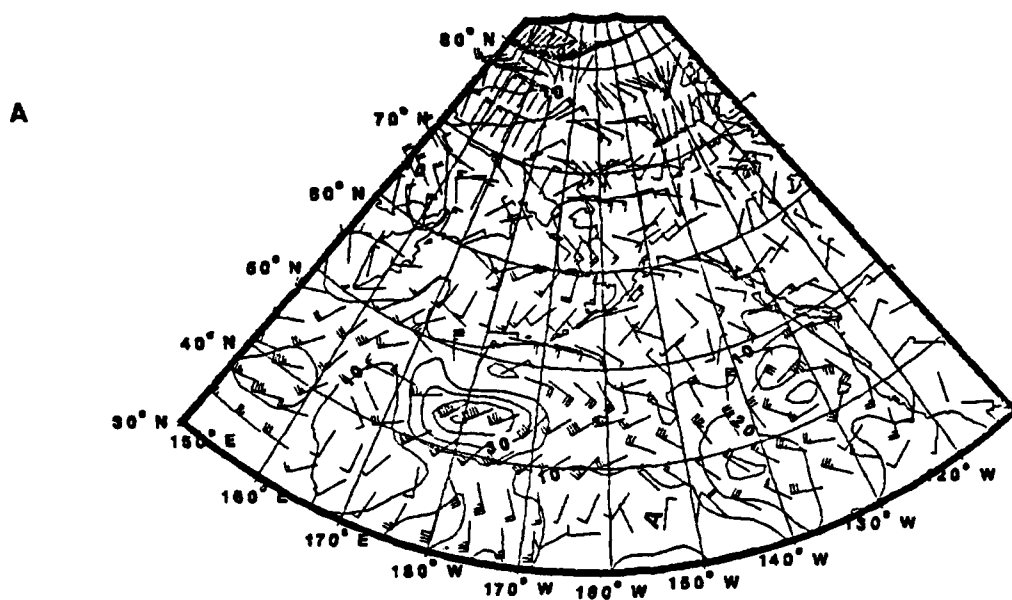


Figure 7. Similar to Figure 4 Except for 12 GMT 14 January 1979 and Southwest Corner of Grid Shifted to 30°N, 150°E.

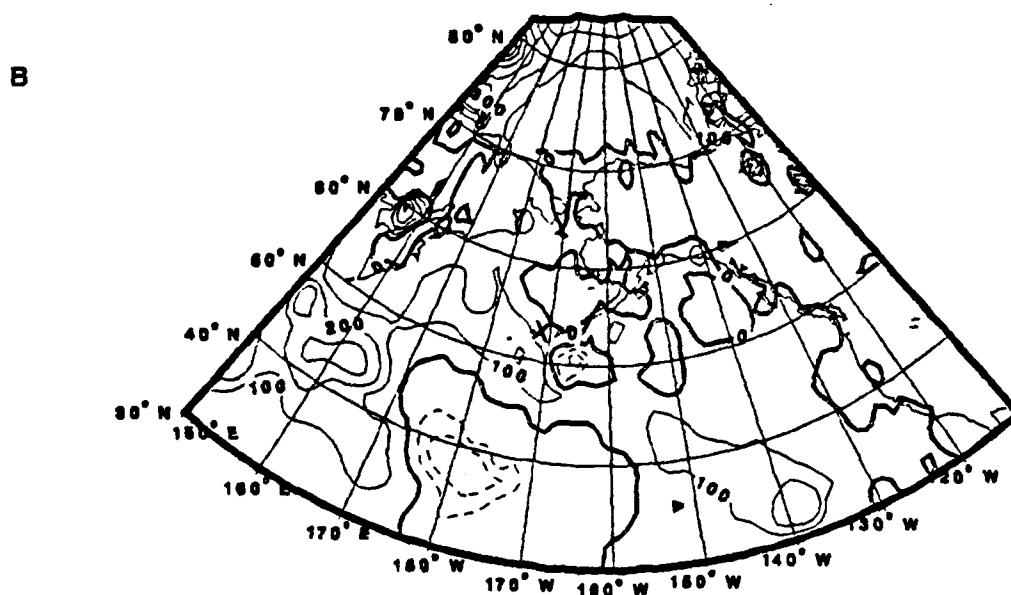
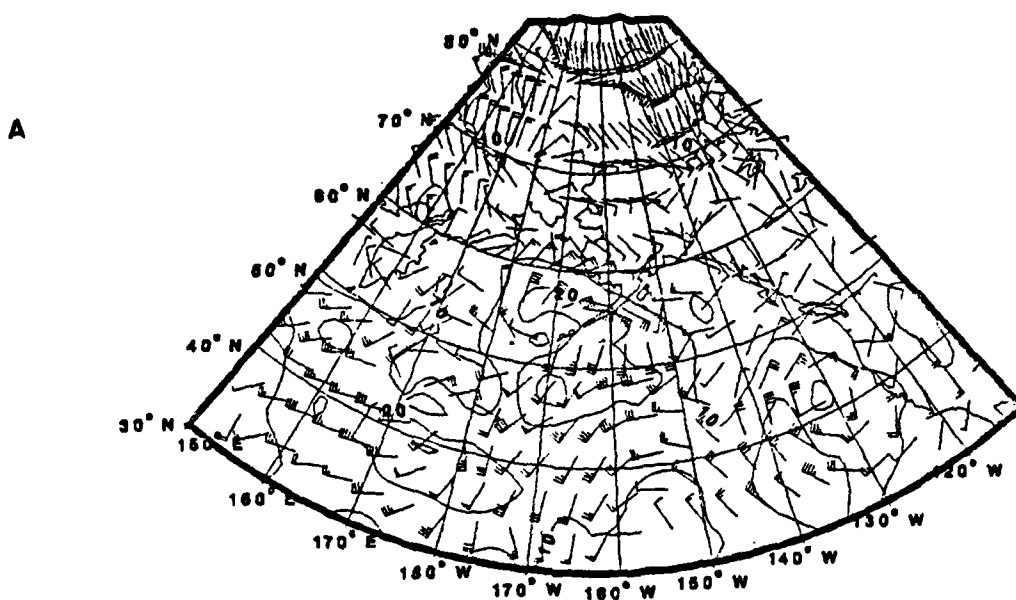


Figure 8. Similar to Figure 4 Except for 00 GMT 15 January 1979 and Southwest Corner of Grid Shifted to 30°N, 150°E.

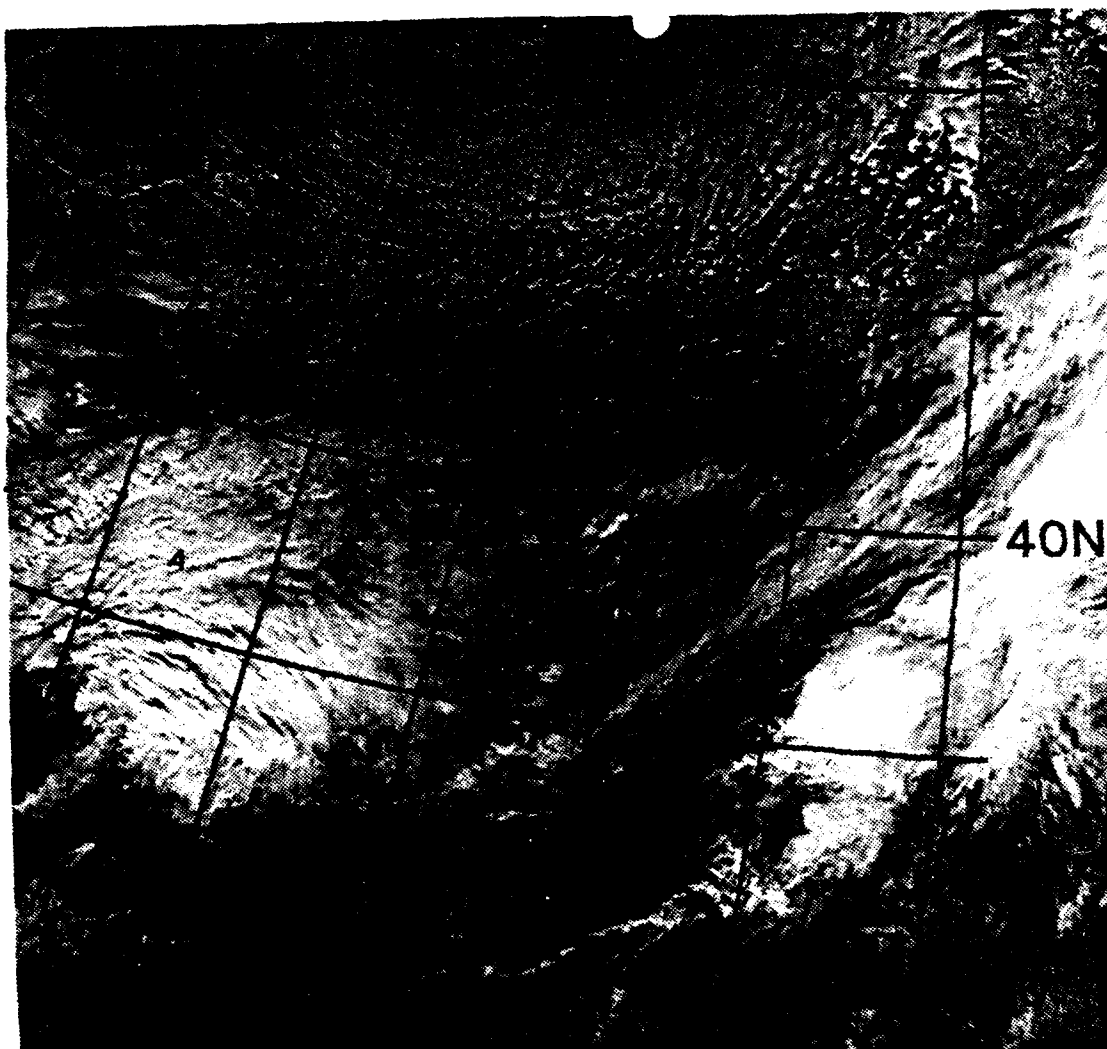


Figure 9. DMSP Visual Satellite Imagery for 2341 GMT 12 January 1979. Label A Indicates Incipient System.

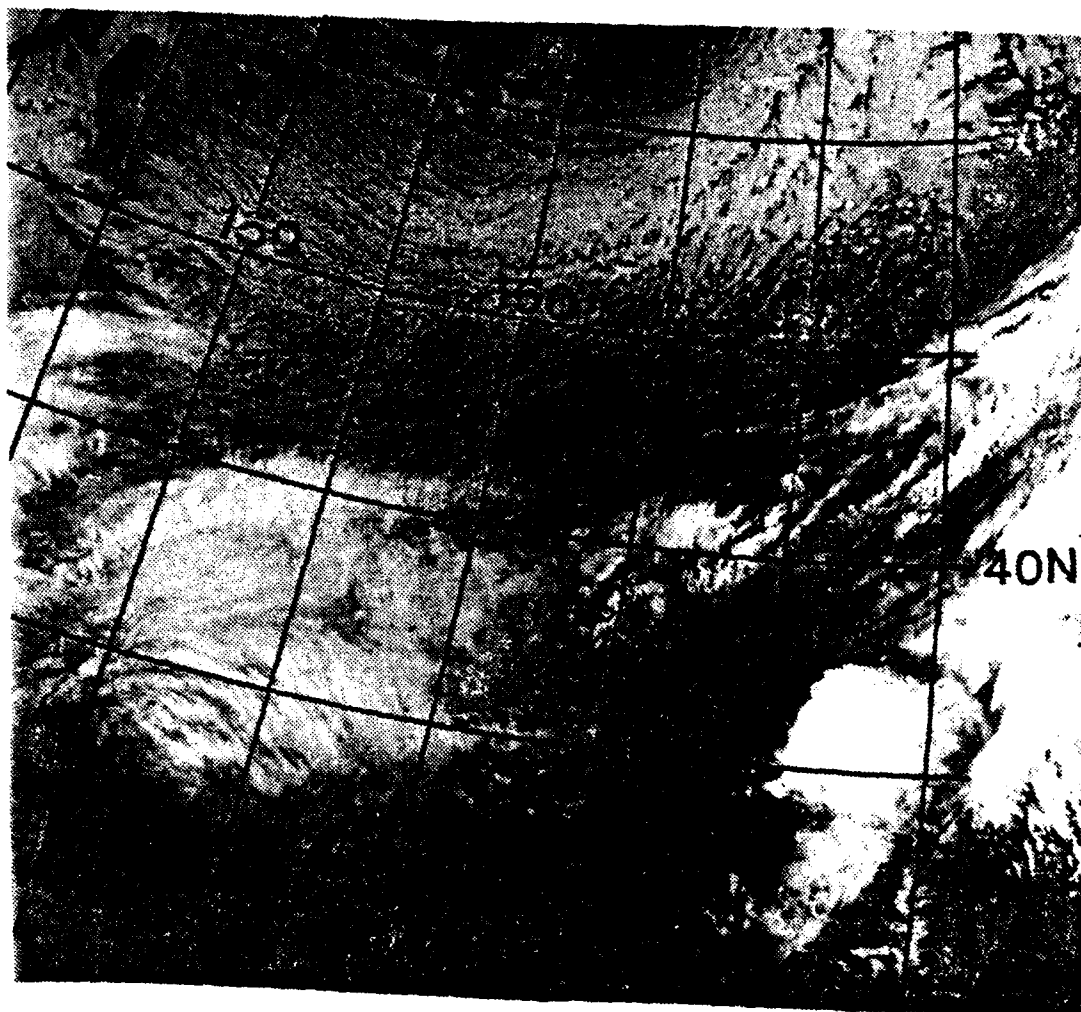


Figure 10. DMSP Infrared Satellite Imagery for 2341 GMT 12 January 1979. Label A Indicates Incipient System.

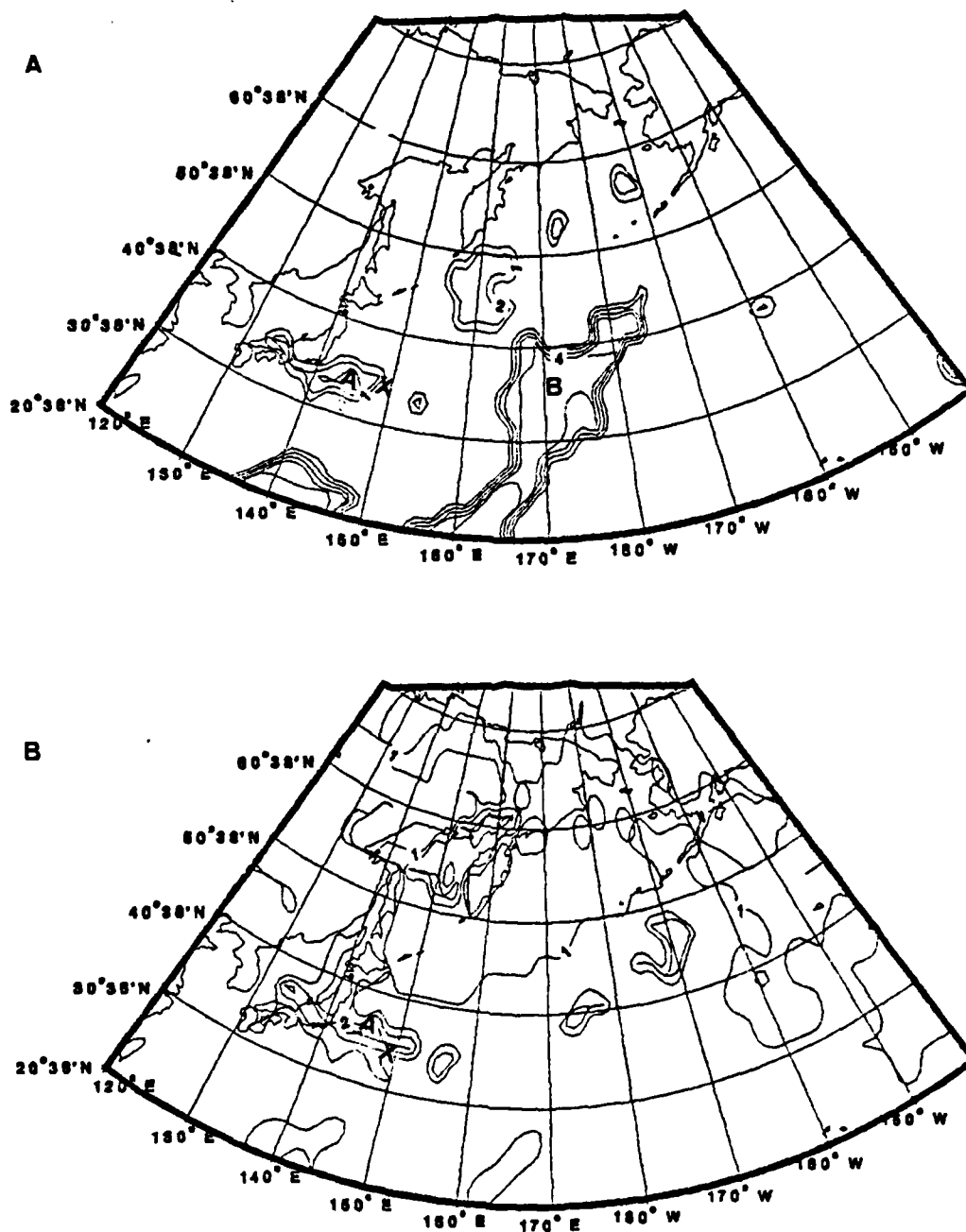


Figure 11. NOGAPS Cloud Diagnoses of (A) Convective and (B) Large-scale for 00 GMT 13 January 1979. Contours Indicate Number of Sigma Levels Where Condensation Heating is Diagnosed.



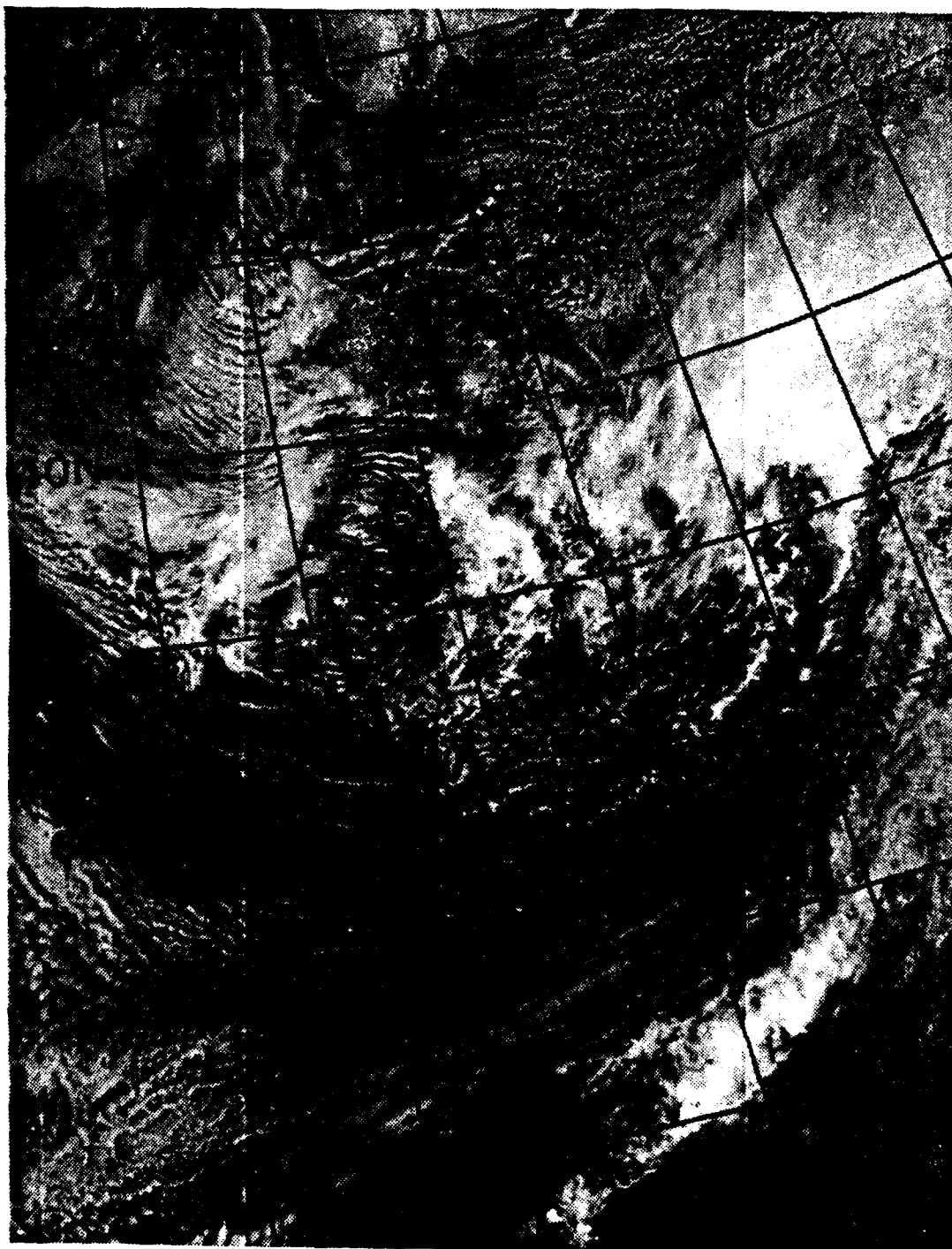


Figure 12. Similar to Figure 9 Except for 1405 GMT 13 January 1979.

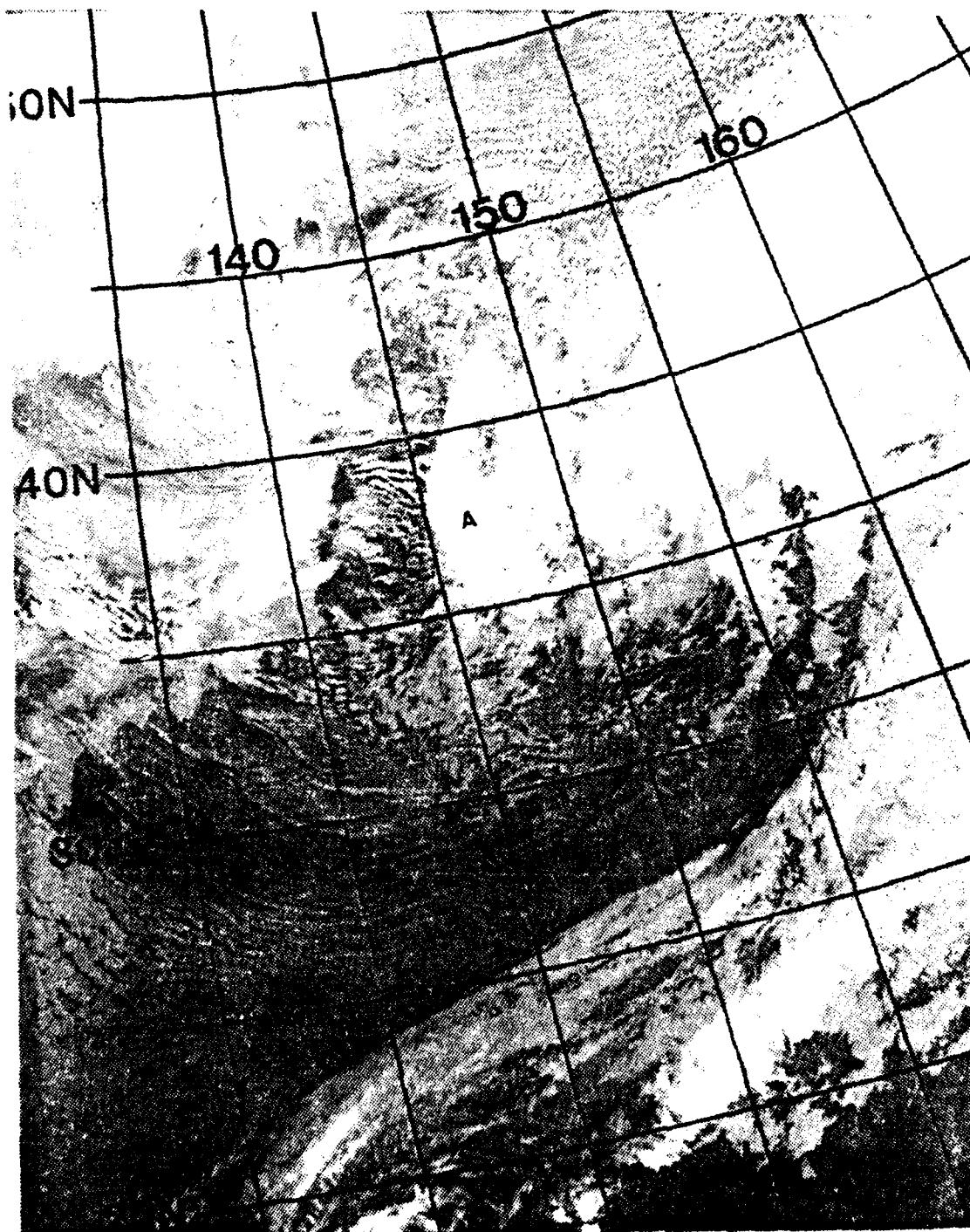


Figure 13. Similar to Figure 10 Except for 1405 GMT 13 January 1979. Label A Indicates Convection to the West of the Storm Center.

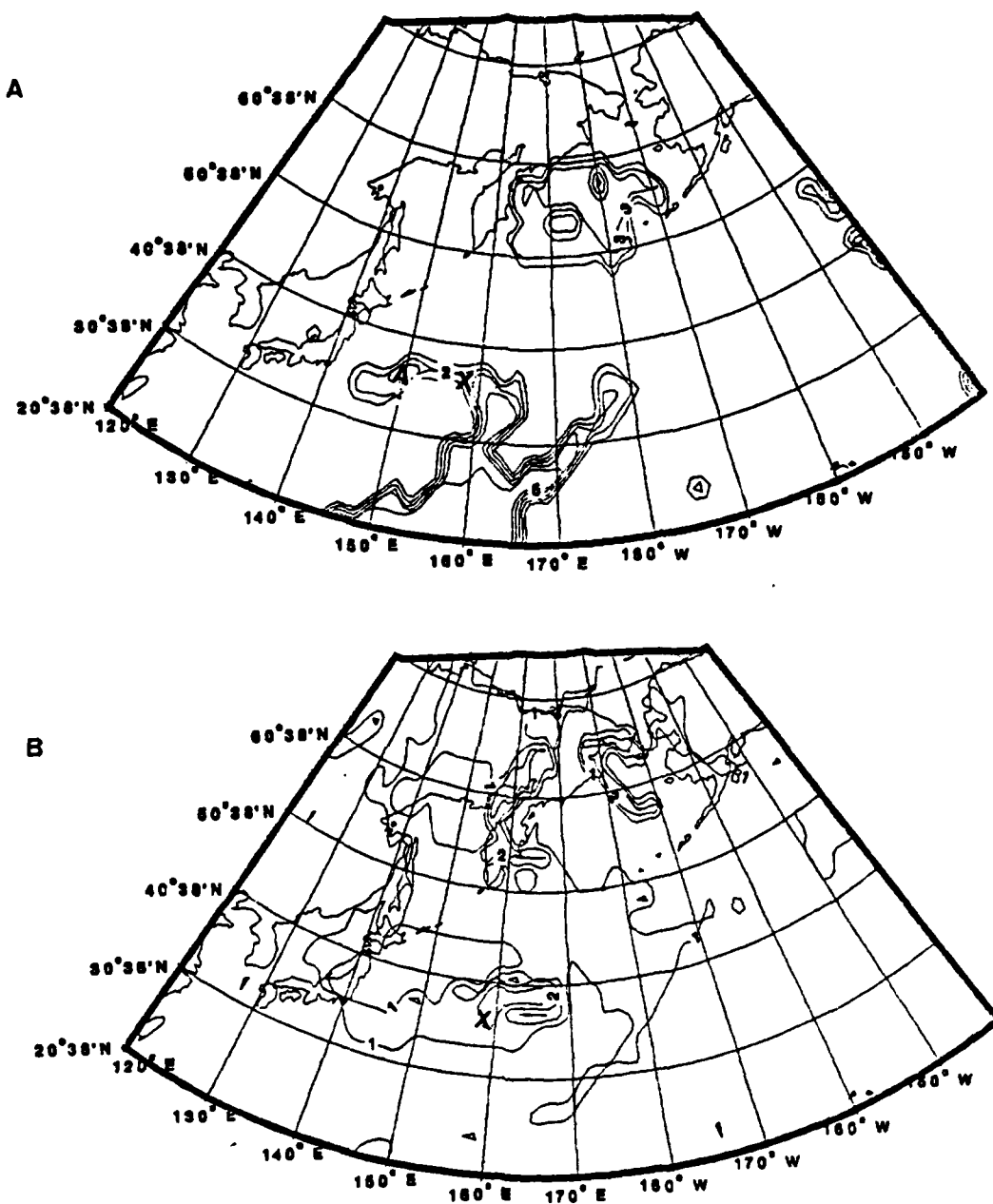


Figure 14. Similar to Figure 11 Except for 12 GMT 13 January 1979.

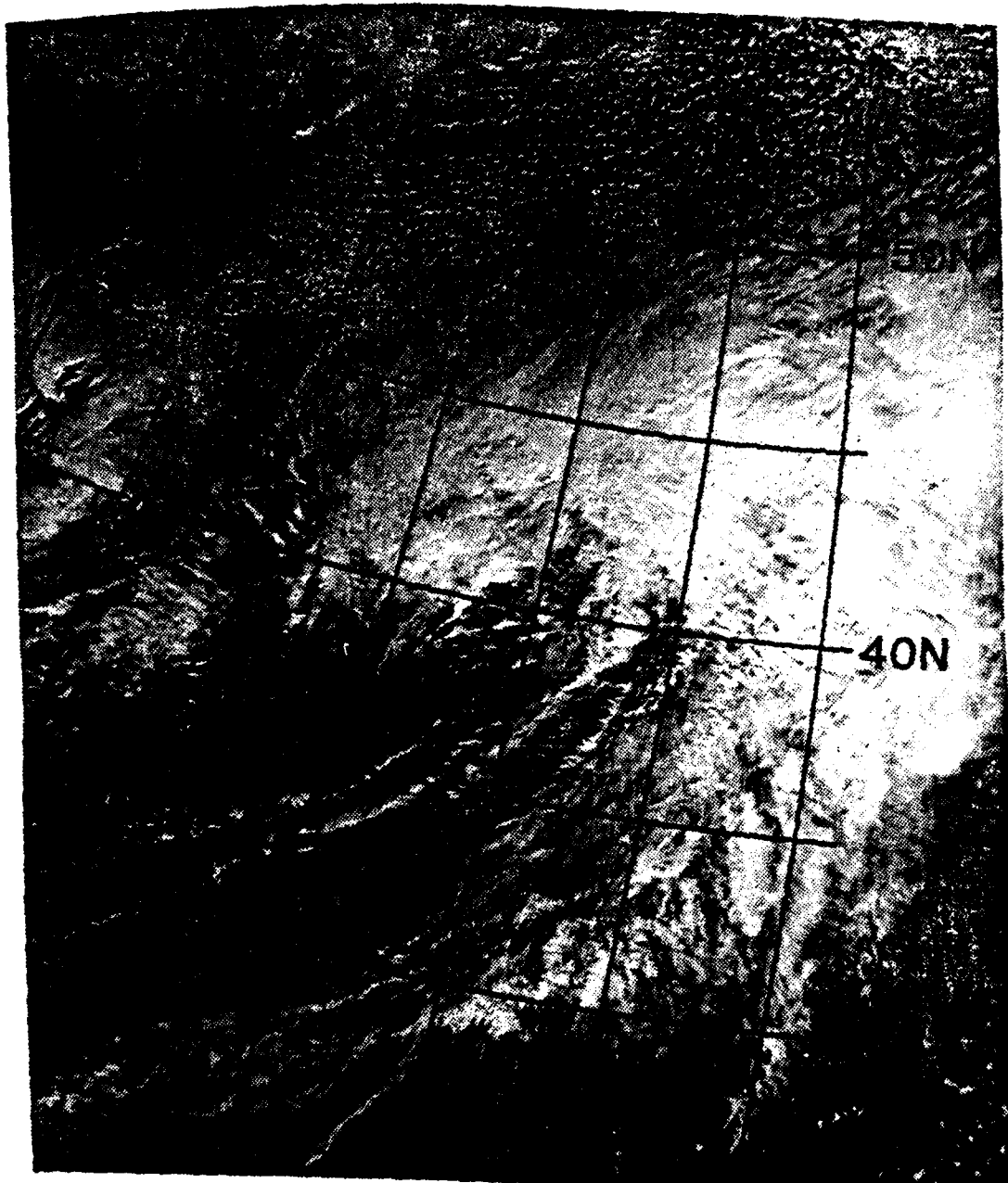


Figure 15. Similar to Figure 9 Except for 0023 GMT 14 January 1979. Label A Identifies Approaching Polar Low.



Figure 16. Similar to Figure 10 Except for 0023 GMT 14 January 1979. Label A Identifies Polar Low. Label B Indicates Low-level Frontal Clouds.

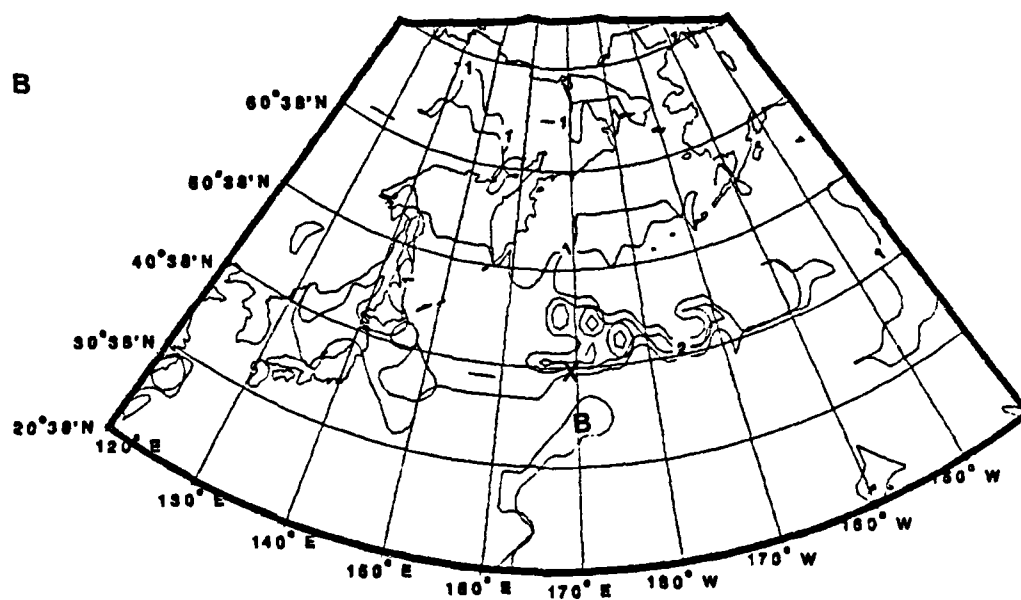
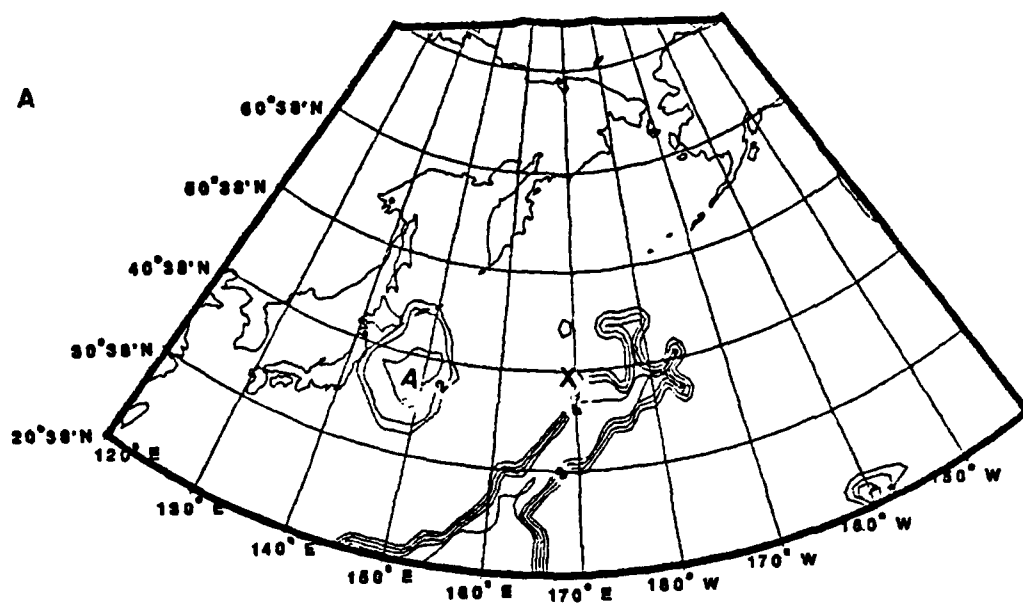


Figure 17. Similar to Figure 11 Except for 00 GMT 14 January 1979.

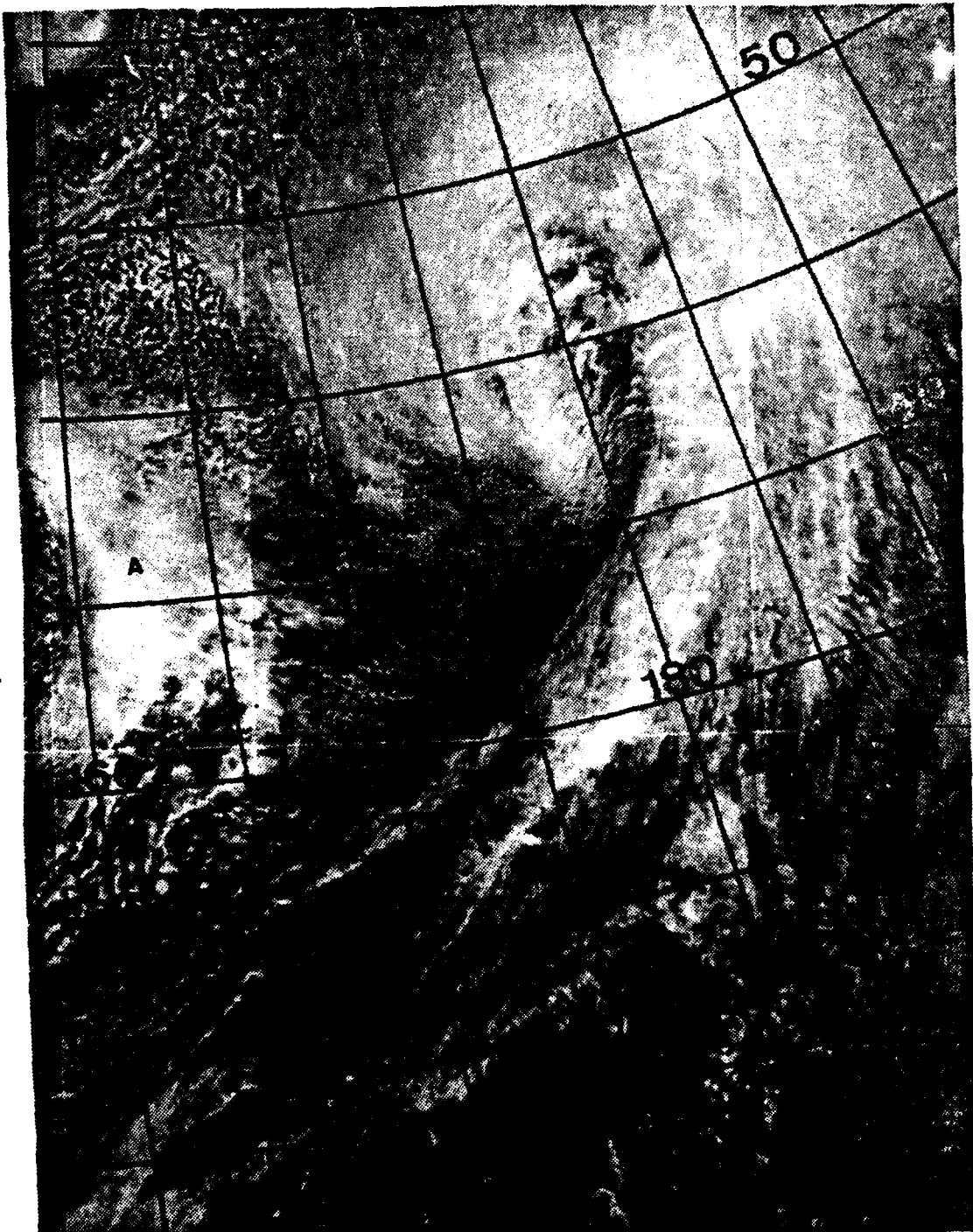


Figure 18. Similar to Figure 9 Except for 1205 GMT 14  
January 1979. Label A Identifies Secondary System.

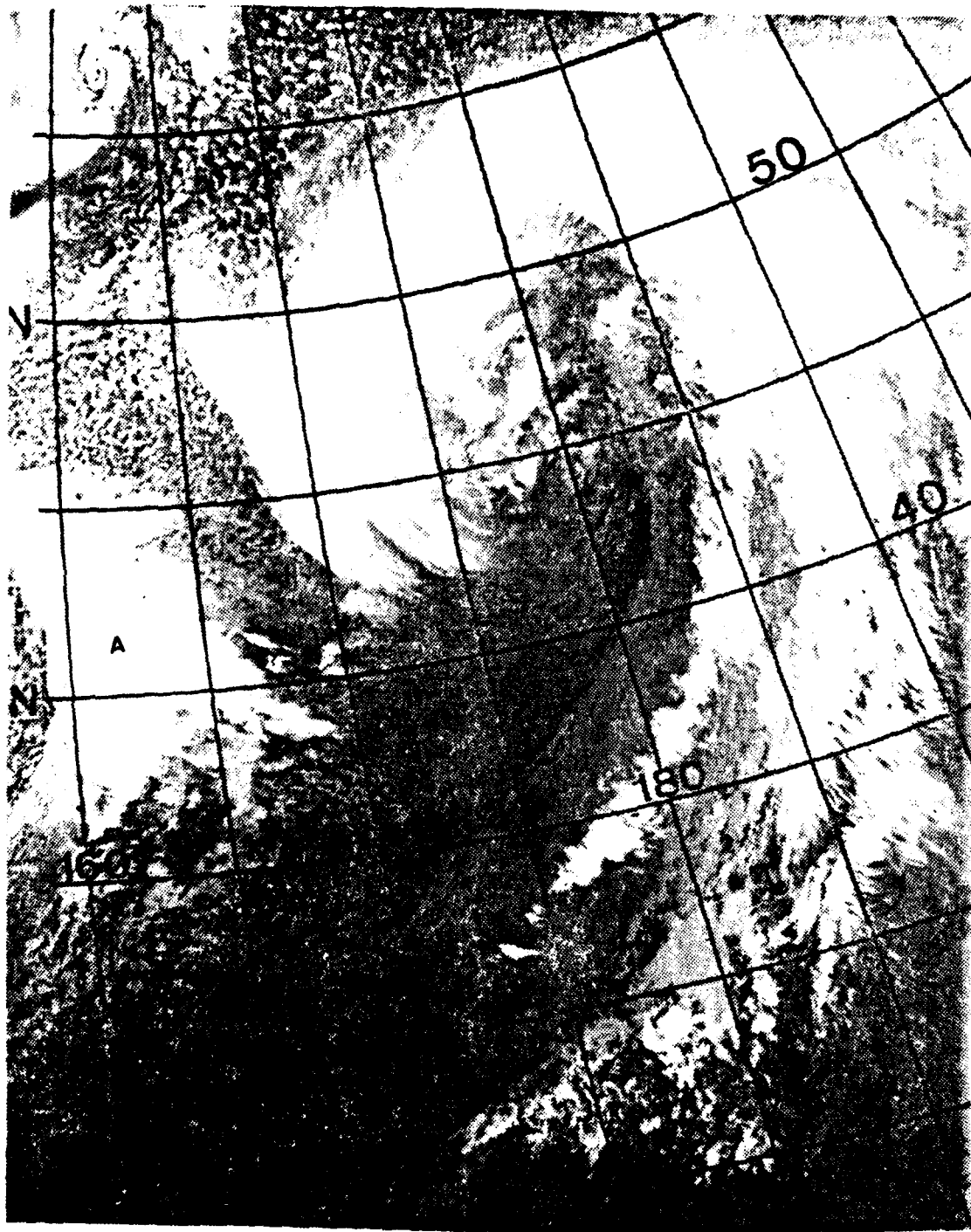


Figure 19. Similar to Figure 10 Except for 1205 GMT 14 January 1979. Label A Identifies Secondary System.



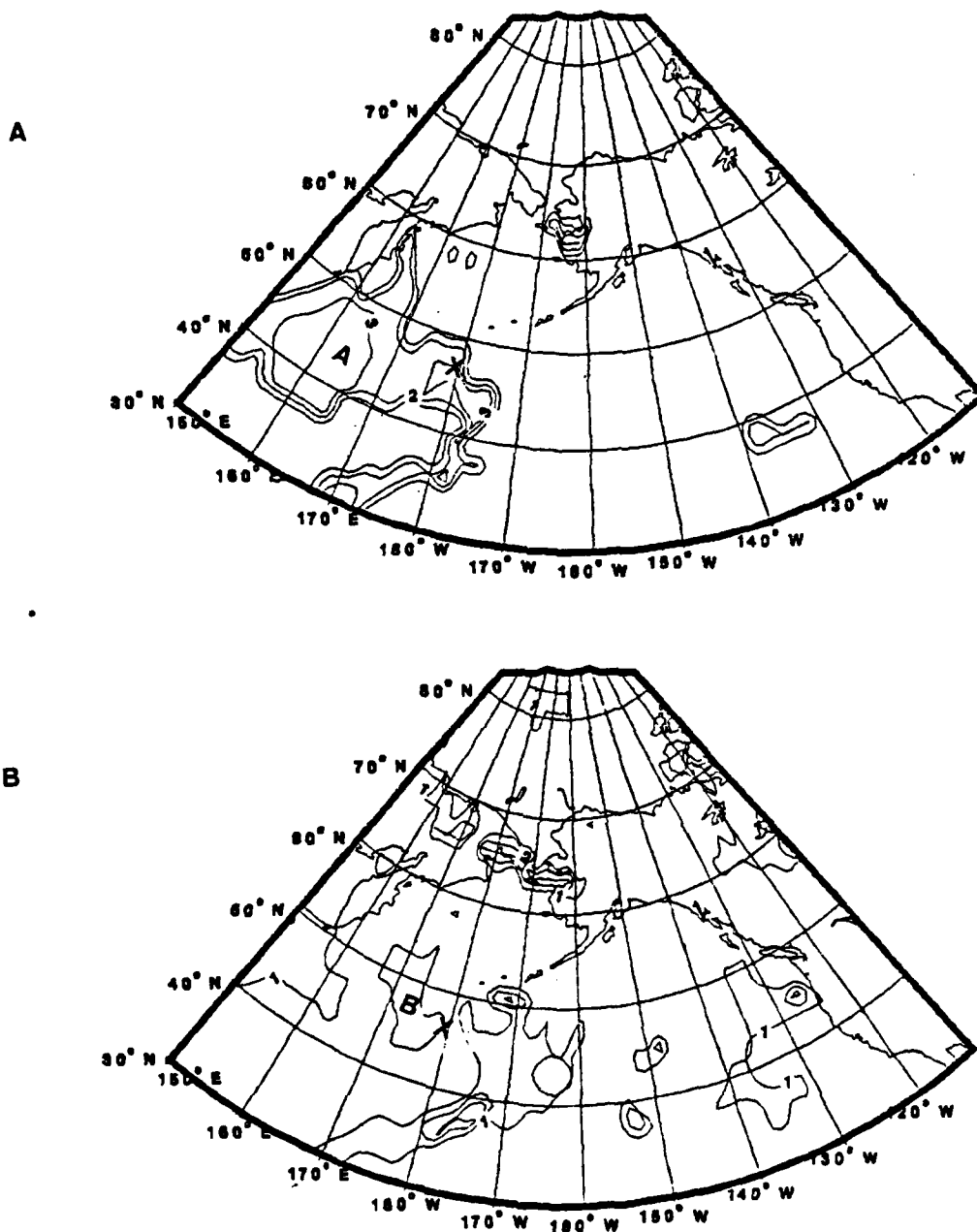


Figure 20. Similar to Figure 11 Except for 12 GMT 14 January 1979 and Southwest Corner of Grid Shifted to 30°N, 150°E.

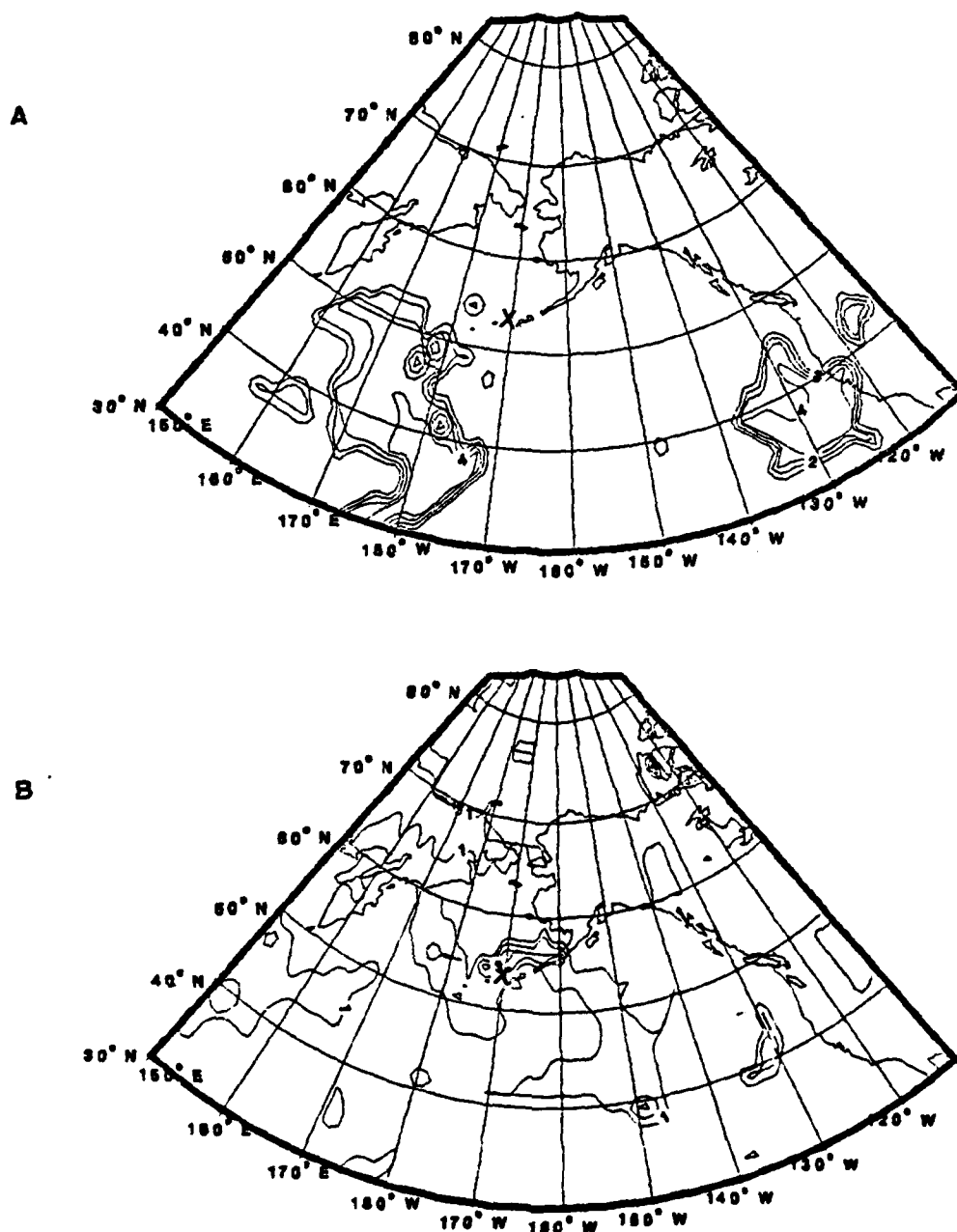


Figure 21. Similar to Figure 11 Except for 00 GMT 15 January 1979 and Southwest Corner of Grid Shifted to 30°N, 150°E.

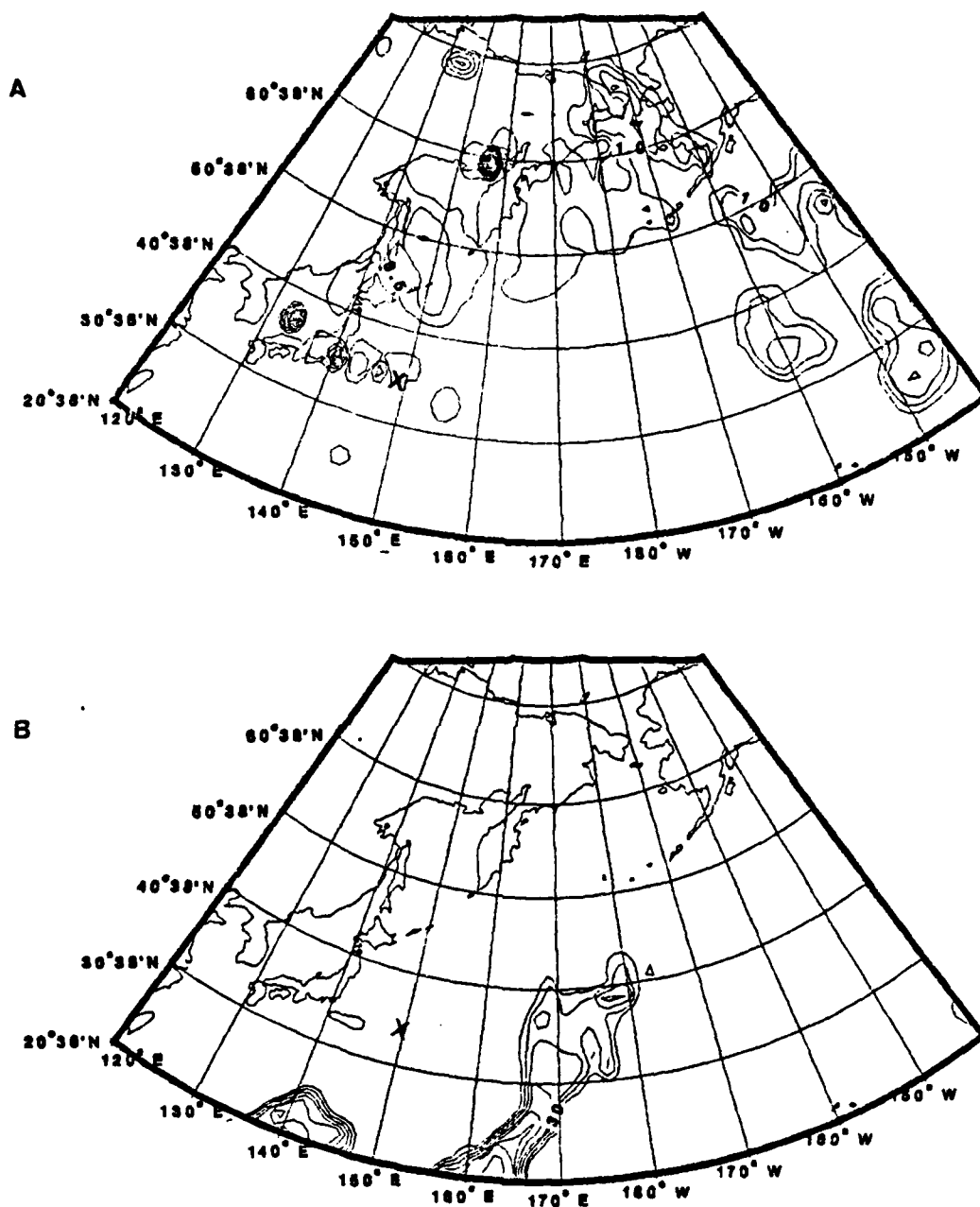


Figure 22. Condensation Heating Fields For 00 GMT 13 January 1979 For (A) Large-scale and (B) Convective. Units are K/day. Convective Contour Interval is 10.0. Large-scale Contour Interval is 0.5. Label X Identifies the Storm Center.

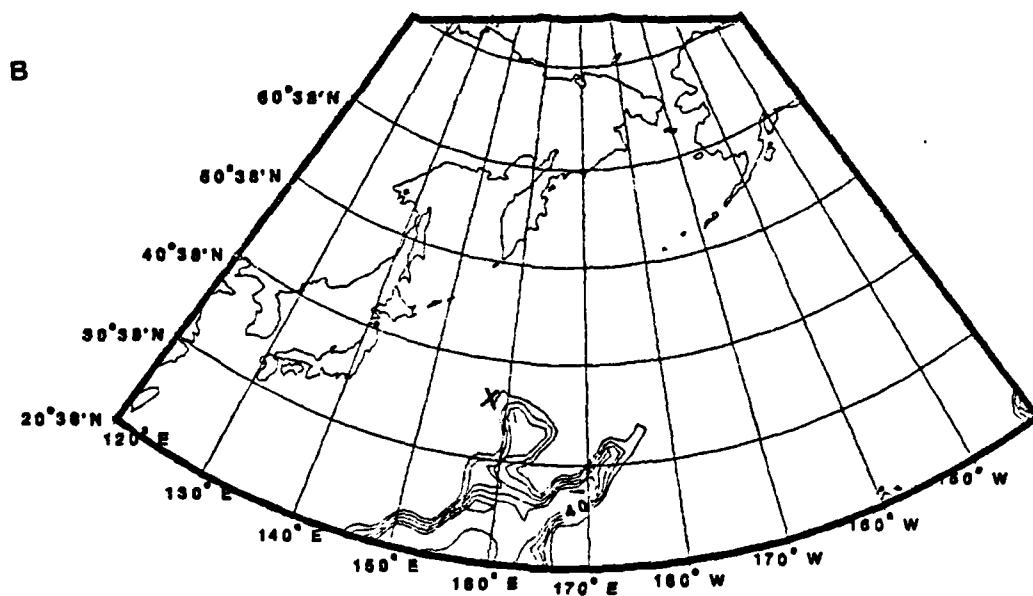
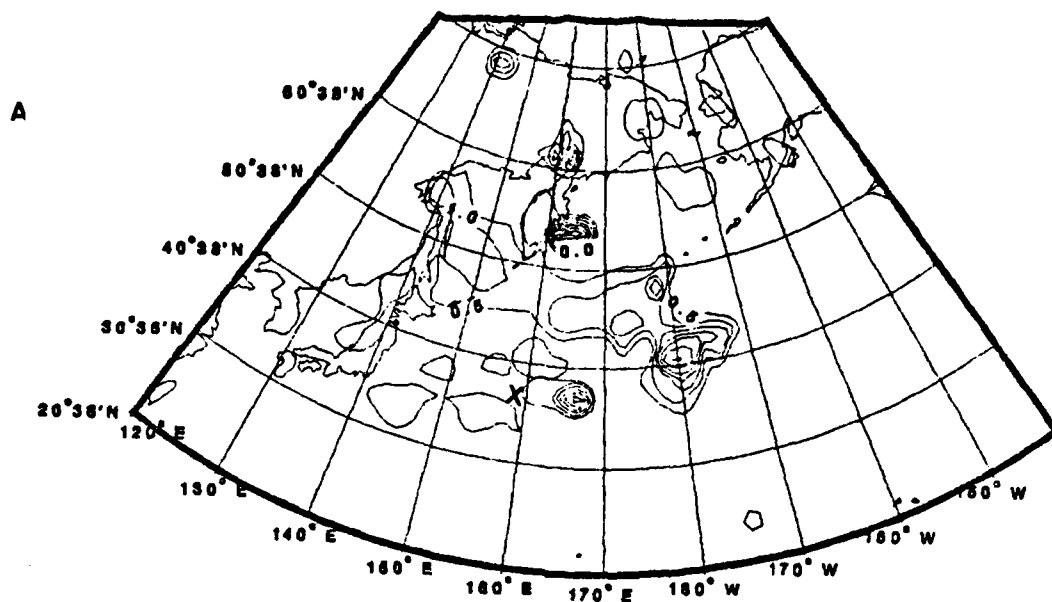


Figure 23. Similar to Figure 22 Except for 12 GMT 13 January 1979.

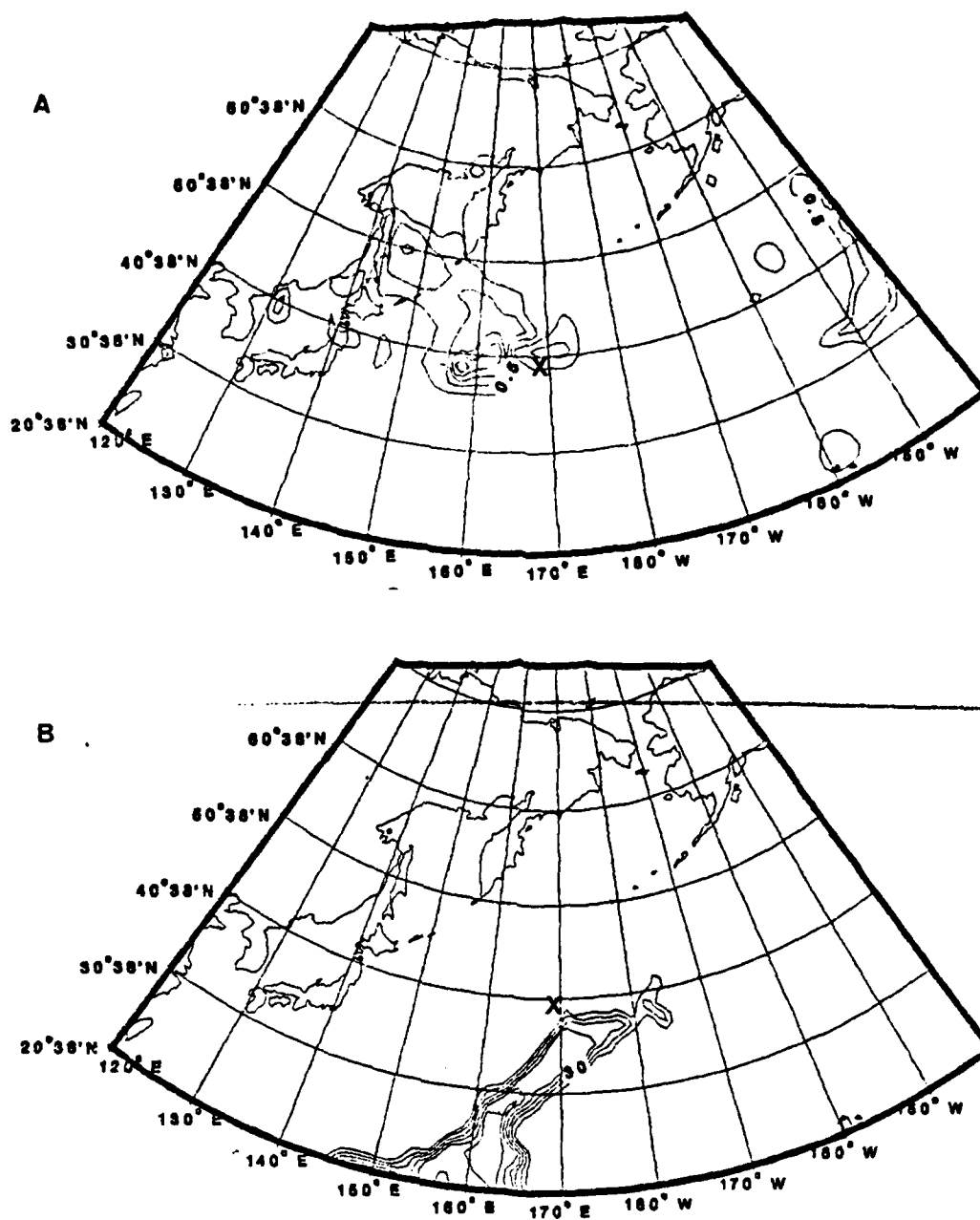
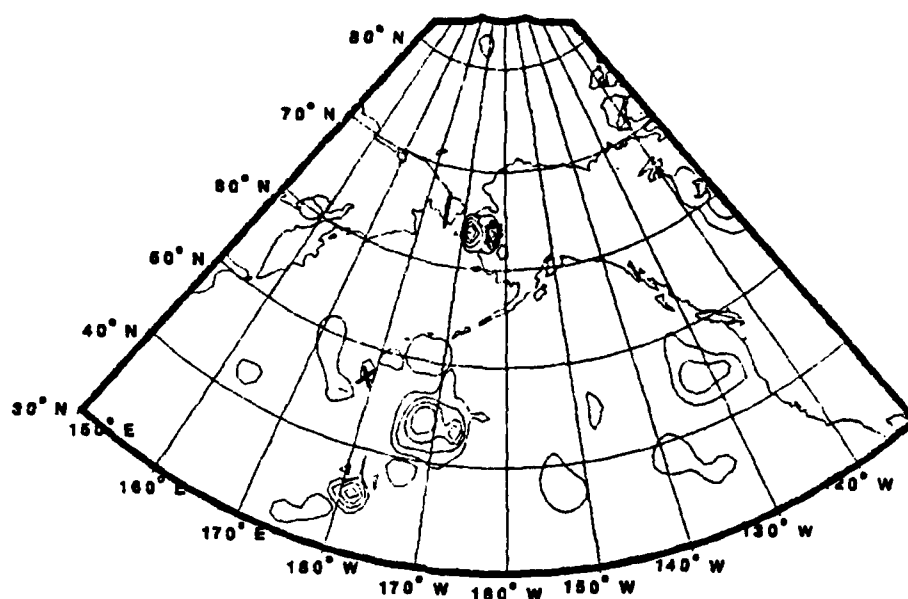


Figure 24. Similar to Figure 22 Except for 00 GMT 14 January 1979.

A



B

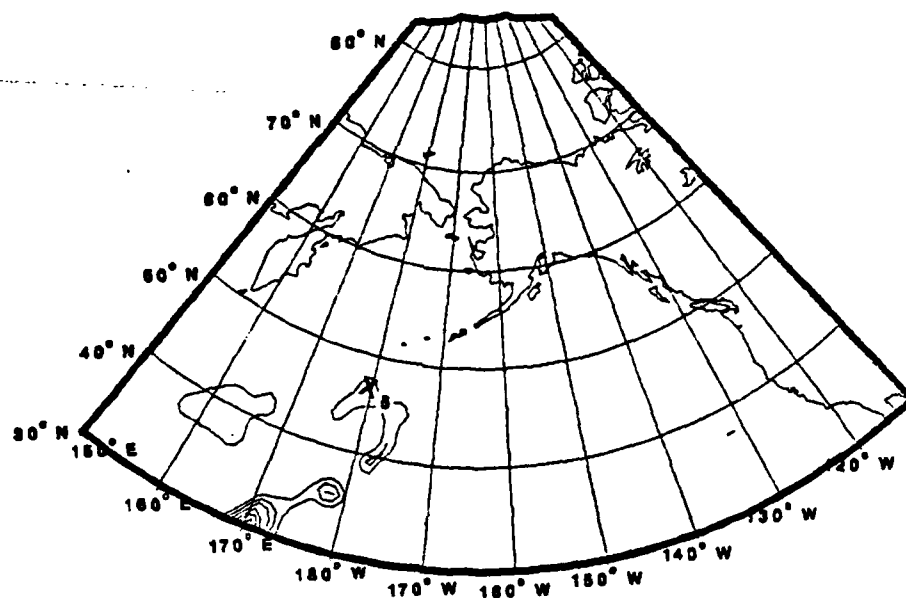


Figure 25. Similar to Figure 22 Except for 12 GMT 14 January 1979. Convective Contour Interval is 5.0. Southwest Corner of Grid Shifted to 30°N, 150°E.

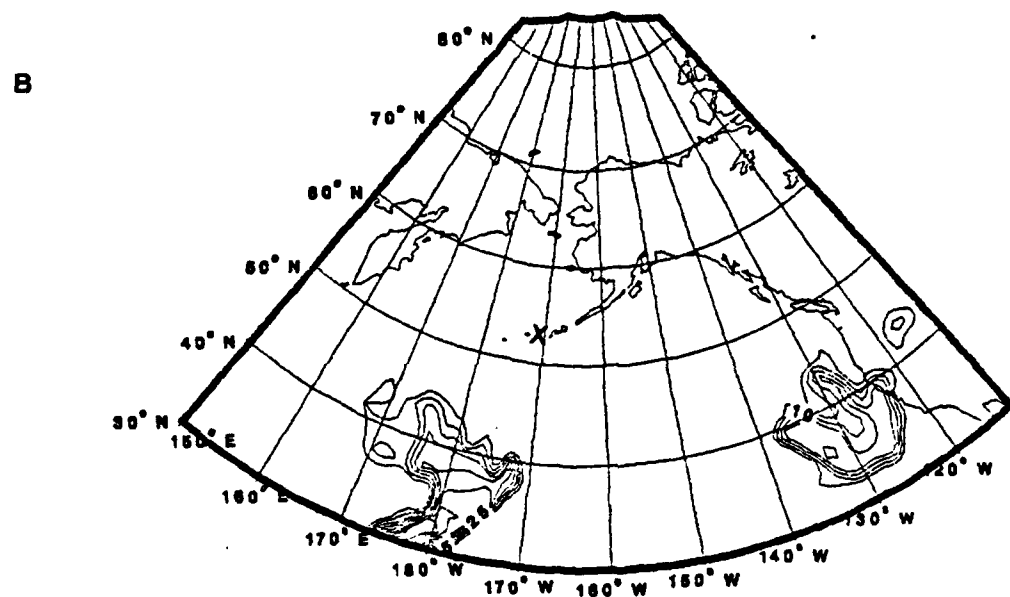
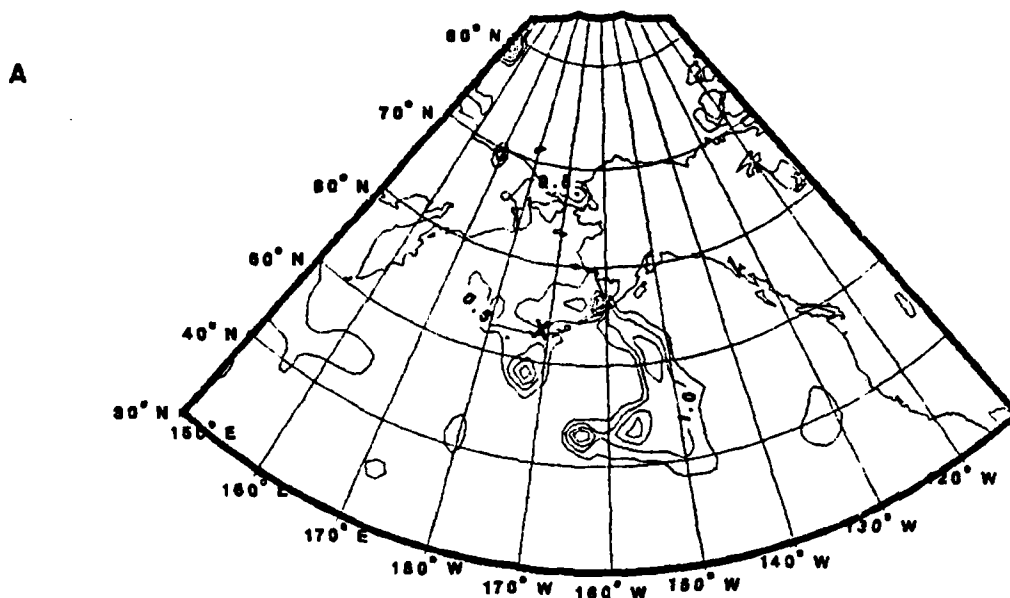


Figure 26. Similar to Figure 22 Except for 00 GMT 15 January 1979. Convective Contour Interval is 5.0. Southwest Corner of Grid Shifted to 30°N, 150°E.

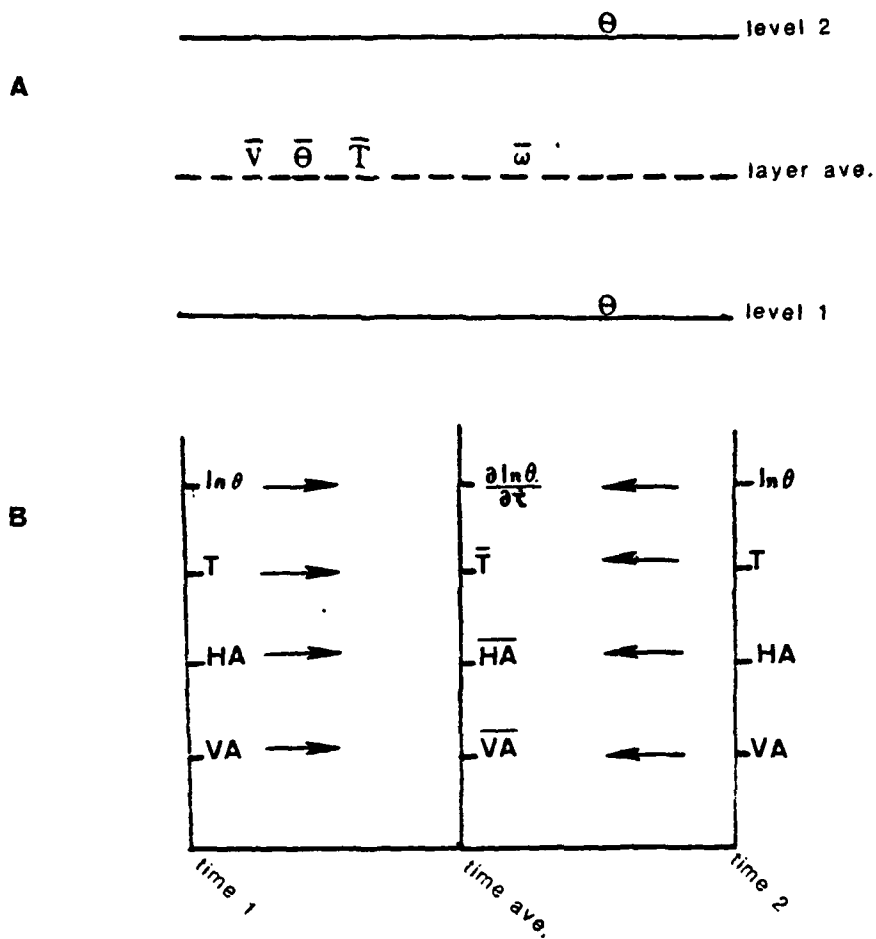


Figure 27. Distribution of Budget Parameters. (A) Layer Averaged and Level Parameters, (B) Time Differencing and Time Averaging Applied. H.A. Refers to Horizontal Advection. V.A. Refers to Vertical Advection.



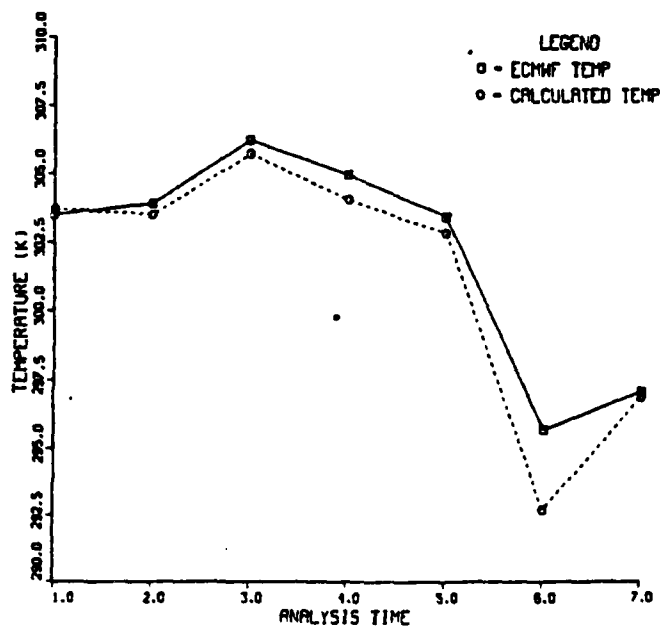


Figure 28. Layer Potential Temperature from ECMWF Initialization and Height Analysis for 700-500 mb Layer at Radius 6. Analysis Time 1 Refers to 0000 GMT 12 January 1979. Subsequent Times are Incremented by 12 h.

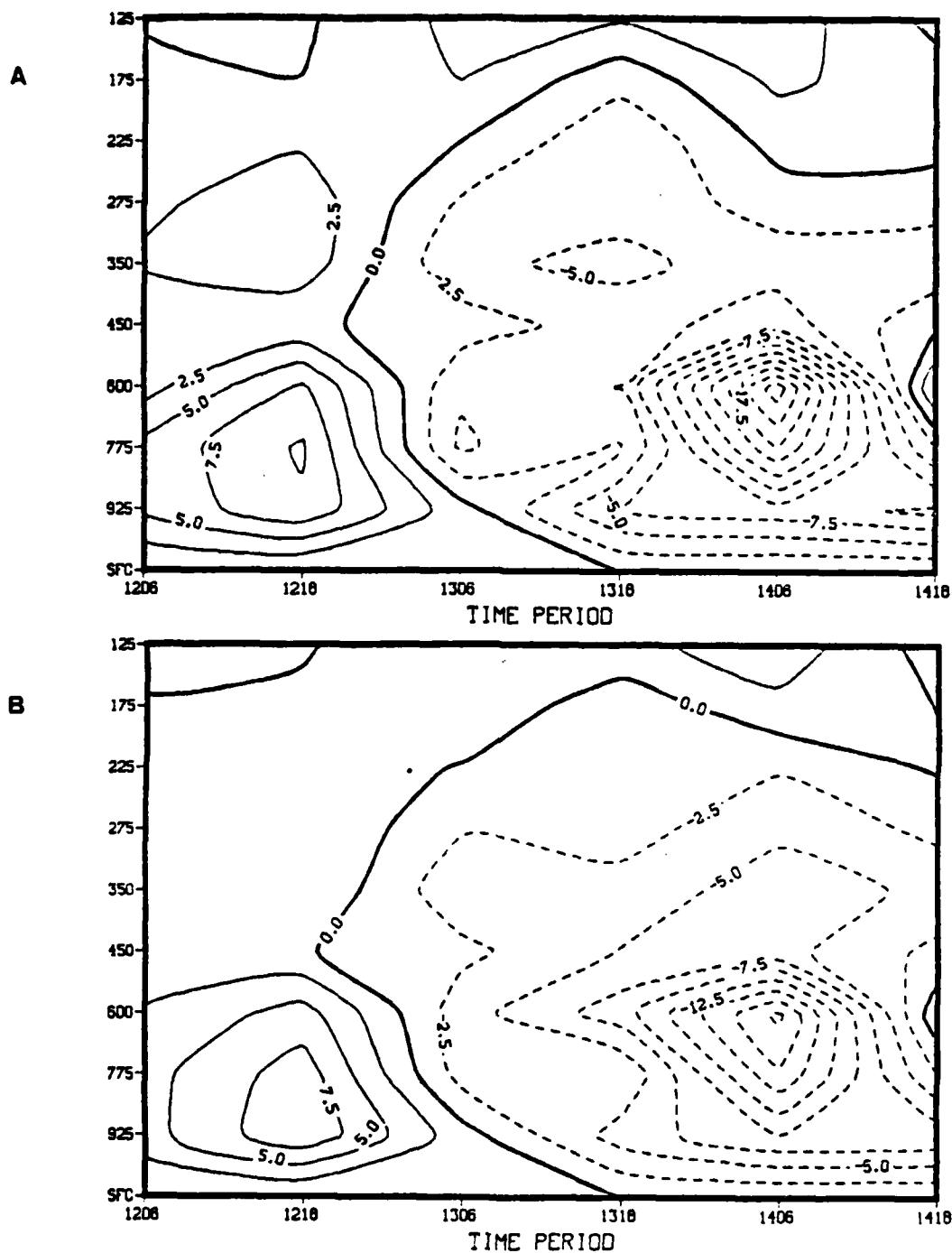


Figure 29. Temperature Time Tendency Time Sections for (A) Radius 6 and (B) Radius 10. Contour Interval is 2.5. Units are K/day. Dashed (Negative) Values Indicate Cooling. Period 1206 Refers to 00-12 GMT 12 January 1979.

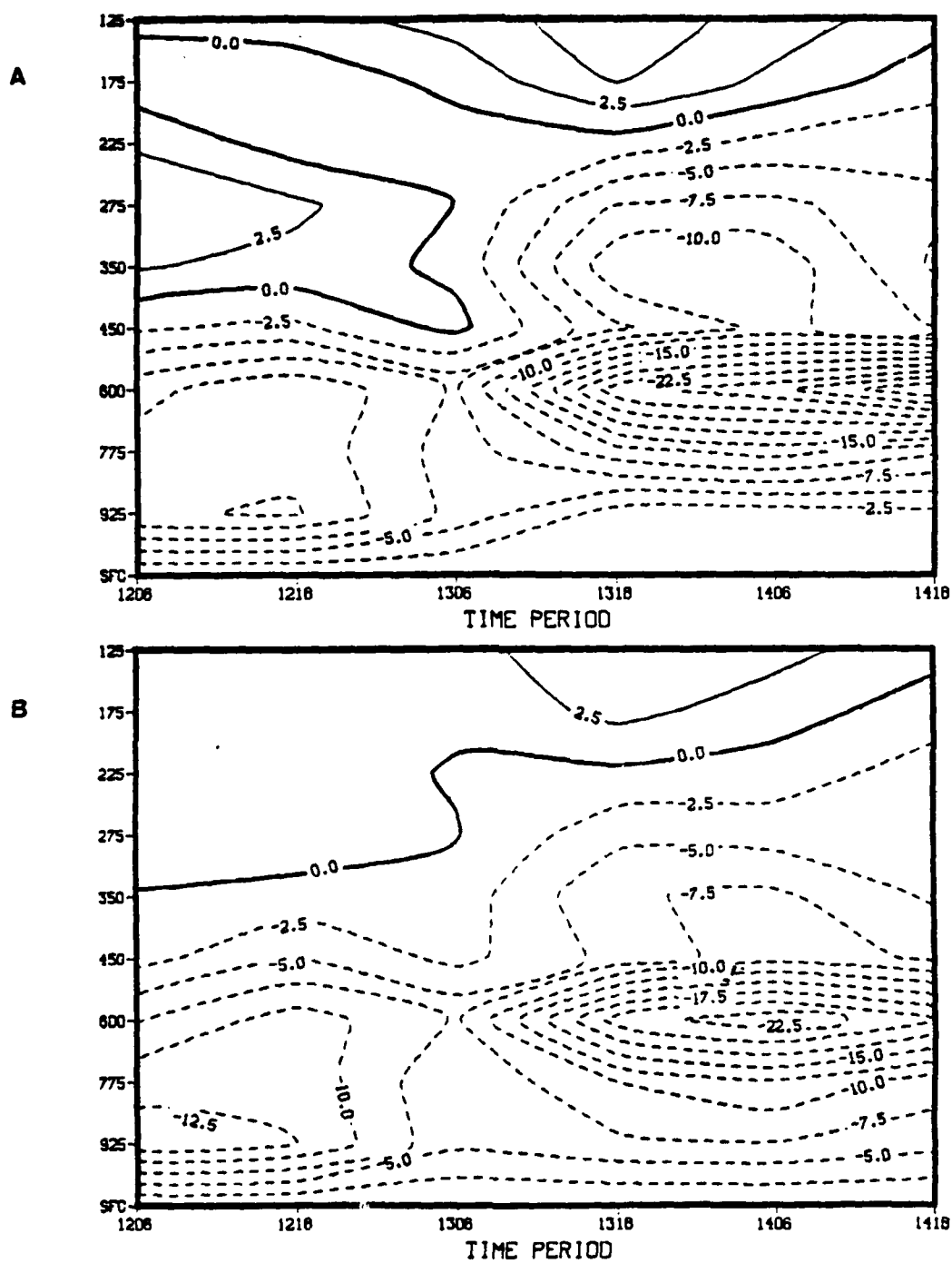


Figure 30. Advective Temperature Tendency Time Sections For (A) Radius 6 and (B) Radius 10. Units and Contours as in Figure 29.

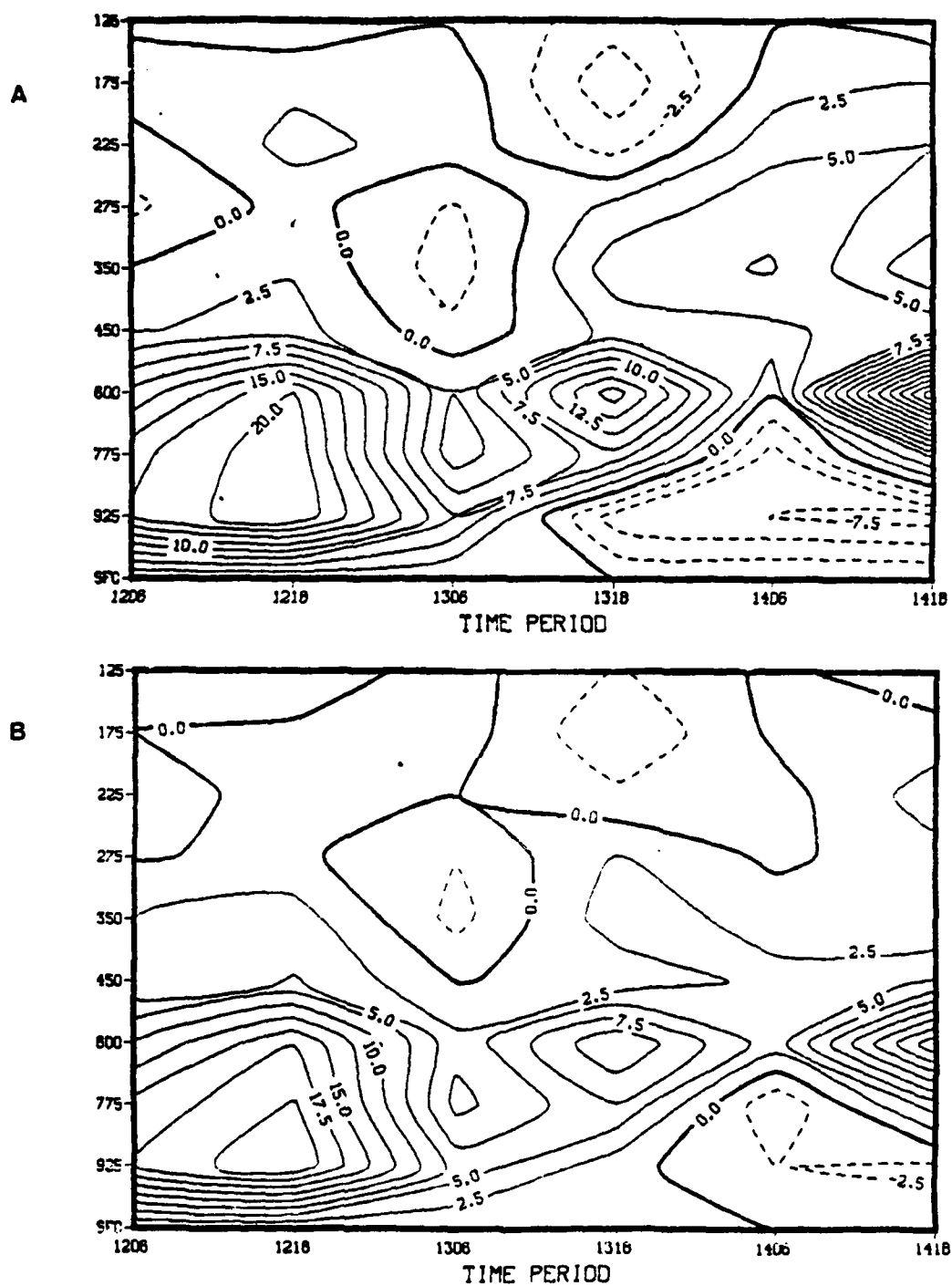


Figure 31. Diabatic Residual Temperature Tendency Time Section for (A) Radius 6 and (B) Radius 10. Units and Contours as in Figure 29.

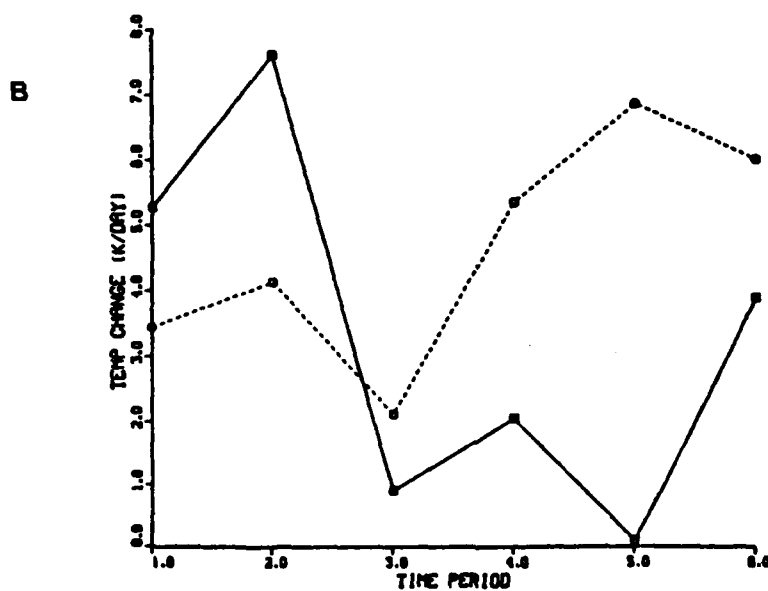
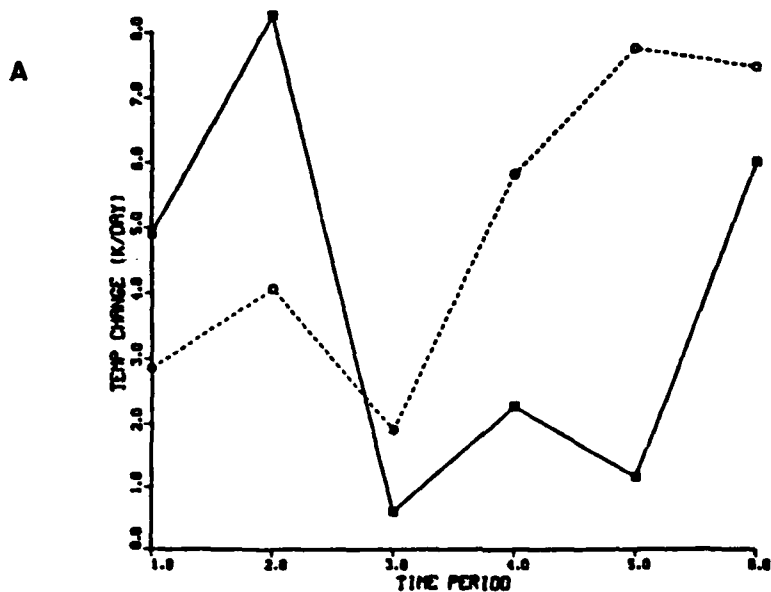


Figure 32. Budget Residual (Solid) and Advective (Dashed) Column-Averaged Temperature Tendency for (A) Radius 6 and (B) Radius 10. Advective Values Are Multiplied by -1. Units Are K/Day. Time Period 1 Refers to 1206. Subsequent Time Periods Are Incremented by 12 h.

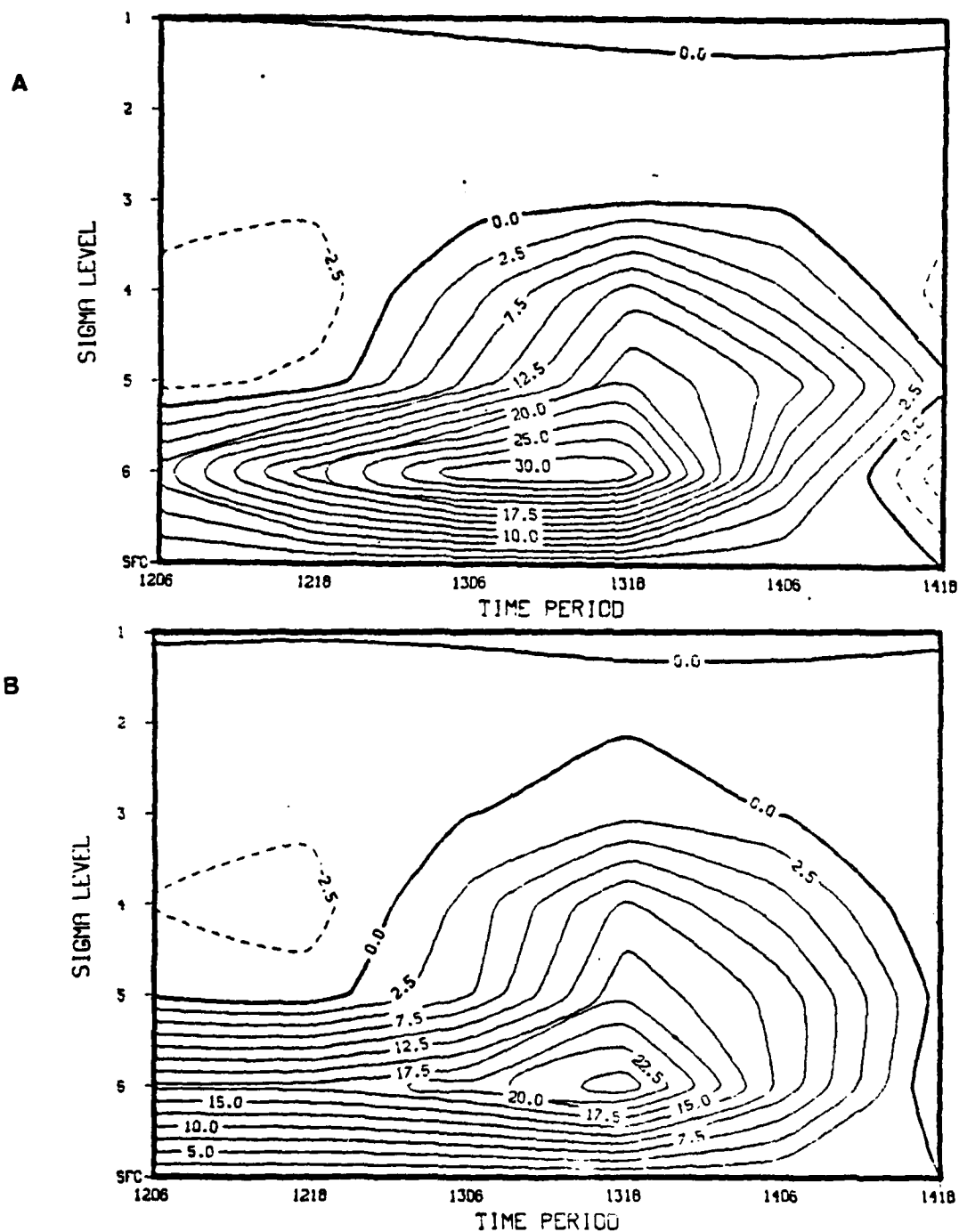


Figure 33. NOGAPS Total Diabatic Tendency Time Sections For (A) Radius 6 and (B) Radius 10. Units and Contours as in Figure 29. Vertical Coordinate Represents Sigma Levels.

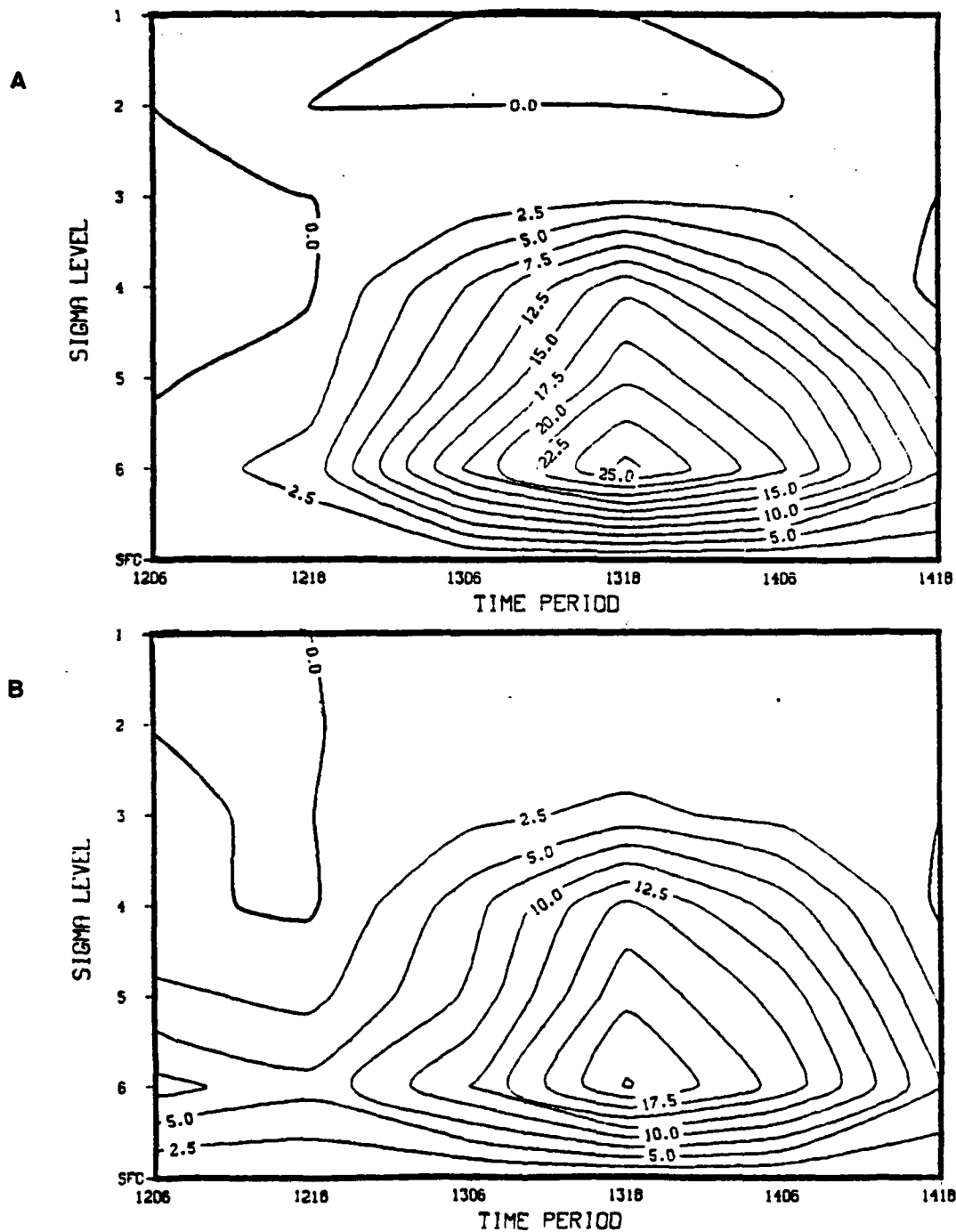


Figure 34. NOGAPS Convective Condensation Temperature Tendency Time Sections For (A) Radius 6 and (B) Radius 10. Units and Contours as in Figure 29.

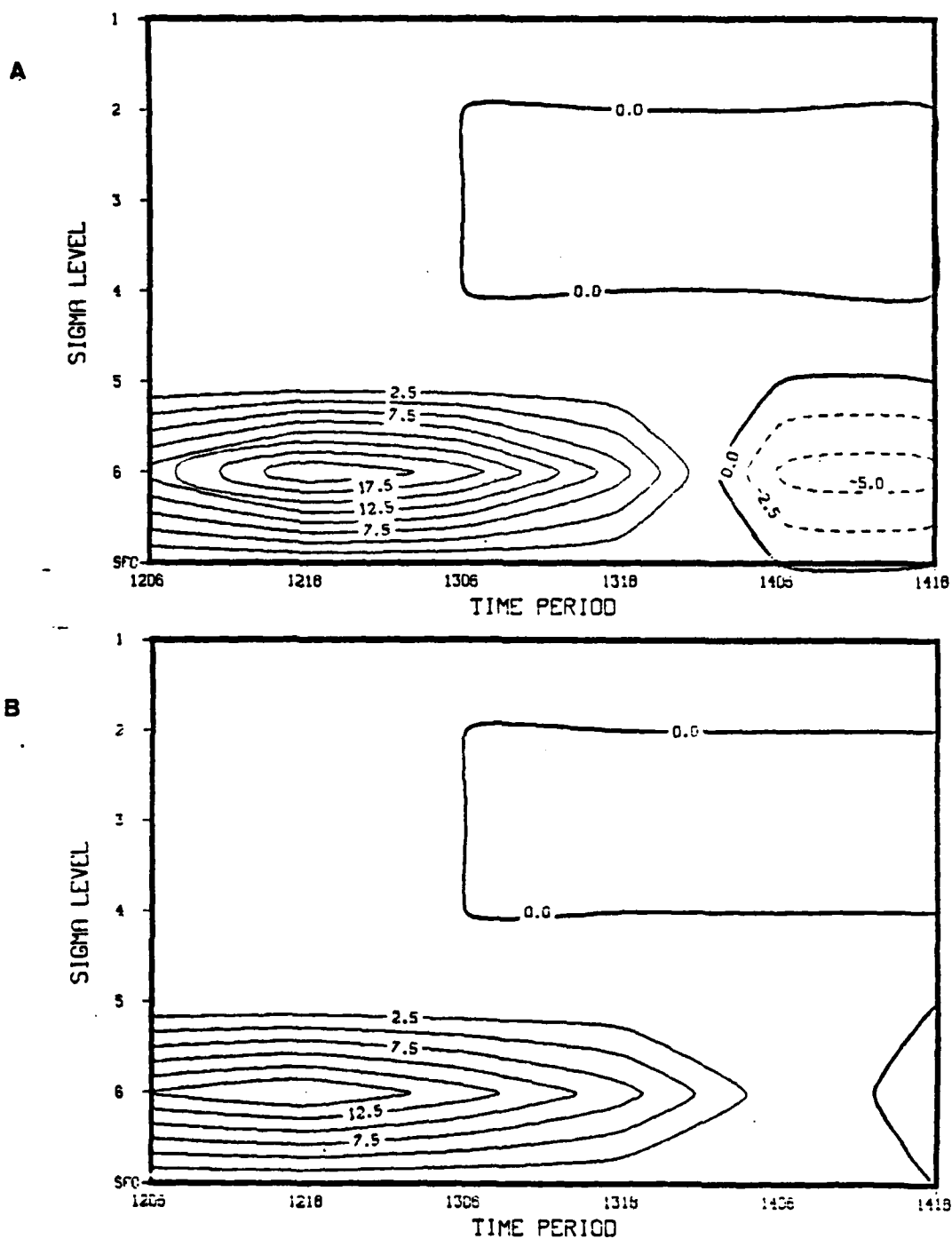


Figure 35. NOGAPS Eddy Transport of Sensible Heating Time Sections for (A) Radius 6 and (B) Radius 10. Units and Contours as in Figure 29.



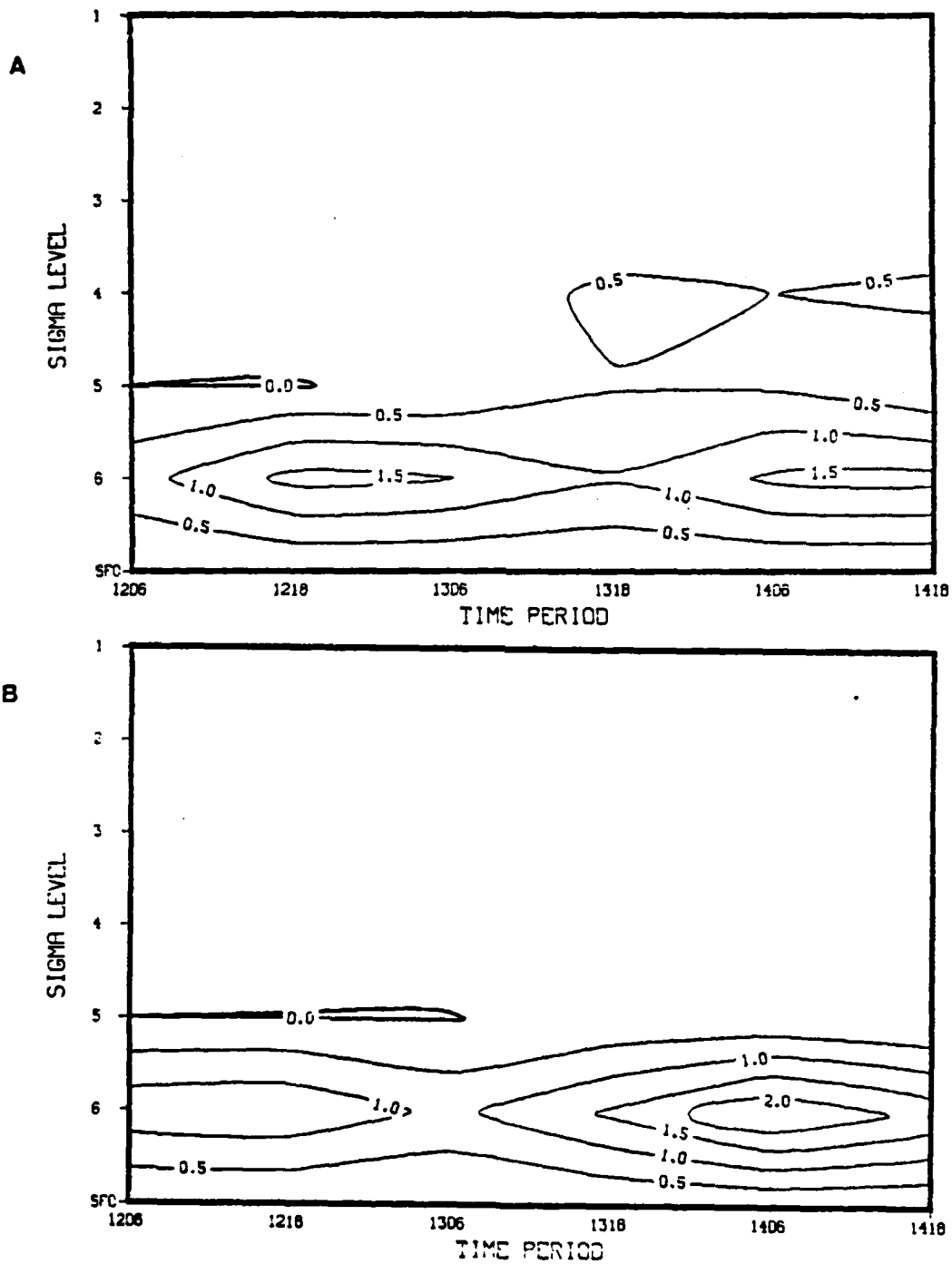


Figure 36. NOGAPS Large-scale Condensation Temperature Tendency Time Sections For (A) Radius 6 and (B) Radius 10. Units as in Figure 29. Contour Interval is 0.5.

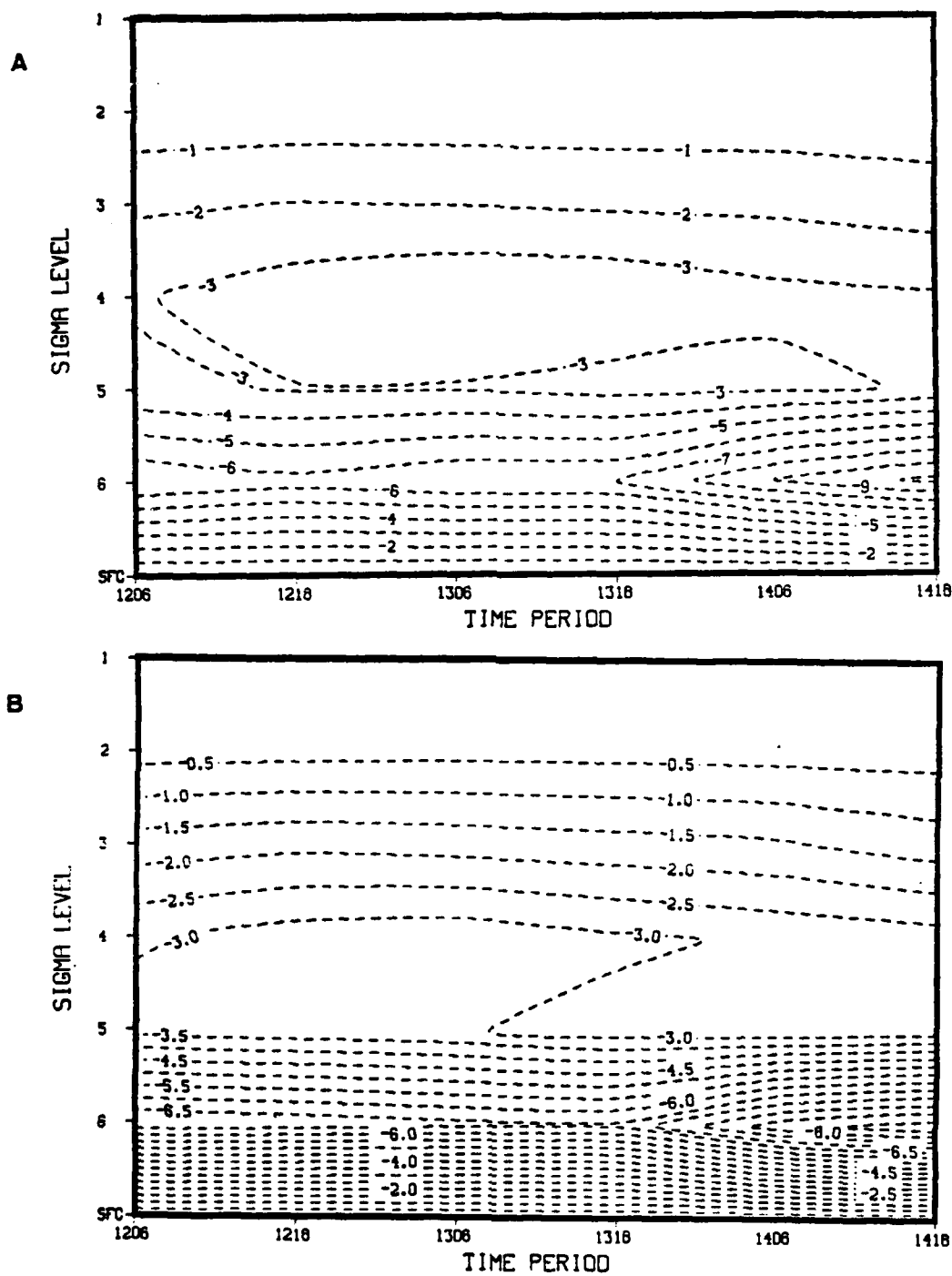


Figure 37. NOGAPS Long-wave Radiation Temperature Tendency Time Sections For (A) Radius 6 and (B) Radius 10. Units as in Figure 29. Contour Interval is 0.5.

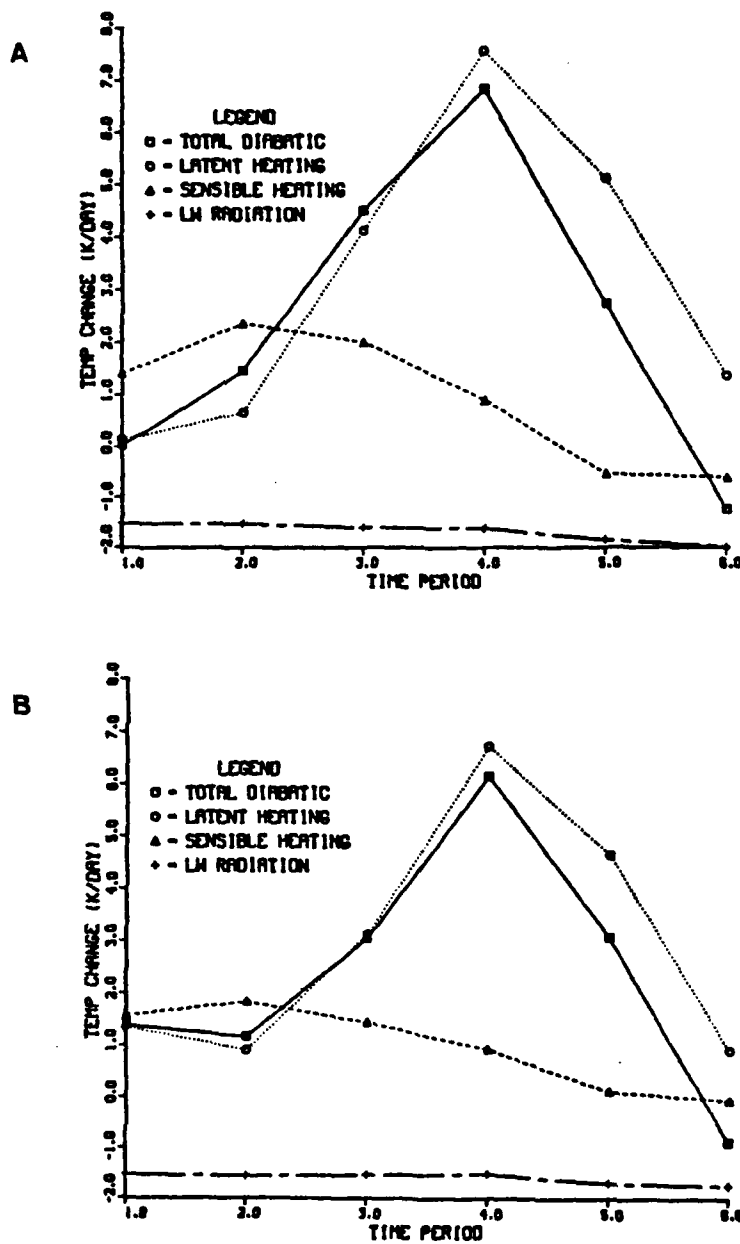


Figure 38. NOGAPS Column-averaged Total Diabatic, Latent Heating, Eddy Sensible Heating and Long-wave Radiation Temperature Tendencies For (A) Radius 6 and (B) Radius 10. Times and Units as in Figure 36.

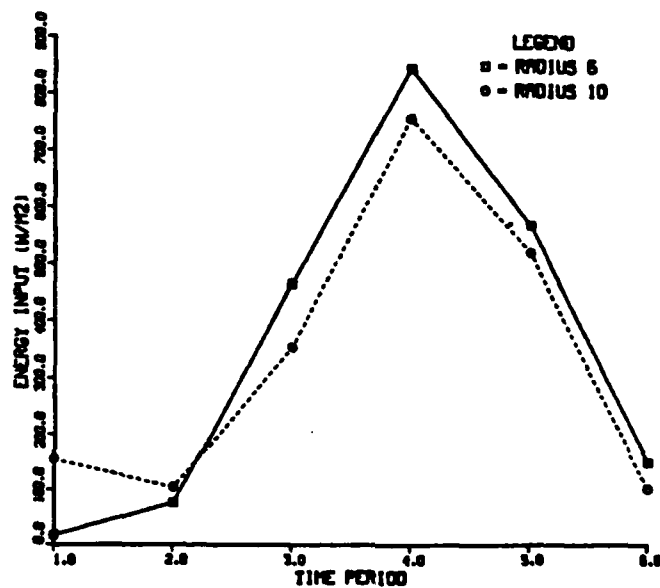


Figure 39. NOGAPS Latent Heating Energy Input For Radius 6 and Radius 10. Units are in  $\text{W/m}^2$ . Times as in Figure 36.

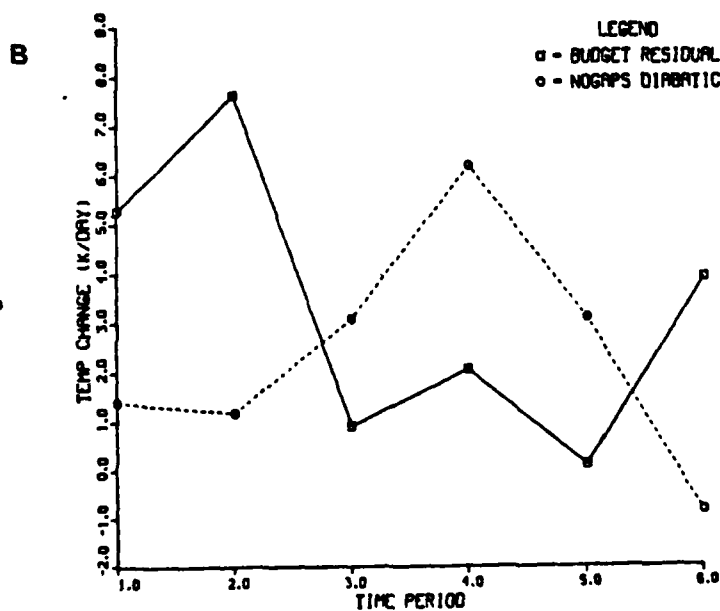
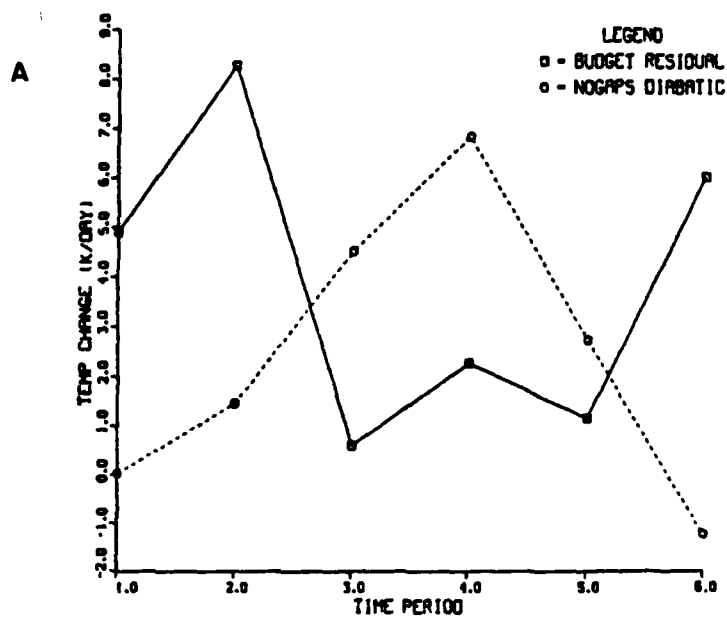


Figure 40. Column-averaged Budget Residual and NOGAPS Total Diabatic Temperature Tendencies For (A) Radius 6 and (B) Radius 10. Times and Units as in Figure 36.

### LIST OF REFERENCES

- Anthes, R.A., Y. Kuo, J. Gyakum, 1983: Numerical simulations of a case of explosive marine cyclogenesis. Mon. Wea. Rev., 111, 1174-1188.
- Arakawa, A., and V.R. Lamb, 1977: Computational design of the basic dynamical processes of the UCLA general circulation model, in Methods in Computational Physics, Vol. 17, Academic Press, Inc., New York.
- \_\_\_\_\_, and W.H. Schubert, 1974: Interaction of a cumulus cloud ensemble with the large-scale environment, Part I. J. Atmos. Sci., 31, 674-701.
- Aubert, E.F., 1957: On the release of latent heat as a factor in large-scale atmospheric motions. J. Meteor., 14, 527-542.
- Bengtsson, L., M. Kanamitsu, P. Kallberg and S. Uppala, 1982: FGGE 4-dimensional data assimilation at ECMWF. Bull. Amer. Meteor. Soc., 63, 29-43.
- Bosart, L.F., 1981: The President's Day snowstorm of 18-19 February 1979: a subsynoptic scale event. Mon. Wea. Rev., 109, 1542-1566.
- \_\_\_\_\_, and S.C. Lin, 1984: A diagnostic analysis of the President's Day snowstorm of February 1979. Manuscript submitted to Mon. Wea. Rev.
- Bullock, B.R., and D.R. Johnson, 1971: The generation of available potential energy by latent heat release in a mid-latitude cyclone. Mon. Wea. Rev., 99, 1-14.
- Calland, W.E., 1983: Quasi-Lagrangian Diagnostics Applied to an Extratropical Explosive Cyclogenesis in the North Pacific. M.S. Thesis, Naval Postgraduate School, 154 pp.
- Chen, T.C., C.B. Chang and D.J. Perkey, 1983: Numerical study of an AMTEX'75 oceanic cyclone. Mon. Wea. Rev., 111, 1818-1829.
- Chou, S.H., and D. Atlas, 1982: Satellite estimates of air-ocean heat fluxes during cold air outbreaks. Mon. Wea. Rev., 110, 1434-1450.

- Danard, M.B., 1964: On the influence of released latent heat on cyclone development. J. Appl. Meteor., 3, 27-37.
- \_\_\_\_\_, 1966: On the contribution of released latent heat to changes in available potential energy. J. Appl. Meteor., 5, 81-84.
- \_\_\_\_\_, and G.E. Ellenton, 1980: Physical influences on East Coast cyclogenesis. Atmosphere-Ocean, 18, 65-82.
- Deardorff, J.W., 1972: Parameterization of the planetary boundary layer for use in general circulation models. Mon. Wea. Rev., 100, 93-106.
- Elsberry, R.L., F.J. Winninghoff and C.S. Liou, 1984: Some aspects of post-frontal convective areas along the west coast of the United States. Unpublished manuscript, Department of Meteorology, Naval Postgraduate School, Monterey, Ca.
- Gall, R.L., and D.R. Johnson, 1971: The generation of available potential energy by sensible heating: a case study. Tellus, XXIII, 465-482.
- Gyakum, J.R., 1983: On the evolution of the QE II storm. II Dynamic and thermodynamic structure. Mon. Wea. Rev., 111, 1156-1173.
- Holton, J.R., 1979: An Introduction to Dynamic Meteorology. Academic Press, Inc., New York. 391 pp.
- Johnson, D.R., and W.K. Downey, 1975a: Azimuthally averaged transport and budget equations for storms: quasi-Lagrangian diagnostics 1. Mon. Wea. Rev., 103, 967-979.
- \_\_\_\_\_, 1975b: The absolute angular momentum of storms: quasi-Lagrangian diagnostics 2. Mon. Wea. Rev., 103, 1063-1076.
- Katayama, A., 1972: A simplified scheme for computing radiative transfer in the troposphere. Tech Report No. 6. Dept. of Meteorology, UCLA.
- Lord, S.J., 1982: Interaction of a cumulus cloud ensemble with the large-scale environment. Part III: semi-prognostic test of the Arakawa-Schubert cumulus parameterization. J. Atmos. Sci., 39, 88-103.
- Mak, M., 1982: On moist quasi-geostrophic baroclinic instability. J. Atmos. Sci., 39, 2028-2037.

- Margules, M., 1903: Über die energie der sturme. Jahr.kais-  
kon Zent. fur met., Vienna (English translation by C.  
Abbe in Smithson, Misc. Coll., 51, 1910, 533-595) .
- Manabe, S., 1956: On the contribution of heat released  
by condensation to the change in pressure pattern.  
JMS of Japan, 34, 308-320.
- Mullen, S.L., 1983: Explosive cyclogenesis associated with  
cyclones in polar air streams. Mon. Wea. Rev., 111,  
1537-1553.
- Petterssen, S., D.L. Bradbury and K. Pederson, 1962: The  
Norwegian cyclone models in relation to heat and cold  
sources. Geophy. Pub., 24, 243-280.
- \_\_\_\_\_, and S.J. Smebye, 1971: On the development of  
extratropical cyclones. Quart. J. Roy. Meteor. Soc., 97,  
457-482.
- Pyke, C.B., 1965: On the role of air-sea interaction in the  
development of cyclones. Bull. Amer. Meteor. Soc., 46,  
4-15.
- Randall, D.A., 1976: The Interaction of the Planetary  
Boundary Layer with Large-scale Circulations. Ph.D.  
Thesis, Dept. of Atmos. Sci., UCLA.
- Ranelli, P.H., 1984: Response of an Atmospheric Prediction  
Model to Time-dependent Sea-surface Temperatures. M.S.  
Thesis, Naval Postgraduate School, 98 pp.
- Rosmond, T.E., 1981: NOGAPS: Navy Operational Global  
Atmospheric Prediction System. Preprint volume, Fifth  
Conference on Numerical Weather Prediction, Monterey,  
Ca., published by the American Meteorological Society,  
Boston, Ma., 7479.
- Sanders, F., and J.R. Gyakum, 1980: Synoptic-dynamic  
climatology of the "Bomb". Mon. Wea. Rev., 108,  
1589-1606.
- Schlesinger, M.E., 1976: A Numerical Simulation of the  
General Circulation of Atmospheric Ozone. Ph.D. Thesis,  
Dept. Atmos. Sci., UCLA.
- Staley, D.O., and R.L. Gall, 1977: On the wavelength of  
maximum baroclinic instability. J. Atmos. Sci., 34,  
1679-1688.



Tracton, S.M., 1973: The role of cumulus convection in the development of extratropical cyclones. Mon. Wea. Rev., 101, 573-593.

Yanai, M., S.K. Esbensen and J.H. Chu, 1973: Determination of bulk properties of tropical cloud clusters from large-scale heat and moisture budgets. J. Atmos. Sci., 30, 611-627.

INITIAL DISTRIBUTION LIST

	No. Copies
1. Defense Technical Information Center Cameron Station Alexandria, VA 22314	2
2. Library, Code 0142 Naval Postgraduate School Monterey, CA 93943	2
3. Professor Robert J. Renard, Code 63Rd Department of Meteorology Naval Postgraduate School Monterey, CA 93943	1
4. Professor Christopher N.K. Mooers, Code 68Mr Department of Oceanography Naval Postgraduate School Monterey, CA 93943	1
5. Professor Carlyle H. Wash, Code 63Cw Department of Meteorology Naval Postgraduate School Monterey, CA 93943	9
6. Professor Russel L. Elsberry, Code 63Es Department of Meteorology Naval Postgraduate School Monterey, CA 93943	1
7. Lt. Thomas E. Bosse 127 Lyndale Ave. Baltimore, MD 21236	2
8. Lt. Raymond Toll, Code 63 Department of Meteorology Naval Postgraduate School Monterey, CA 93943	1
9. Director Naval Oceanography Division Naval Observatory 34th and Massachusetts Avenue NW Washington, D.C. 20390	1
10. Commander Naval Oceanography Command Central NSTL Station Bay St. Louis, MS 39522	1

- |     |                                                                                                                                    |   |
|-----|------------------------------------------------------------------------------------------------------------------------------------|---|
| 11. | Commanding Officer<br>Naval Oceanographic Office<br>NSTL Station<br>Bay St. Louis, MS 39522                                        | 1 |
| 12. | Commanding Officer<br>Fleet Numerical Oceanography Center<br>Monterey, CA 93940                                                    | 1 |
| 13. | Commanding Officer<br>Naval Ocean Research and Development<br>Activity<br>NSTL Station<br>Bay St. Louis, MS 39522                  | 1 |
| 14. | Commanding Officer<br>Naval Environmental Prediction<br>Research Facility<br>Monterey, CA 93940                                    | 1 |
| 15. | Chairman, Oceanography Department<br>U.S. Naval Academy<br>Annapolis, MD 21402                                                     | 1 |
| 16. | Chief of Naval Research<br>800 N. Quincy Street<br>Arlington, VA 22217                                                             | 1 |
| 17. | Office of Naval Research (Code 480)<br>Naval Ocean Research and Development<br>Activity<br>NSTL Station<br>Bay St. Louis, MS 39522 | 1 |
| 18. | Commander<br>Oceanographic Systems Pacific<br>Box 1390<br>Pearl Harbor, HI 96860                                                   | 1 |

**END**

**FILMED**

**1-85**

**DTIC**